

A Systematic Study of Supernova Remnants  
in the Large and Small Magellanic Clouds with *Suzaku*  
(すざく衛星を用いたマゼラン星雲内の超新星残骸の系統解析)

Yoko Takeuchi  
(武内 陽子)

Department of Physics, Graduate School of Science, Tokyo University of Science  
(東京理科大学大学院 理学研究科 物理学専攻)

High Energy Astrophysics Laboratory, RIKEN  
(理化学研究所 玉川高エネルギー宇宙物理研究室)

E-Mail: [takeuchi@crab.riken.jp](mailto:takeuchi@crab.riken.jp)

March, 2016



# Abstract

Supernova (SN) explosions eject various chemical elements produced by nuclear fusion reactions in a star. Supernovae (SNe) are classified into Type Ia and core-collapse (CC) depending upon the nature of the progenitor star and the explosion mechanism. Classification of the progenitors of supernova remnants (SNRs) is crucial for determining the rates of SN explosions in a galaxy, which is key to understanding the evolution of the chemical composition of the Universe. Because SNRs are composed of hot plasmas with temperatures of at least  $10^7$  K, they emit soft X-rays in the form of emission lines from heavy elements and thermal bremsstrahlung radiation. In many cases, many of these emission lines originate from the hot ejecta from the exploded progenitor star. Detailed analysis of these emission lines will enable us to directly measure the chemical abundances of SNR progenitors. In general, to determine the progenitor type of an SNR, the first step is to separate the X-ray emission of the ejecta from the swept-up interstellar medium (ISM). To decipher the morphological and spectral properties of SNRs, which are generally spatially diffuse objects, it is ideal to use X-ray instruments equipped with a high angular resolution, such as those onboard the *Chandra* satellite. However, for many SNRs which only appear as point sources in the instruments of current X-ray observatories, such as distant extragalactic SNRs, we can only obtain spatially integrated spectral information.

With that in mind, we conceive of new observational diagnostics for progenitor classification by utilizing instruments with a high resolution in the energy space without the requirement of a high angular resolution; these diagnostics are independent of whether or not the SNR in question is spatially resolvable by the instrument. To develop our new diagnostics, we attempt a systematic study of a total of 20 SNRs in the Large and Small Magellanic Clouds (LMC/SMC) using archival data of the *Suzaku* satellite. Although the angular resolution of *Suzaku* does not allow us to spatially resolve the SN ejecta from the swept-up ISM, its excellent energy resolution makes it possible to clearly separate emission

lines in the soft X-ray band, which is crucial for accurate abundance measurements. There are several merits of studying SNRs in the LMC and SMC. For example, the distances to these SNRs are effectively known to be  $\sim 50$  kpc, and the interstellar absorption toward the LMC and SMC is known to be even smaller than that toward our Galactic center.

In this thesis, we present a systematic analysis of nine evolved SNRs in the LMC and SMC: DEM L238, DEM L249, 0534–69.9, 0548–70.4, B0532–71.0, B0532–67.5, 0103–72.6, 0049–73.6, and 0104–72.3. However, the X-ray emission from an evolved SNR in the adiabatic phase (a.k.a. the Sedov phase) is dominated by the swept-up ISM, making it difficult to determine its ejecta composition and thus its SN type. We find that the characteristic spectral feature around 1 keV is markedly different among the SNRs; the first four SNRs show enhanced Fe L-shell emission, whereas the other five are dominated by Ne K-shell lines. This finding implies that SN ejecta still contribute considerably to the spatially integrated X-ray spectra of the otherwise ISM-dominant SNRs, making our spectral analysis of spatially integrated data from these SNRs meaningful for progenitor determination. Moreover, the Fe/Ne mass ratios, determined mainly from the well-resolved Fe L-shell and Ne K-shell lines, clearly divide the observed SNRs into the Type Ia and CC groups, confirming some previous classifications made by *Chandra* observations that utilized its extremely high angular resolution. This indicates that the spatially integrated X-ray spectra of old ( $\sim 10^4$  yr) SNRs can also be effective for discriminating their progenitor types, which would be helpful for future systematic studies of extragalactic SNRs with *ASTRO-H*, *Athena*, and other future satellites.

# Contents

<b>Abstract</b>	<b>i</b>
<b>1 INTRODUCTION</b>	<b>1</b>
<b>2 REVIEW OF SUPERNOVAE AND SUPERNOVA REMNANTS</b>	<b>5</b>
2.1 Classification of SNe	5
2.1.1 Type Ia SNe	6
2.1.2 Core-collapse SNe: Types Ib, Ic, and II	7
2.2 Stellar Nucleosynthesis	8
2.2.1 H burning	8
2.2.2 He burning	10
2.2.3 Heavy-element burning	10
2.2.4 Difference in abundances between Type Ia and CC SNe	12
2.3 Dynamical Evolution of SNRs	13
2.3.1 $M_{\text{ISM}} \ll M_{\text{ej}}$ : Free expansion phase	13
2.3.2 $M_{\text{ISM}} \approx M_{\text{ej}}$ : Transition phase	15
2.3.3 $M_{\text{ej}} \lesssim M_{\text{ISM}}$ : Adiabatic phase (Sedov phase)	16
2.3.4 $M_{\text{ej}} \ll M_{\text{ISM}}$ : Radiative cooling phase	16
2.4 Shock Wave Processes	17
2.4.1 Shock wave heating	17
2.4.2 Collisionless shocks	20
2.4.3 Cosmic-ray acceleration	20
2.5 X-ray Polarimetry Observations	21
<b>3 THERMAL PLASMAS OF SNRS</b>	<b>23</b>
3.1 Classification of Plasma State	23

3.2	X-ray Emission . . . . .	25
3.2.1	Continuous emissions . . . . .	25
3.2.2	Emission lines . . . . .	29
<b>4</b>	<b>X-RAY OBSERVATIONS OF SNRS</b>	<b>37</b>
4.1	Compact Objects . . . . .	37
4.2	X-ray Abundance . . . . .	38
4.3	Morphology . . . . .	39
4.4	Property of Fe K-shell Emission . . . . .	41
<b>5</b>	<b>INSTRUMENTS</b>	<b>45</b>
5.1	Overview of the <i>Suzaku</i> Satellite . . . . .	45
5.2	X-ray Telescope (XRT) . . . . .	47
5.3	X-ray Imaging Spectrometer (XIS) . . . . .	47
5.3.1	Overview . . . . .	47
5.3.2	Basic performance . . . . .	50
5.3.3	Radiation damage . . . . .	51
<b>6</b>	<b>OBSERVATIONS</b>	<b>55</b>
6.1	Target Selection . . . . .	55
6.2	Observation and Data Reduction . . . . .	58
6.3	Classification of SNRs . . . . .	59
<b>7</b>	<b>ANALYSIS AND RESULTS</b>	<b>63</b>
7.1	Spectral Features . . . . .	63
7.2	Model Fitting . . . . .	63
7.2.1	One-temperature NEI model . . . . .	63
7.2.2	Two-temperature NEI model . . . . .	69
<b>8</b>	<b>DISCUSSION</b>	<b>73</b>
8.1	Brief Summary of the Preceding Works and Our Results . . . . .	73
8.1.1	DEML238 & DEML249 . . . . .	73
8.1.2	0534–69.9 & 0548–70.4 . . . . .	74
8.1.3	B0532–71.0 . . . . .	74
8.1.4	B0532–67.5 . . . . .	74

8.1.5	0103–72.6 . . . . .	74
8.1.6	0049–73.6 . . . . .	75
8.1.7	0104–72.3 (a.k.a. IKT 25) . . . . .	75
8.2	Classification of SNRs with the Fe/Ne Abundance Ratio . . . . .	76
8.3	Electron Temperature Trend . . . . .	80
8.4	Future Prospects . . . . .	81
<b>9</b>	<b>CONCLUSION</b>	<b>87</b>
<b>A</b>	<b>ANALYSIS OF YOUNG SNRS</b>	<b>89</b>
A.1	Spectral Features . . . . .	89
A.2	Model Fitting . . . . .	91
A.2.1	Two-temperature NEI model . . . . .	91
A.2.2	Single Gaussian model . . . . .	94
	<b>Acknowledgements</b>	<b>115</b>



# List of Figures

2.1	Classification scheme for SNe based on spectral and light curve features for a few months . . . . .	6
2.2	Onion-like structure of a massive star before core collapse. . . . .	11
2.3	Number ratio of elemental abundance to solar ( $X_{\odot}$ ) predicted for Type Ia and CC SNe . . . . .	14
2.4	Schematic views of an SNR heating shock wave. . . . .	15
2.5	Schematic views of the shock front in the observer rest frame and the shock rest frame . . . . .	17
2.6	A schematic view of a TPC X-ray polarimeter of the <i>PRAxIS</i> mission . . .	21
3.1	A schematic view of plasma states. . . . .	24
3.2	Predicted X-ray spectrum from thin thermal plasma of Si in the CIE condition without the detector response . . . . .	26
3.3	A schematic view of bremsstrahlung emission. . . . .	27
3.4	(a) A schematic view of the emission mechanism for RRC. (b) Predicted RRC spectrum made by H-like Fe ions . . . . .	28
3.5	Ion fractions of several elements in collisional ionization equilibrium as a function of the electron temperature . . . . .	31
3.6	Centroid K-shell energy as a function of ionization state $n_{et}$ for Si, S, Ar, and Ca . . . . .	32
3.7	$Ly\alpha/He\alpha$ flux ratio as a function of ionization state $n_{et}$ for Si, S, Ar, and Ca 33	
3.8	$He\beta/He\alpha$ flux ratio as a function of the electron temperature for Si, S, Ar, and Ca in CIE state . . . . .	34
3.9	$Ly\beta/Ly\alpha$ flux ratio as a function of the electron temperature for Si, S, Ar, and Ca in CIE state . . . . .	35

4.1	X-ray image of the Crab nebula and its pulsar . . . . .	38
4.2	<i>Chandra</i> X-ray intensity map and integrated spectrum of N103B in the LMC	39
4.3	<i>Chandra</i> X-ray images and X-ray spectra of SNR 0049–73.6 in the SMC . .	40
4.4	<i>Chandra</i> soft X-ray images (0.5–2.1 keV) of 24 SNRs in our Galaxy and the LMC . . . . .	41
4.5	Results from a statistical analysis using line emission image with <i>Chandra</i> .	42
4.6	Diagnostic for progenitor type using Fe K $\alpha$ line with <i>Suzaku</i> . . . . .	43
5.1	Schematic view and side-view of <i>Suzaku</i> . . . . .	46
5.2	Photograph of the XRT without the thermal shield . . . . .	48
5.3	Schematic view of the XRT mounted on the <i>Suzaku</i> EOB . . . . .	48
5.4	Vignetting of the four XRT-I modules using the measured data of the Crab nebula in the two energy bands . . . . .	48
5.5	Photograph and side-view of the XIS CCD . . . . .	49
5.6	Top view of the XIS CCD . . . . .	49
5.7	Quantum efficiency of the XIS as function of incident X-ray energy for FI and BI CCD . . . . .	50
5.8	Effective area of the XIS including the XRT for FI and BI CCD . . . . .	50
5.9	The total effective area of the XRT-I combined to the XIS compared with that of <i>Chandra</i> and <i>XMM-Newton</i> . . . . .	51
5.10	The XIS response function to incident monochromatic X-ray . . . . .	52
5.11	Background count rate of XIS as a function of energy compared with that of <i>ASCA</i> , <i>Chandra</i> , and <i>XMM-Newton</i> . . . . .	52
5.12	The time history of the center energy and energy resolution. . . . .	53
6.1	Optical images of the LMC and SMC . . . . .	56
6.2	Locations of the LMC and SMC relative to our Galaxy. . . . .	58
6.3	Each XIS image of SNR 0534-69.9 in the LMC . . . . .	60
6.4	Classification scheme for our targets based on the SNR age. . . . .	60
7.1	Background-subtracted XIS spectra . . . . .	64
7.2	<i>Suzaku</i> XIS spectra of the MCs SNRs fitted with the $1-kT_e$ NEI fit model .	67
7.3	Same as figure 7.2 for a fit with the $2-kT_e$ NEI model . . . . .	70

8.1	The relation of measured abundances of Fe and Ne for the SNRs in the LMC and the SMC . . . . .	77
8.2	Fe/Ne mass ratios as a function of the SNR radius . . . . .	78
8.3	Confidence contour for the abundance ratio of Fe to Ne determined from the spectrum of 0104–72.3 . . . . .	79
8.4	Density-weighted electron temperature as a function of the SNR radius . . . . .	80
8.5	(a) Simulated spectra of SNR 0104–72.3 in the 0.8–1.1 keV band for observations with the SXS aboard <i>ASTRO-H</i> . (b) Simulated SXS spectra of DEM L249 and 0103–72.6 . . . . .	82
8.6	Simulated spectra of SNR 0548–70.4 and B0532–71.0 in the 0.8–1.1 keV and 0.5–2.0 keV band for observations with the SXS aboard <i>ASTRO-H</i> . . . . .	82
8.7	Location maps of the M31 and M33 SNRs superposed on star-subtracted H $\alpha$ images. . . . .	83
8.8	X-ray image of M31 with SNR candidates using the <i>XMM-Newton</i> EPIC . . . . .	85
A.1	<i>Suzaku</i> XIS spectra of the young LMC/SMC SNRs, where the background spectra are subtracted . . . . .	90
A.2	<i>Suzaku</i> XIS spectra of the young MCs SNRs fitted with the $2\text{-}kT_e$ NEI fit models . . . . .	92
A.3	The fitting results of SNR N103B for four type models . . . . .	96
A.4	The fitting results of SNR 0509–67.5 for four type models . . . . .	98
A.5	The fitting results of SNR 0519–69.0 for four type models . . . . .	100
A.6	The fitting results of SNR N63A for 4 type models . . . . .	102
A.7	The fitting results of SNR N49 for 4 type models . . . . .	104
A.8	The fitting results of SNR N132D for 4 type models . . . . .	106



# List of Tables

2.1	Products with nucleosynthesis. . . . .	12
2.2	Total mass of heavy element synthesized by Type Ia and CC SNe. . . . .	13
3.1	K-shell line energies of H-like and He-like ions. . . . .	30
5.1	<i>Suzaku</i> performance . . . . .	46
6.1	List of the MCs SNRs observed by <i>Suzaku</i> . . . . .	57
6.2	Select region for spectral analysis. . . . .	59
6.3	List of SNR we analyzed. . . . .	61
7.1	Mean LMC ISM abundances. . . . .	65
7.2	Mean SMC ISM abundances. . . . .	66
7.3	The best-fit spectral parameters of the one-temperature component with NEI	68
7.4	The best-fit spectral parameters of the two-temperature NEI model . . . . .	71
8.1	Parameters of future X-ray mission instruments. . . . .	83
A.1	The best-fit spectral parameters of the $2\text{-}kT_e$ NEI model. . . . .	93
A.2	List of parameter conditions for the gaussian models. . . . .	95
A.3	The best-fit parameters with multi-gaussians + continuum model in N103B	97
A.4	The best-fit parameters with multi-gaussians + continuum model in 0509-67.5	99
A.5	The best-fit parameters with multi-gaussians + continuum model in 0519-69.0101	
A.6	The best-fit parameters with multi-gaussians + continuum model in N63A	103
A.7	The best-fit parameters with multi-gaussians + continuum model in N49	105
A.8	The best-fit parameters with multi-gaussians + continuum model in N132D	107



# Chapter 1

## INTRODUCTION

Supernovae (SNe) are some of the most energetic events in the Cosmos and are brought about by explosions of stars in galaxies. They are so energetic and luminous that they can usually outshine their host galaxies and can be captured by smaller amateur telescopes or even the naked eye in a clear night sky. It is widely believed that SNe play the important role of synthesizing and ejecting chemical elements into interstellar space that eventually become the essential ingredients of organic life as we know today. Two distinct types of SN explosions are known so far, namely, Type Ia SNe and core-collapse (CC) SNe. Type Ia SNe occur through the thermonuclear detonation of white dwarf (WD) stars, which are the remnants of less massive stars such as the Sun. They are thought to occur in binary systems composed of either a WD and a companion star or two WDs. CC SNe, on the other hand, involve more massive stars, which are expected to end their life by self-explosion. Since there are clear differences in the resultant chemical abundances between the two types of SNe due to their different progenitors, explosion mechanisms, and nucleosynthesis processes, it is vital to determine their rates of occurrence in individual galaxies to reveal their recent chemical enrichment histories. X-ray observations of young supernova remnants (SNRs) allow us to distinguish their parent SN types owing to the fact that their X-ray spectra are dominated by emission originating directly from the ejecta (debris) of the exploded progenitor star (e.g., Vink, 2012). The Large Magellanic Cloud (LMC), the nearest galaxy from our Milky Way, is probably the best place for us to perform a comprehensive study of galactic chemical evolution. The SN rate in the LMC was estimated using *ASCA* data of young ( $t \lesssim 1,500$  yr) LMC SNRs (Hughes *et al.*, 1995). On the other hand, identifying the progenitor type of evolved ( $t \gtrsim 5,000$  yr) SNRs is often very challenging because their (volume-integrated) X-ray line emissions

are often dominated by the swept-up interstellar medium (ISM) heated by the outgoing shockwave of the SNRs rather than by the stellar materials. In fact, previous *ASCA* and *XMM-Newton* observations of Magellanic Sedov-phase SNRs were utilized to study ISM abundances (e.g., Hughes *et al.*, 1998; van der Heyden *et al.*, 2004). A breakthrough was achieved through observations by the *Chandra* X-ray observatory, which possesses the highest angular resolution ( $\sim 0''.5$ ) among the current X-ray space telescopes. By allowing us to spatially resolve the ejecta core from the swept-up ISM shell, *Chandra* has successfully discriminated the progenitor types of a number of evolved SNRs in the Magellanic Clouds (e.g., DEM L71: Hughes *et al.*, 2003; N49B: Park *et al.*, 2003b; N132D: Borkowski *et al.*, 2007; and B0049–73.2: Hendrick *et al.*, 2005; Schenck *et al.*, 2014).

Opportunities for spatially resolved spectral analyses are, unfortunately, relatively limited owing to their more stringent criteria, such as long required exposure times from telescopes with high angular resolutions (which generally have very tight yearly mission schedules) and observation targets with reasonable angular sizes in the sky. Although the forthcoming X-ray mission *ASTRO-H* (Takahashi *et al.*, 2014) will dramatically change our view of SNRs owing to its excellent spectral resolution ( $\sim 5$  eV at 0.5–10 keV), its angular resolving power of 1.3 is only comparable to the typical angular size of evolved SNRs in the Magellanic Clouds ( $\sim 1'$ ). Moreover, SNRs in nearby spiral galaxies (e.g., M31) cannot be resolved into ejecta and ISM components even with *Chandra*'s angular resolution. It therefore would be of tremendous value if we could identify a simple and reliable diagnostic in X-ray spectral data effective for discriminating progenitor types of SNRs that can also be achieved using instruments without excellent angular resolution. We already know that this is not unachievable. For example, metal enhancements of the middle-aged ( $t \sim 5,000$  yr) LMC SNRs DEM L71 and N49B (of Fe and Mg, respectively), which were first revealed by *Chandra* data, have been confirmed by recent *Suzaku* observations (Uchida *et al.*, 2015). This suggests that some important plasma properties diagnosable by spatially resolved X-ray spectra can persist in data integrated over larger regions of SNRs, and these data can also be obtained by telescopes with less outstanding spatial resolving power. In this case of the *Suzaku* observations, such as the example given above, successes are often attributable to the high sensitivity (to emission lines) of the X-ray Imaging Spectrometer (XIS: Koyama *et al.*, 2007) onboard the satellite.

In this thesis, we focus on the establishment of a new observational diagnostic for progenitor classification from ‘spatially integrated’ X-ray spectra of SNRs observed by the

*Suzaku* XIS by using its high energy resolution without the requirement of a high angular resolution. To develop our methodology, we attempt a systematic study of a total of 20 SNRs in the LMC and Small Magellanic Cloud (SMC) using the *Suzaku* XIS archival data. Specifically, to put our new technique to the test, we perform a systematic study of nine evolved SNRs whose classification is known to be very difficult without space-resolved spectral information.

This thesis is organized as follows. We first review the anatomy and fundamental theory of SNe and SNRs in Chapter 2. The physical mechanisms of X-ray thermal emission in SNRs are then discussed in Chapter 3. In Chapter 4, an outline of our data analysis methods for X-ray observations of SNRs is given. An introduction to the powerful instruments onboard the *Suzaku* satellite can then be found in Chapter 5. In Chapter 6, we describe our target selection criteria and data reduction procedures, which is followed by a presentation of our spectral analysis results in Chapter 7. These results are discussed in detail in Chapter 8. Finally, we conclude this work in Chapter 9.



## Chapter 2

# REVIEW OF SUPERNOVAE AND SUPERNOVA REMNANTS

Supernovae (SNe) are energetic explosion events of evolved massive stars at the end of their lives, which are one of the big events in the Universe. The kinetic energy of expansion,  $E_{\text{SN}}$ , typically reaches  $\sim 10^{51}$  erg. Elements with masses up to that of iron are synthesized inside stars and are spread by SN explosions over interstellar space, then these elements become material for the next generation of stars. SNe play a very important role in the chemical evolution of the Universe. Supernova remnants (SNRs) are nebulae of heated interstellar gas and ejecta material observable from their X-ray emission for more than  $10^4$  yr after the explosion. SNRs retain crucial information about nucleosynthesis in their progenitors and the elemental composition of the interstellar medium (ISM), which are key to understanding the chemical evolution of the Universe. In this chapter, we describe the basic features of SNe and SNRs.

### 2.1 Classification of SNe

When SN explosions occur, they have the appearance of a new star in the sky for a few months. SNe are observationally classified as Type I and Type II with/without absorption lines, respectively, in the light curve (luminosity as a function of elapsed time from the explosion) from their optical spectrum as illustrated in figure 2.1 (Harkness & Wheeler, 1990). Type II is distinguished from other SN types by its light curve having H absorption. Type II is classified into more detailed types from its light curve (Types II-L, II-P, and others). If an optical light curve has a negative gradient, it is defined as Type

II-L (linear). Type II-P has a slower decline (plateau phase) than a normal light curve. On the other hand, if there is no H absorption in the optical spectrum, the SNe are classified as Type I. Type I is further separated into Types Ia, Ib, and Ic depending on the absence or presence of He and Si absorption lines.

SNe are also classified according to the expansion mechanism. The thermonuclear expansion of a white dwarf (WD) may create a Type Ia SN. The other types (Types II, Ib, and Ic) occur by the sudden gravitational collapse of the core of a massive star ( $M \gtrsim 8 M_{\odot}$ , where  $M_{\odot}$  is the mass of the Sun). We describe the origins of these SNe in detail in the following subsection.

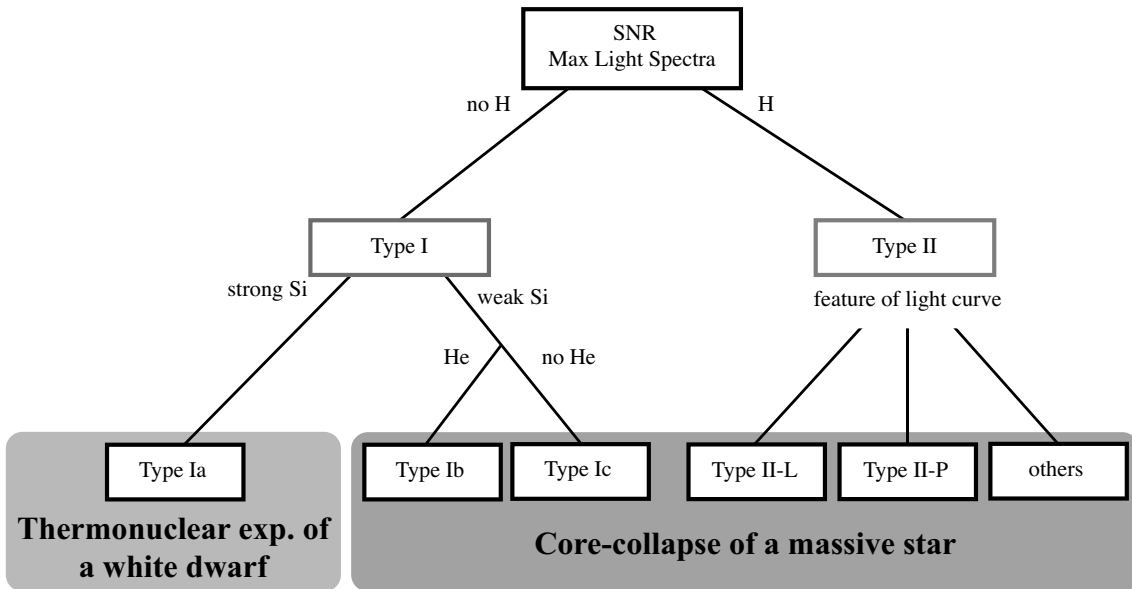


**Figure 2.1:** Classification scheme for SNe based on spectral and light curve features for a few months (Harkness & Wheeler, 1990).

### 2.1.1 Type Ia SNe

Since the optical spectra of Type Ia SNe have no H absorption line, the progenitor has lost its outer layer of H. A Type Ia SN is believed to be the explosion of a WD in a binary system. A WD is a stellar remnant of mass  $< 8 M_{\odot}$  and has a C+O core. The scenario of the explosion of a WD is considered to have two patterns. One is caused by a WD with a main sequence star such as a supergiant star. Gas is stripped from the star and accumulates around the WD. When the total mass of the WD including the accumulated gas exceeds the Chandrasekhar limit of  $\sim 1.4 M_{\odot}$ , beyond which it cannot be supported

against its weight by electron degeneracy pressure, the WD expands through a process known as thermal runaway. Another scenario, with a doubly degenerate progenitor, is the merger of two WDs whose combined mass exceeds the Chandrasekhar limit. In this scenario, there is no compact object or black hole. More of some elements such as Fe and Si are synthesized rather than O, Ne, and Mg (Nomoto *et al.*, 1984; Iwamoto *et al.*, 1999). The characteristic light curves of Type Ia SNe often show the same peak brightness because of their progenitor WDs having a similar mass at the Chandrasekhar limit. Thus, Type Ia SNe are utilized for the measurement of cosmological distances. Although many researchers have attempted to explain the detailed physical mechanism of the explosions, no one has yet fully succeeded.

### 2.1.2 Core-collapse SNe: Types Ib, Ic, and II

CC SNe are the catastrophic explosions of massive stars ( $M \gtrsim 8 M_{\odot}$ ). The final phase of evolution of a massive star is different from that of a lighter star such as the Sun. A massive star can generate heavier elements than H and He by nuclear fusion at the center due to a higher pressure and temperature (for details see § 2.2). If we could cut through a star and look at its cross section, we would see an onion-like structure with envelopes of different elements undergoing nuclear fusion. Finally, an Fe core is produced at the center of the star. The energy generated by nuclear fusion counteracts the force of gravity and prevents the star from collapsing, keeping the star in hydrostatic equilibrium. When the Fe core is increasingly compressed and reaches an internal temperature of  $\sim 3 \times 10^9$  K, the photodisintegration of Fe nuclei occurs as follows:



Since this reaction is endothermic, the equilibrium is broken, then the star cannot support itself against its gravity and collapses. The gravitational energy released by the surrounding stellar matter creates a shock wave that propagates outward. The shock wave leads to explosive nuclear fusion and ejects the nuclear-fused material outwards. Therefore, the abundances created by CC (Types Ib, Ic and II) are affected by the envelope, which depends on the mass of the collapsing star. The remnants of the core leave a neutron star or a black hole after the explosion. The total energy generated by the gravitational collapse

is  $\sim 10^{53}$  erg for  $\sim 10$  s during CC SNe. However, the energy of the expanding shock wave is only  $\sim 10^{51}$  erg because neutrinos carry away 99% of the total energy. Massive stars have a shorter lifetime ( $\sim 10^6$ – $10^7$  yr) than lighter stars ( $\sim 10^{10}$  yr); thus, the CC SN rate is higher than that of Type Ia SNe. In fact, CC SNe events account for approximately 75% of all observed SNe.

The difference between Type Ib/Ic and Type II is related to the mass of the progenitor. The progenitors of Type Ib/Ic are much heavier stars,  $> 25 M_{\odot}$ , than those of Type II SNe. Type Ib progenitors have outer atmospheres deprived of most of their H, while Type Ic progenitors have shed both the H and He layers due to strong stellar wind or from their interaction with a close companion of  $3$ – $4 M_{\odot}$  (Pols, 1997; Woosley & Eastman, 1997). Therefore, their optical spectra do not have H lines (and He lines for Type Ic). Highly massive stars are formed rarely; the occurrence rate of Type Ib and Ic SNe is much lower than that of Type II SNe.

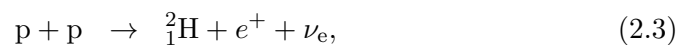
## 2.2 Stellar Nucleosynthesis

Stellar nucleosynthesis is the process by which the natural abundances of the chemical elements within stars vary owing to nuclear fusion in their cores and overlying envelopes. In this section, we briefly mention their nucleosynthesis.

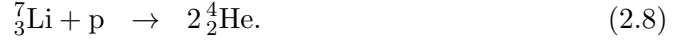
### 2.2.1 H burning

In main sequence stars, the nuclear fusion of hydrogen occurs in the core. The reactions are generally called the “proton-proton (p-p) chain” and the “CNO cycle”. The p-p chain consists of three branches depending on the temperature,  $T$ , as follows:

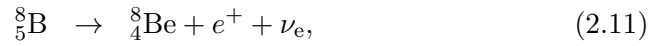
- p-p I ( $0.8 \times 10^7 \text{ K} < T < 1.4 \times 10^7 \text{ K}$ ):



- p-p II ( $1.4 \times 10^7 \text{ K} < T < 2.3 \times 10^7 \text{ K}$ ):



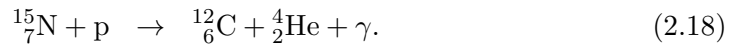
- p-p III ( $T > 2.3 \times 10^7 \text{ K}$ ):



He is created from H by this process. These reactions typically require  $10^9$  yr to complete.

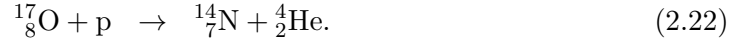
When the central temperature reaches  $\sim 2 \times 10^7 \text{ K}$ , the other H burning process, the CNO cycle, becomes dominant. This cycle occurs in massive stars compared with the Sun. The main reactions of the CNO cycle are defined below.

- CNO cycle:



Here, the  ${}^{12}_6\text{C}$  produced in the last reaction is recycled in the first reaction of the CNO cycle. This process involves  ${}^{12}_6\text{C}$ ,  ${}^{13}_6\text{C}$ ,  ${}^{14}_7\text{N}$ , and  ${}^{15}_7\text{N}$ , which is why it is called the CNO cycle. This reaction has a minor branch. After the reaction produces  ${}^{15}_7\text{N}$  (equation 2.17), the next reaction does not produce  ${}^{12}_6\text{C}$  and instead produces  ${}^{16}_8\text{O}$  and photons as follows.

- CNO-2 cycle:



The  ${}^{17}_9\text{F}$  produced in this minor cycle merely acts as a catalyst. The timescale for the completion of the CNO cycle is typically  $\sim 4 \times 10^8$  yr and is shorter than that of the p–p chain. Stars spend most of their lifetime in the H burning stage.

### 2.2.2 He burning

When the H burning process fuses H to He in the core, the pressure which is necessary to counteract gravity is no longer maintained. The core of He begins to compress, causing the temperature and pressure to become sufficiently high for He to burn. The reaction of He fusion, named the triple- $\alpha$  process, occurs at  $T > 10^9$  K,



As an additional process to the triple- $\alpha$  process,  ${}^{16}_8\text{O}$  is produced simultaneously by the reaction



As a result of this reaction, the core consists of  ${}^{12}_6\text{C}$  and  ${}^{16}_8\text{O}$  formed in the star center. In a star of below  $8 M_\odot$ , the nucleosynthesis ends after this reaction. The star sheds most of its mass to form a planetary nebula. The C+O core is left, which becomes a WD whose size is the same as that of Earth but whose mass is  $\sim M_\odot$ .

### 2.2.3 Heavy-element burning

When the core temperature further increases, carbon and oxygen are synthesized by He burning. These processes depend on the temperature and density in the core, and

proceed quickly in stars whose mass is larger than  $\sim 2 M_{\odot}$ . The temperature and density are determined by the mass of the star. If the mass of the star exceeds  $8 M_{\odot}$ , carbon burning begins to produce an O, Ne, and Mg core. If the mass exceeds  $10 M_{\odot}$ , the nuclear fusion continues until the core consists of Fe synthesized through heavier-element burning (e.g., O burning and Si burning). Therefore, the inner structure of a massive star resembles an onion as shown in figure 2.2. The star cannot produce any heavier nuclei than Fe since Fe is the most stable nucleus. Such massive stars become the progenitors of CC SNe.

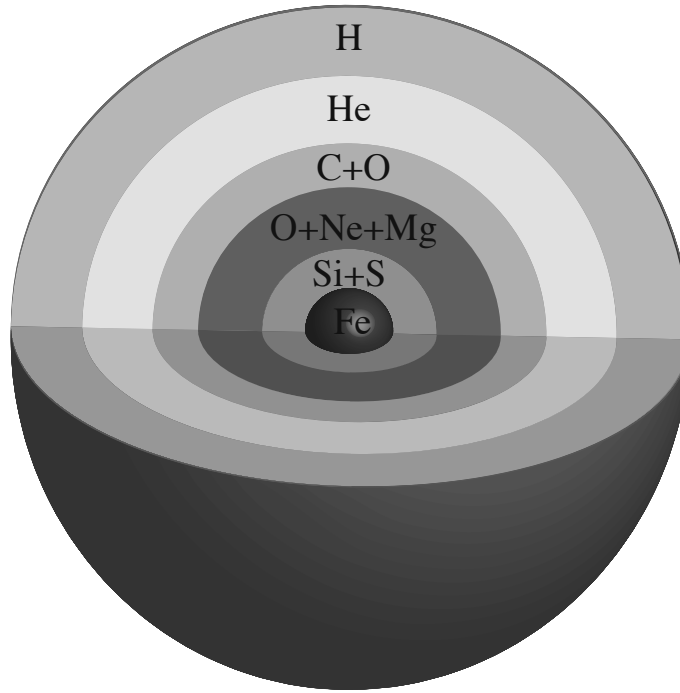
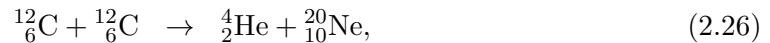


**Figure 2.2:** Onion-like structure of a massive star before core collapse.

When the maximum temperature reaches  $\sim 10^9$  K, explosive carbon burning begins:



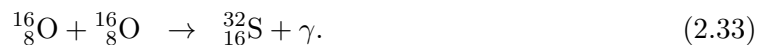
At the same temperature, Ne burning is described as



**Table 2.1:** Products with nucleosynthesis.

Mass	Process	Main products	timescale	Ignition temperature (K)
	H burning	He	$\sim 10^9$ yr	$\sim 10^7$
$< 8 M_{\odot}$	He burning	B, C, O	$\sim 10^5$ yr	$\sim 10^9$
$> 8 M_{\odot}$	C & Ne burning	O, Ne, Mg, Si	$\sim 10^3$ yr	$2 \times 10^9$
	O burning	O, Si, S, Ar, Ca	$\sim 1$ yr	$3\text{--}4 \times 10^9$
$> 10 M_{\odot}$	Si burning	Si, S, Ar, Ca, Cr, Mn, Fe, Co, Ni, Zn	$\sim$ day	$4 \times 10^9$

After Ne burning, O burning begins at an ignition temperature of  $\sim 3\text{--}4 \times 10^9$  K.



Furthermore, after O burning, Si burning begins at a temperature over  $\sim 4 \times 10^9$  K. This process forms several heavy elements (e.g., Ar, Ca, Cr, Fe, and Ni). Table 2.1 lists the products of these nucleosyntheses, the timescale of the reaction, and the ignition temperature.

#### 2.2.4 Difference in abundances between Type Ia and CC SNe

The type and number of elements synthesized by nuclear fusion are dependent on the mass of the progenitor star. Since progenitor stars have different masses, which may lead to different types of SNe, the chemical abundance patterns of their SN ejecta also have different characteristics. Despite the many theoretical models constructed by previous researchers, we still have not completely elucidated the mechanism of SN expansion and its relationship with the resultant metal abundance. Table 2.2 lists the typical masses of the various elements synthesized in Type Ia and CC SNe predicted by Iwamoto *et al.* (1999) and Kobayashi *et al.* (2006). For products of Type Ia SNe, we adopt the values from the WDD2 model (Iwamoto *et al.*, 1999). This model is calculated assuming a delay-detonation model, which has recently been favored by the supernova community. Figure 2.3 shows the number ratios of abundance for Type Ia and CC SNe models, which are normalized by that of Si. This model indicates that the abundance of Fe in Type Ia

**Table 2.2:** Total mass of heavy element synthesized by Type Ia and CC SNe.

Element	Synthesized mass ( $M_{\odot}$ )				
	Type Ia*	CC SNe†			
		$13 M_{\odot}$	$15 M_{\odot}$	$20 M_{\odot}$	$40 M_{\odot}$
C	$8.99 \times 10^{-3}$	$8.80 \times 10^{-2}$	$8.83 \times 10^{-2}$	$9.77 \times 10^{-2}$	$4.58 \times 10^{-1}$
N	$2.69 \times 10^{-4}$	$9.08 \times 10^{-3}$	$1.29 \times 10^{-2}$	$1.84 \times 10^{-2}$	$2.60 \times 10^{-2}$
O	$4.58 \times 10^{-2}$	$3.87 \times 10^{-1}$	$2.93 \times 10^{-1}$	$9.95 \times 10^{-1}$	$7.96 \times 10^0$
Ne	$6.22 \times 10^{-4}$	$1.34 \times 10^{-1}$	$1.26 \times 10^{-1}$	$2.79 \times 10^{-1}$	$1.88 \times 10^0$
Mg	$4.52 \times 10^{-3}$	$4.64 \times 10^{-2}$	$7.85 \times 10^{-2}$	$1.00 \times 10^{-1}$	$4.04 \times 10^{-1}$
Si	$2.06 \times 10^{-1}$	$6.22 \times 10^{-2}$	$1.05 \times 10^{-1}$	$1.27 \times 10^{-1}$	$5.34 \times 10^{-1}$
S	$1.24 \times 10^{-1}$	$2.69 \times 10^{-2}$	$3.45 \times 10^{-2}$	$5.16 \times 10^{-2}$	$2.26 \times 10^{-1}$
Ar	$2.50 \times 10^{-2}$	$4.67 \times 10^{-3}$	$4.80 \times 10^{-3}$	$8.30 \times 10^{-3}$	$3.59 \times 10^{-3}$
Ca	$2.47 \times 10^{-2}$	$3.94 \times 10^{-3}$	$3.11 \times 10^{-3}$	$6.53 \times 10^{-3}$	$2.84 \times 10^{-3}$
Fe	$7.93 \times 10^{-1}$	$7.49 \times 10^{-2}$	$7.44 \times 10^{-2}$	$7.77 \times 10^{-2}$	$1.80 \times 10^{-2}$
Ni	$5.87 \times 10^{-2}$	$2.40 \times 10^{-3}$	$2.21 \times 10^{-3}$	$1.96 \times 10^{-3}$	$1.93 \times 10^{-3}$

\* Reference: (Iwamoto *et al.*, 1999). The used model is WDD2.

† Reference: (Kobayashi *et al.*, 2006). The values are with a progenitor metallicity of  $Z = 0.004$ .

SNe is  $\sim 10$  times larger than that in CC SNe, whereas the abundances of light elements (e.g., O, Ne, Mg) in CC SNe are  $\sim 100$  times larger than those in Type Ia SNe.

## 2.3 Dynamical Evolution of SNRs

When an SN explosion occurs, the ejected materials (ejecta) expand in interstellar space with a high velocity as the result of a strong shock wave. The remnant structures are called SNRs. Basically, an SNR is composed of an expanding ejecta and the swept-up ISM. The evolution phase of an SNR is mainly determined by the relation between the masses of the ejecta ( $M_{\text{ej}}$ ) and the swept-up ISM ( $M_{\text{ISM}}$ ). We explain the four evolution phases in this section: the free expansion phase, transition phase, adiabatic phase (Sedov phase), and radiative cooling phase. We here assume that the density of the ambient medium is uniform.

### 2.3.1 $M_{\text{ISM}} \ll M_{\text{ej}}$ : Free expansion phase

After an SN explosion, the ejecta expands without deceleration since the interaction with the low-density ISM is ignored. The kinetic energy of the SN explosion,  $E_{\text{SN}}$ , is about

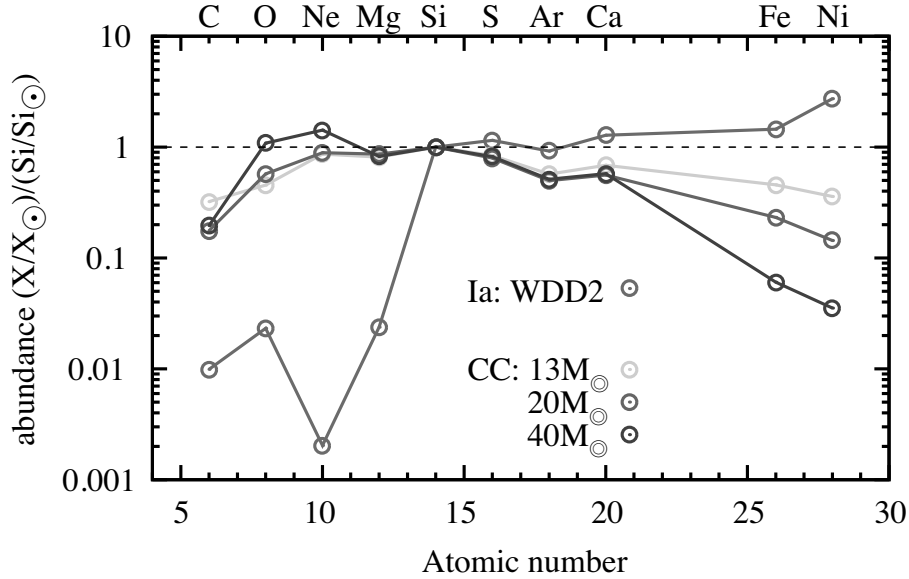


**Figure 2.3:** Number ratio of elemental abundance to solar ( $X_{\odot}$ ) predicted for Type Ia and CC SNe (Iwamoto *et al.*, 1999; Kobayashi *et al.*, 2006). The ordinate is normalized to Si.

$\sim 10^{51}$  erg in both Type Ia and CC SNe. The expansion velocity,  $v_e$ , is obtained using  $E_{\text{SN}}$  as

$$v_e = \sqrt{\frac{2E_{\text{SN}}}{M_{\text{ej.}}}} = 8.5 \times 10^8 \left( \frac{E_{\text{SN}}}{10^{51} \text{ erg}} \right)^{1/2} \left( \frac{M_{\text{ej.}}}{1.4 M_{\odot}} \right)^{-1/2} [\text{cm s}^{-1}]. \quad (2.34)$$

$v_e$  in this phase is typically  $\sim 10^4 \text{ km s}^{-1}$ , and is much larger than the sound speed in the ISM ( $\sim 15 \text{ km s}^{-1}$ ). Hence a strong shock wave is generated, namely a forward shock. Since the velocity of the shock wave is constant in this stage, the radius of the shock,  $R_s$ , can be written as

$$R_s = v_e t, \quad (2.35)$$

where  $t$  is the elapsed time after the SN explosion (thus, the SNR age). The expanding forward shock sweeps up the ISM. The mass of swept-up ISM ( $M_{\text{ISM}}$ ) is expressed as

$$M_{\text{ISM}} = \frac{4}{3} R_s^3 n_0 \mu m_{\text{H}}, \quad (2.36)$$

where  $n_0$ ,  $\mu$ , and  $m_{\text{H}}$  are the hydrogen number density of the ISM, the mean atomic weight, and the hydrogen mass, respectively. This phase of free expansion of the ejecta continues until  $M_{\text{ISM}}$  becomes comparable to  $M_{\text{ej.}}$ . The time scale  $t$  is obtained by equations 2.34,

2.35, and 2.36 to be

$$t \sim 2.5 \times 10^2 \left( \frac{E}{10^{51} \text{ erg}} \right)^{-1/2} \left( \frac{M_{\text{ej.}}}{1.4 M_{\odot}} \right)^{5/6} \left( \frac{\mu}{1.4} \right)^{-1/3} \left( \frac{n_0}{1 \text{ cm}^{-3}} \right)^{-1/3} \text{ [yr]}. \quad (2.37)$$

Therefore, this phase typically continues for a few hundred years.

### 2.3.2 $M_{\text{ISM}} \approx M_{\text{ej.}}$ : Transition phase

When  $M_{\text{ISM}}$  becomes comparable to  $M_{\text{ej.}}$ , the swept-up ISM gradually affects the evolution of the SNR, although it is not yet dominant. The swept-up ISM pushes back on the ejecta, which causes another shock wave (reverse shock). The ejecta is heated to a high temperature by the reverse shock and is gradually ionized (for details see § 3.1). The boundary between the ISM and the ejecta is called the “contact discontinuity”. The reverse shock initially propagates outward. When  $M_{\text{ISM}}$  becomes greater than  $M_{\text{ej.}}$ , the reverse shock propagates back to the center. Figure 2.4 shows a schematic view of an SNR in this phase. At this stage, the material subjected to shock by the two shock waves is sufficiently hot to emit X-rays, while the material in the central region cannot emit X-rays and is still expanding freely. Most young SNRs are probably in this stage.

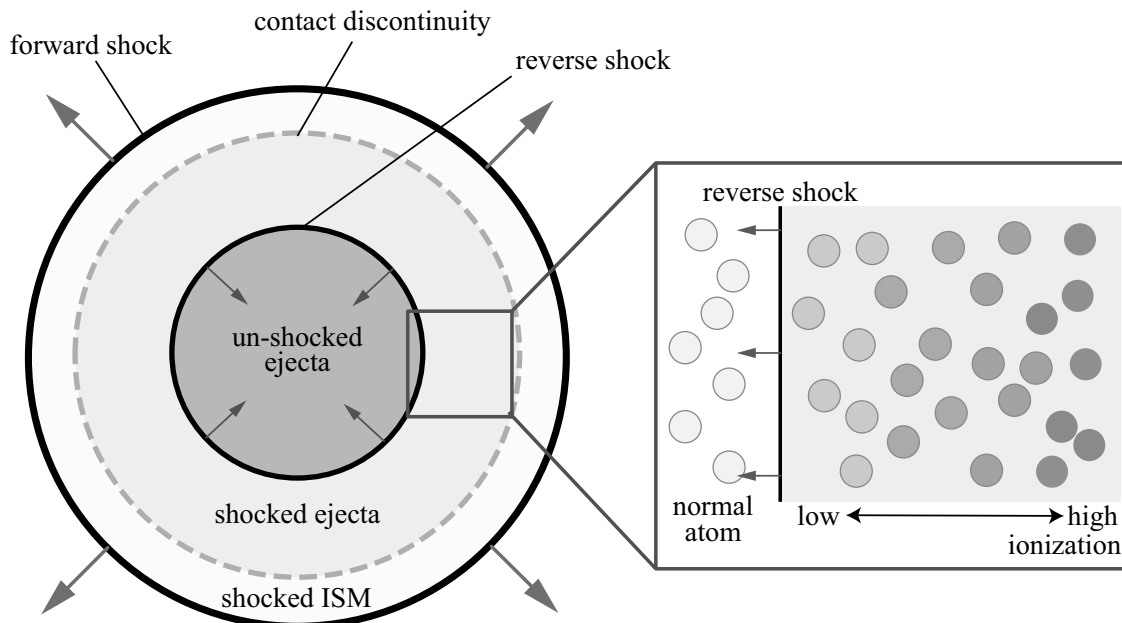


**Figure 2.4:** Schematic views of an SNR heating shock wave.

### 2.3.3 $M_{\text{ej.}} \lesssim M_{\text{ISM}}$ : Adiabatic phase (Sedov phase)

When  $M_{\text{ISM}}$  becomes greater than  $M_{\text{ej.}}$ , the kinetic energy of the ejecta in the SNR shell is transferred to the swept-up ISM. Therefore the forward shock is decelerated by the swept-up ISM, but the energy loss via radiation is still negligible at this stage. This phase can be regarded as adiabatic since the gas expands adiabatically while maintaining a constant total energy of the supernova ( $E_{\text{SN}}$ ). In this phase, the shock evolution can be approximated by a point explosion in a uniform medium. Sedov (1959) gave an exact self-similar solution for this phase. This phase is often called the ‘‘Sedov phase’’. The gas flow in this phase can be described using two parameters,  $E_{\text{SN}}$  and  $n_0$ . The radius,  $R_s$ , and velocity,  $v_s$ , of the forward shock wave and the mean plasma temperature of the shock front,  $T_s$ , are written as

$$R_s = 3.9 \times 10^{19} \left( \frac{t}{10^4 \text{ yr}} \right)^{2/5} \left( \frac{E_{\text{SN}}}{10^{51} \text{ erg}} \right)^{1/5} \left( \frac{n_0}{1 \text{ cm}^{-3}} \right)^{-1/5} \text{ [cm]}, \quad (2.38)$$

$$v_s = \frac{dR_s}{dt} = 4.9 \times 10^7 \left( \frac{t}{10^4 \text{ yr}} \right)^{-3/5} \left( \frac{E_{\text{SN}}}{10^{51} \text{ erg}} \right)^{1/5} \left( \frac{n_0}{1 \text{ cm}^{-3}} \right)^{-1/5} \text{ [cm s}^{-1}\text{]}, \quad (2.39)$$

$$T_s = 3.3 \times 10^6 \left( \frac{t}{10^4 \text{ yr}} \right)^{-6/5} \left( \frac{E_{\text{SN}}}{10^{51} \text{ erg}} \right)^{2/5} \left( \frac{n_0}{1 \text{ cm}^{-3}} \right)^{-2/5} \text{ [K]}. \quad (2.40)$$

Equation 2.40 shows that  $T_s$  decreases with time during this phase. In this phase, the density of the swept-up ISM is much higher than that of the ejecta, and hence the X-ray emission is dominated by the ISM. The Sedov phase continues for  $10^4$ – $10^5$  yr. By the end of this phase,  $\sim 70\%$  of the initial explosion energy has been transformed into the thermal energy of the swept-up ISM (Chevalier, 1974).

### 2.3.4 $M_{\text{ej.}} \ll M_{\text{ISM}}$ : Radiative cooling phase

As the plasma temperature decreases to  $\sim 10^6$  K, the ionized atoms start to capture free electrons and lose their energy by radiative emission. The cooling rate gradually increases and the evolution exits the adiabatic phase since the total energy in this phase is no longer equal to the initial energy,  $E_{\text{SN}}$ . The next stage is called the ‘‘radiative cooling phase’’. Assuming a non-relativistic monoatomic gas ( $\gamma = 5/3$ ), we obtain the radius of the shock in terms of the time as

$$R_s \propto t^{2/7}. \quad (2.41)$$

When the temperature further decreases, the pressure can be ignored and the cool shell expands while conserving radial momentum ( $v_s M_{\text{shell}} = \text{constant}$ , where  $M_{\text{shell}}$  is the mass of the shell). The shock expands as

$$R_s \propto t^{1/4}. \quad (2.42)$$

Finally, when the shock speed further decreases and becomes comparable to the velocity of the ISM ( $v \sim 10 \text{ km s}^{-1}$ ), the shell boundary of the SNR disperses into the ISM. This phase is called the “disappearance phase”.

## 2.4 Shock Wave Processes

When shock waves occur in the shell of an SNR expanding supersonically, there are several physical interactions between the shock waves and the materials. Here we introduce some of these shock wave processes.

### 2.4.1 Shock wave heating

The ejecta and swept-up ISM are heated by the shock waves mentioned in § 2.3. Figure 2.5 shows schematic views of the shock wave in the observer and shock rest frames. In the shock rest frame, the gas flows from the ISM side to the SNR side at the shock velocity  $v_s$ . Since the mass, momentum, and energy are conserved between the upstream

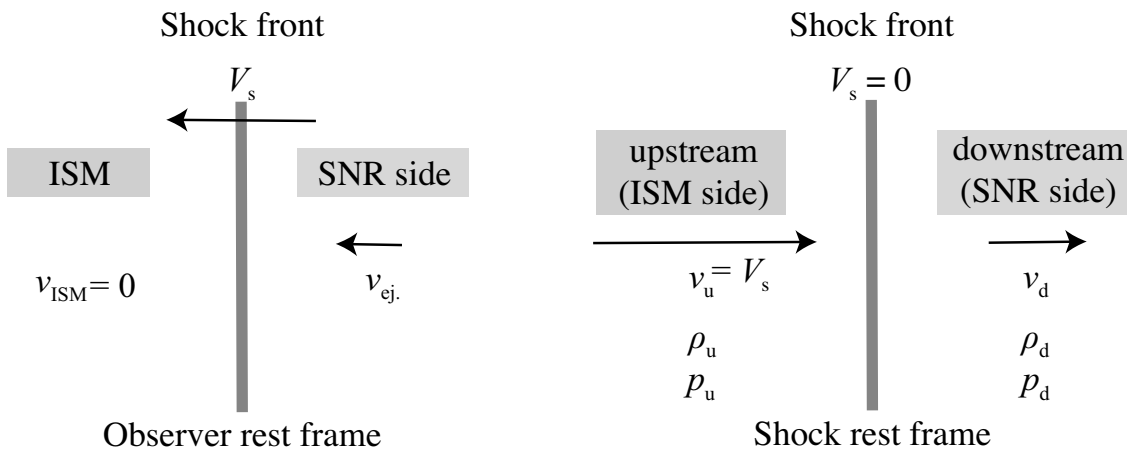


**Figure 2.5:** Schematic views of the shock front in the observer rest frame (left) and the shock rest frame (right).  $v_s$ ,  $\rho$ , and  $p$  are the shock velocity, density, and pressure, respectively.

and downstream sides of the shock front, the following equations hold:

$$\rho_u v_u = \rho_d v_d, \quad (2.43)$$

$$\rho_u v_u^2 + p_u = \rho_d v_d^2 + p_d, \quad (2.44)$$

$$\frac{1}{2}v_u^2 + h_u = \frac{1}{2}v_d^2 + h_d, \quad (2.45)$$

where  $\rho, v, p$ , and  $h$  are the density, velocity, pressure, and enthalpy, respectively. The subscripts u and d represent upstream and downstream, respectively. For an ideal gas,  $h$  can be written as

$$h = C_p T = \frac{\gamma}{(\gamma - 1)} \frac{p}{\rho}, \quad (2.46)$$

where  $\gamma$  is the specific heat ratio. These three equations, 2.43, 2.44, and 2.45, are known as the Rankine–Hugoniot relations. Now, we define the following parameters:

$$x = \frac{\rho_d}{\rho_u} = \frac{v_u}{v_d}, \quad y = \frac{p_d}{p_u},$$

$$a_u^2 = \frac{\gamma p_u}{\rho_u}, \quad \mathcal{M}_u = \frac{v_u}{a_u},$$

where  $a_u$  and  $\mathcal{M}_u$  are the speed of sound and the Mach number in the upstream, respectively. Rewriting equations 2.44, and 2.45, these equations become

$$\mathcal{M}_u^2 \left(1 - \frac{1}{x}\right) = \frac{y - 1}{\gamma}, \quad (2.47)$$

$$\mathcal{M}_u^2 \left(1 - \frac{1}{x^2}\right) = \frac{2(yx^{-1} - 1)}{\gamma - 1}. \quad (2.48)$$

Assuming  $x \neq 1$  and  $y \neq 1$ , equations 2.47 and 2.48 are solved for  $x$  and  $y$  to give

$$x = \frac{\rho_u}{\rho_d} = \frac{v_d}{v_u} = \frac{(\gamma + 1)\mathcal{M}_u^2}{(\gamma - 1)\mathcal{M}_u^2 + 2}, \quad (2.49)$$

$$y = \frac{p_d}{p_u} = \frac{2\gamma\mathcal{M}_u^2 - (\gamma - 1)}{\gamma + 1}. \quad (2.50)$$

From the state equation, the ratio of the temperatures,  $T_d/T_u$ , is given as

$$\frac{T_d}{T_u} = \frac{p_u \rho_u}{p_u \rho_d} = \frac{[2\gamma \mathcal{M}_u^2 - (\gamma - 1)][(\gamma - 1)\mathcal{M}_u^2 + 2]}{(\gamma + 1)^2 \mathcal{M}_u^2}. \quad (2.51)$$

Also, the velocities are written as

$$v_u^2 = \frac{1}{2\rho_u} \left[ (p_u(\gamma - 1) + p_u(\gamma + 1)) \right], \quad (2.52)$$

$$v_d^2 = \frac{1}{2\rho_u} \frac{[p_u(\gamma + 1) + p_u(\gamma - 1)]^2}{p_u(\gamma - 1) + p_u(\gamma + 1)}. \quad (2.53)$$

Assuming a strong shock ( $1 \ll \mathcal{M}_u$  or  $p_u \ll p_d$ ), equations 2.49, 2.51, 2.52, and 2.53 become

$$\frac{\rho_u}{\rho_d} = \frac{v_d}{v_u} = \frac{\gamma + 1}{\gamma - 1}, \quad (2.54)$$

$$\frac{T_d}{T_u} = \frac{p_u}{p_u} \frac{\gamma - 1}{\gamma + 1}, \quad (2.55)$$

$$v_u^2 = \frac{(\gamma + 1)p_u}{2\rho_u}, \quad (2.56)$$

$$v_d^2 = \frac{(\gamma - 1)^2 p_u}{2(\gamma + 1)\rho_u}. \quad (2.57)$$

The velocity of the upstream gas in the shock rest frame is equal to  $v_s$ . From equations 2.54 and 2.57, we obtain the mean post-shock temperature:

$$kT_d = \mu m_H \frac{p_u}{\rho_d} = \frac{2(\gamma - 1)}{(\gamma + 1)^2} \mu m_H v_s^2, \quad (2.58)$$

where  $k$  is the Boltzmann constant. Assuming a non-relativistic monoatomic gas,  $\gamma = 5/3$ , the density and velocity ratios of the upstream to the downstream are  $\rho_u/\rho_d = 4$  and  $v_d/v_u = 1/4$ , respectively. In addition, the post-shock temperature is given by

$$kT_d = \frac{3}{16} \mu m_H v_s^2. \quad (2.59)$$

The shock wave heating can be described as the conversion from kinetic energy to internal energy.

### 2.4.2 Collisionless shocks

Shock waves in astrophysical environments encounter media of very low densities, usually a few particles per  $\text{cm}^3$  or even lower. In this environment, collisional interactions between particles occur infrequently since the mean free path of Coulomb collisions is long. Therefore, collisionless processes involving collective interactions between particles and electromagnetic fields must be responsible for the shock formation (McKee, 1974). Collisionless shocks are ubiquitous in the Universe and are key to understanding the process of electron heating by shocks. However, the detailed fundamental mechanism remains to be completely elucidated. SNRs are ideal for studying this mechanism because we can observe the shock wave for a long time. Recently, by performing the spectral analysis of Tycho's SNR with *Suzaku*, Yamaguchi *et al.* (2014b) revealed an electron temperature behind the reverse shock that was much higher than expected. This result shows new evidence for efficient electron heating by collisionless shocks.

### 2.4.3 Cosmic-ray acceleration

Cosmic rays have been observed with energy of up to  $10^{20}$  eV, which we cannot achieve on Earth using human-made particle accelerators. The energy density of cosmic rays ( $\sim 1 \text{ eV cm}^{-3}$ ) is larger than that of starlight, the Galactic magnetic field, and the cosmic microwave background. Ever since the discovery of cosmic rays (Hess, 1912), their origin and acceleration mechanism have been a puzzle. SNR shock fronts are a possible origin of cosmic rays with energy below approximately  $10^{15}$  eV. Recent studies have reported evidence for cosmic ray acceleration in SNRs. Koyama *et al.* (1995) discovered synchrotron X-ray emission from the limb-brightened region of SN 1006 using the *ASCA* satellite, which revealed that cosmic ray electrons are accelerated by the shocks of SNRs. Several SNRs show strong synchrotron emission (RCW 86: Borkowski *et al.*, 2001; G347.3-0.5: Slane *et al.*, 1999; G266.2-1.2: Slane *et al.*, 2001). Bamba *et al.* (2003) discovered very thin (arcsecond width) filaments and clumps in the synchrotron emission near the shock front of SN 1006 using *Chandra*. Uchiyama *et al.* (2007) reported the discovery of the brightening and decay of X-ray hot spots in the shell of the SNR RX J1713.7-3946 on a one-year timescale. This rapid variability shows that the X-rays are produced by ultrarelativistic electrons through a synchrotron process and that electron acceleration does indeed take place in a strongly magnetized environment, perhaps causing the amplification of the magnetic field by a factor of more than 100. To reveal the origin and the acceleration

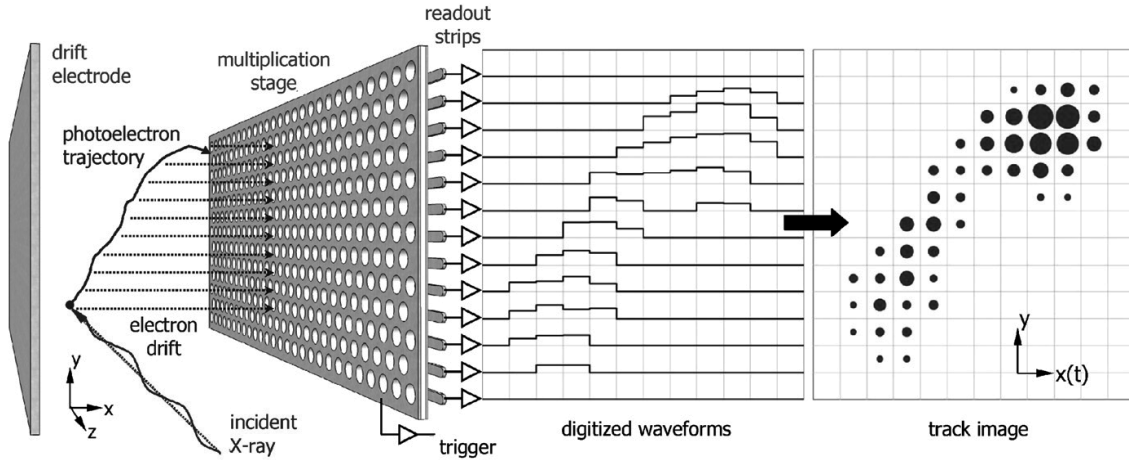


**Figure 2.6:** A schematic view of a TPC X-ray polarimeter of the *PRAXyS* mission (Black *et al.*, 2007). Incident X-rays enter the detector volume along the Z-axis. Charges collected on the strips are read-out and binned according to arrival time and strip number. Multiplying the arrival time by the drift velocity, the orthogonal 2-dimension photoelectron track images are reconstructed.

mechanism, we need to know the structure (e.g., direction and turbulence) of the magnetic field around an SNR shock.

## 2.5 X-ray Polarimetry Observations

Synchrotron X-ray radiation, which is an important key to understanding the cosmic-ray acceleration mechanism, can also create strong polarization. Polarized X-rays provide us with information about the structure of magnetic fields. Polarimetry is a powerful tool for astrophysical observations but has hardly been used to explore the X-ray band. Previous measurements were carried out in the 1970's using a sounding rocket and the *OSO-8* satellite. Only the Crab nebula has been detected by this satellite (Novick *et al.*, 1972; Weisskopf *et al.*, 1976, 1978).

The NASA *PRAXyS* satellite mission, Polarimeter for Relativistic Astrophysical X-ray Sources, was designed to detect linear X-ray polarization from SNRs, black holes, and neutron stars in the 2–10 keV energy band (Jahoda *et al.*, 2014). The *PRAXyS* payload includes a high-efficiency photoelectric gas polarimeter to measure X-ray linear polarization in the 2–10 keV range. The *PRAXyS* polarimeter is a gas proportional counter based on the time projection chamber (TPC) technique. Figure 2.6 illustrates the readout concept of the polarimeter. When an incident X-ray interacts with a gas molecule, a

photoelectron is ejected preferentially in the direction of the electric field of the incident X-ray, which is defined as the polarization direction. The emitted angle has the probability distribution  $\cos^2(\phi - \phi_0)$ , where  $\phi$  and  $\phi_0$  are the polarization-sensitive azimuthal angle and source-polarized direction, respectively. An ejected photoelectron passes through the gas and forms an ionized electron cloud along the track in a uniform electric field between the drift electrode and a micro-pattern gas electron multiplier (GEM; Tamagawa *et al.*, 2006, 2009). The GEM structure is a parallel-plate capacitor with many through holes, which have a hole pitch of  $140\ \mu\text{m}$ , a hole diameter of  $70\ \mu\text{m}$ , and a thickness of  $100\ \mu\text{m}$ . The electrons drift to the GEM holes, where they are amplified by an electron avalanche, and then are collected by  $121\ \mu\text{m}$ -pitch readout strips under the GEM. The charge signal on each strip is read by the APV25 readout ASIC with a 20 MHz sampling rate (French *et al.*, 2001). A two-dimensional track image is constructed using the strip position and the arrival time information. The track image is analyzed to determine the direction of ejection. The target gas used in the *PRAXyS* polarimeter is pure dimethyl ether (DME) because of its lower rate of diffusion and lower drift velocity than the other known gases used in proportional counters.

One of the key points of the *PRAXyS* polarimeter is the performance of the GEM. We evaluated the performance of the same type of GEM foil as that used in the *PRAXyS* polarimeter. The charge sharing between the GEM and the readout electrodes was measured as a function of the electric field (Takeuchi *et al.*, 2012). Also, we investigated the gain uniformity and linearity of the energy scale (Takeuchi *et al.*, 2014a) and the gain performance at low gas pressures (Takeuchi *et al.*, 2014b). We found that these results satisfy the minimum requirements of *PRAXyS*. In the near future, we anticipate that the GEM will provide high-quality polarization data from observations of astrophysical accelerators such as SNRs to shed light on the poorly understood physics of diffusive shock acceleration and collisionless shocks.

## Chapter 3

# THERMAL PLASMAS OF SNRS

In this chapter, we explain the properties of optically thin thermal plasma, and introduce ionizing, equilibrium, and recombining plasmas in SNRs. Then, we discuss the X-ray emission mechanism of these plasma states associated with SNRs.

### 3.1 Classification of Plasma State

In a thin thermal plasma, we assume that the electron distribution obeys the Maxwell-Boltzmann distribution law

$$f(v) = 4\pi v_e^2 \left( \frac{m_e}{2\pi k T_e} \right)^{3/2} \exp\left( -\frac{m_e v_e^2}{2k T_e} \right), \quad (3.1)$$

where  $f(v)$ ,  $m_e$ ,  $v_e$ , and  $k$  are the velocity probability density, the mass of an electron, the velocity of an electron, and the Boltzmann constant ( $1.38 \times 10^{-23} \text{ J K}^{-1}$ ), respectively. To express the plasma condition, we define the ionization temperature,  $T_z$ , as a characteristic, which indicates the ionization degree of an ion. We can classify a plasma into three states using two temperatures,  $T_e$  and  $T_z$ : the underionized, ionization equilibrium, and overionized states. Underionized (overionized) means a lower (higher) ionization stage than that predicted by equilibrium. There are three ionization processes: electric impact ionization, photoionization, and autoionization. In general, the photoionization effect is negligible owing to its weakness relative to electron impact ionization in a thin thermal plasma. On the other hand, there are three recombination processes: three-body recombination, radiative recombination, and dielectric recombination. Each process is the inverse of one of the previous ionization processes. From the viewpoint of the collisional atomic process

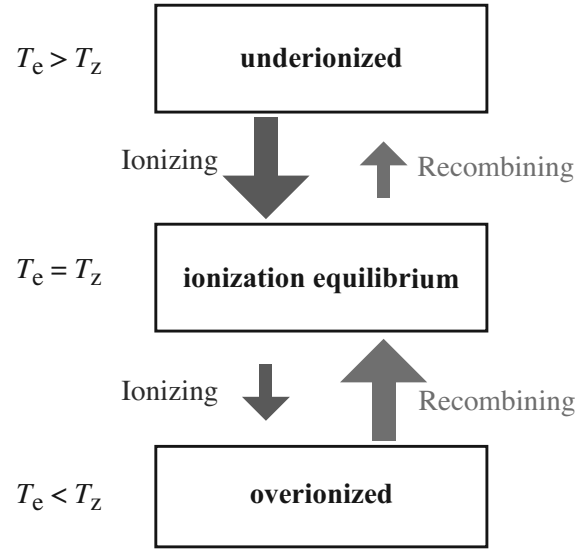


**Figure 3.1:** A schematic view of plasma states.

for thermal emission, a plasma condition can be classified into the above three states by the relation between the thermal energy and the energy distributed in the ionization state. We summarize these states in detail as follows and in figure 3.1.

1.  $T_e > T_z$ : underionized (lower ionization stage than that predicted by equilibrium)  
The electrons have sufficient thermal energy to ionize atoms. Ionization is more dominant than recombination in this condition. The plasma in this condition can usually be found in X-ray spectra of SNRs, particularly young SNRs.
2.  $T_e = T_z$ : ionization equilibrium  
There is a balance between the ionization rate and the recombination rate. The plasma in this condition is known as “collisional ionization equilibrium (CIE) plasma”. This plasma has been observed in old ( $\sim 10^4$  yr) SNRs.
3.  $T_e < T_z$ : overionized (higher ionization stage than that predicted by equilibrium)  
This is the opposite of the underionized case. The recombination process occurs chiefly in this state. Plasma in this condition has been observed only recently in some SNRs. Recent X-ray observations have revealed several SNRs in this condition (e.g., W49B: Ozawa *et al.*, 2009; IC 443: Yamaguchi *et al.*, 2009; G359.1–0.5: Ohnishi *et al.*, 2010; W28: Sawada & Koyama, 2012; G346.6–0.2: Yamauchi *et al.*, 2013; 3C 391: Sato *et al.*, 2014; W44: Uchida *et al.*, 2012; N49: Uchida *et al.*, 2015).

After the shock heating, the shocked materials, which were initially neutral, gradually lose electrons one-by-one through collisions with free electrons. This phase is known as the non-equilibrium ionization (NEI) state and continues until the ionization state is in equilibrium with the thermal electrons (CIE condition).

Masai (1984, 1994) derived the characteristic timescale for a plasma to reach CIE. The ionization rate equation is obtained using the element atomic number,  $Z$ , as follows:

$$\frac{df_z}{d(n_e t)} = S_{Z-1} f_{Z-1} + (S_Z + \alpha_Z) f_Z + \alpha_{Z+1} f_{Z+1}, \quad (3.2)$$

$$\sum_{z=0}^Z f_z = 1, \quad (3.3)$$

where  $f_Z$  is the ionization fraction of the element corresponding to the loss of  $Z - 1$  electrons.  $S_Z$  and  $\alpha_Z$  are the ionization and recombination rate coefficients of the  $Z$ th ion, respectively. In the CIE condition,  $df_z/d(n_e t) = 0$ . The time to arrive at CIE is estimated as  $n_e t \approx 10^{12} \text{ cm}^{-3} \text{ s}$ . If  $n_e = 1 \text{ cm}^{-3}$ , a typical value in an SNR, the plasma takes  $\sim 3 \times 10^4 \text{ yr}$  to reach the CIE condition. Therefore, most SNRs should still be in non-ionization equilibrium.

## 3.2 X-ray Emission

Thin thermal plasma in SNRs emits X-rays. Figure 3.2 shows the predicted X-ray spectrum from a thin thermal plasma in the CIE condition with  $T_e = 1 \text{ keV}$  without the detector response. For simplicity, the abundances of H and Si are fixed to the same as those of the Sun, and other element abundances are fixed to zero. External electric and magnetic field effects are ignored. The spectrum is composed of a continuum and many emission lines. In this section, we summarize the X-ray emission processes.

### 3.2.1 Continuous emissions

There are three radiative processes for continuum emissions: thermal bremsstrahlung, radiative recombination, and two-photon radiation. In CIE plasma of  $\sim 1 \text{ keV}$ , thermal bremsstrahlung is the most dominant continuum emission. However, at low ( $\sim 0.1 \text{ keV}$ ) temperatures, the radiative recombination continuum is larger relative to the thermal bremsstrahlung. Also, in the overionized state, the radiative recombination continuum features may be more pronounced because the majority of the ions recombine.

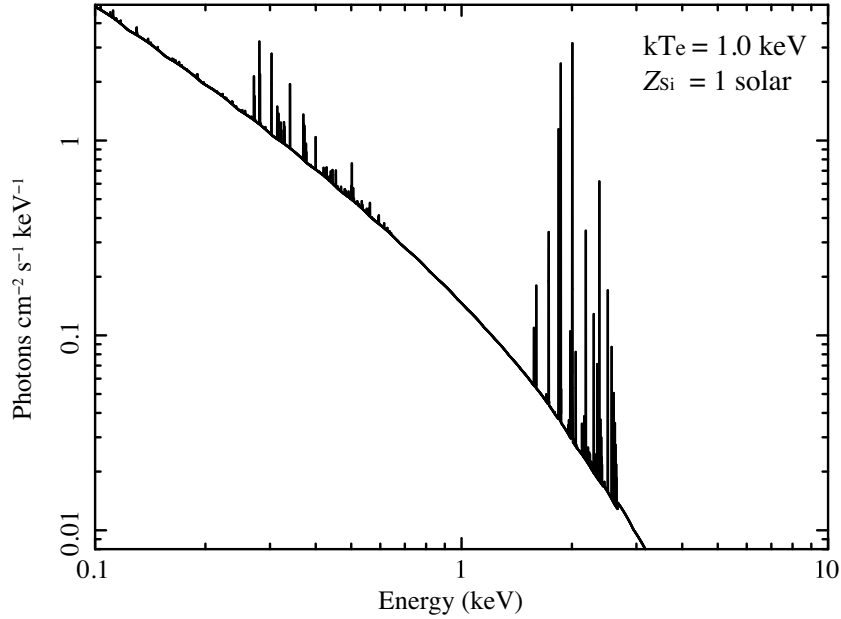


**Figure 3.2:** Predicted X-ray spectrum from thin thermal plasma of Si in the CIE condition without the detector response. Assuming the electron temperature  $T_e=1.0$  keV. For simplicity, we fixed the abundances except for H and Si to zero. Most of the continuum emission is due to the bremsstrahlung radiation. The figure is derived from the APEC code.

### Thermal bremsstrahlung

Bremsstrahlung is electromagnetic radiation produced by the deceleration of a charged particle when deflected by another charged particle. Electrons emit photons by bremsstrahlung in the electric field of an atomic nucleus as shown in figure 3.3. The emission power in an isotropic thermal distribution is expressed as

$$\begin{aligned} \frac{dW}{dV dt d\nu} &= \frac{32\pi e^6}{3mc^3} \left( \frac{2\pi}{3km} \right)^{1/2} T_e^{-1/2} Z^2 n_e n_i \overline{g_{ff}} \exp\left(\frac{-h\nu}{kT_e}\right) \\ &= 6.8 \times 10^{-38} T_e^{-1/2} Z^2 n_e n_i \overline{g_{ff}} \exp\left(\frac{-h\nu}{kT_e}\right) \quad [\text{erg s}^{-1} \text{cm}^{-3} \text{Hz}^{-1}], \quad (3.4) \end{aligned}$$

where  $e$ ,  $m$ ,  $c$ ,  $n_e$ , and  $n_i$  are the electron charge, electron mass, light speed, and the densities of the electron and ion, respectively.  $\overline{g_{ff}}$  is the velocity-averaged Gaunt factor. For typical thermal plasma emitting X-rays,

$$\overline{g_{ff}} = \left( \frac{3 kT_e}{\pi h\nu} \right)^{1/2}. \quad (3.5)$$

The factor  $T_e^{-1/2}$  in equation 3.4 originates from the fact that  $dW/(dV dt d\nu) \propto v^{-1}$ . From equation 3.4, the power of bremsstrahlung emission increases as the density and/or temperature increases.

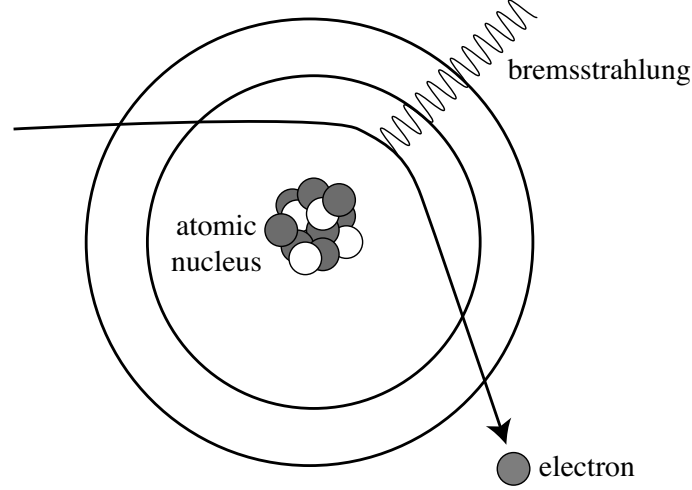


**Figure 3.3:** A schematic view of bremsstrahlung emission.

### Radiative recombination

Radiative recombination is the process of emitting a photon when a free electron collides and recombines with an ion. The energy of the emitted photon,  $E_{\text{RRC}}$ , is obtained as

$$E_{\text{RRC}} = E_{\text{free}} - E_{\text{edge}}, \quad (3.6)$$

where  $E_{\text{free}}$  and  $E_{\text{edge}}$  are the kinetic energy of a free electron and the binding energy of the  $n$  level in an ion, respectively. Since  $E_{\text{free}}$  is not quantized, this radiation forms a continuous spectrum with sharp edges at the binding energies of the levels. The spectrum of this radiation is called the “radiative recombination continuum (RRC)”. Figures 3.4 (a) and (b) show a schematic view of the emission mechanism for the RRC and the predicted RRC spectrum, respectively.

The power emitted per keV by this process is described in Tucker & Gould (1966) as

$$\frac{dE}{dV dt d\omega} = \frac{dP}{dE} = n_e n_{Z,j+1} v_e E_\gamma \cdot \sigma^{\text{rec}}(E_e) \cdot \frac{f(v) dv}{dE}, \quad (3.7)$$

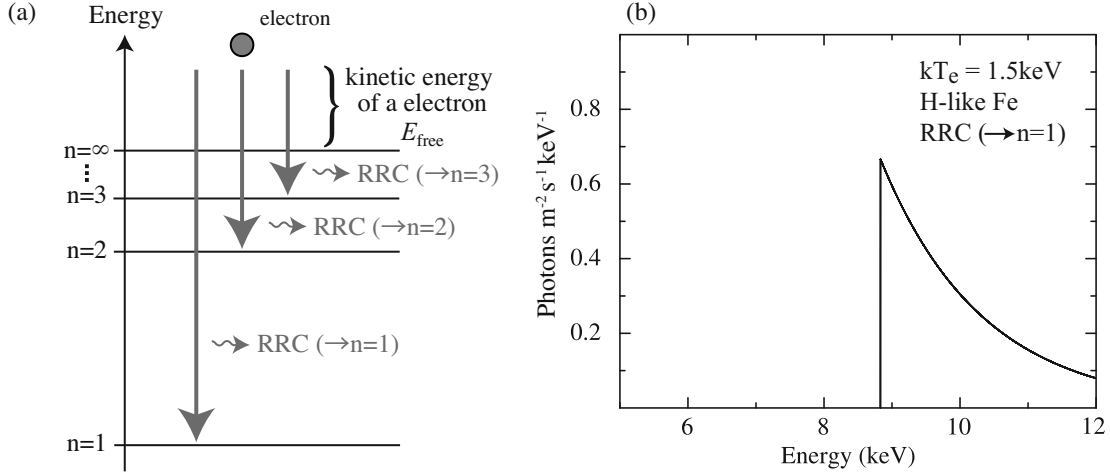


**Figure 3.4:** (a) A schematic view of the emission mechanism for RRC. (b) Predicted RRC spectrum made by H-like Fe ions. The energy of the edge corresponds to K-shell binding energy. Figure (b) is taken from Ozawa (2010).

where  $n_{Z,j+1}$ ,  $E_\gamma$ , and  $\sigma^{\text{rec}}(E_e)$  are the density of an ion with atomic number  $Z$  and ionization state  $j + 1$ , the energy of the emitted photon, and the recombination cross section to level  $n$  at the electron energy  $E_e$ , respectively. We assume that  $f(v)$  is the Maxwell–Boltzmann distribution.

We can also rewrite equation 3.7 using the binding energy,  $E_{\text{edge}}$ , of the ion for an electron and the Maxwell–Boltzmann equation. Equation 3.7 becomes

$$\frac{dW}{dE} = n_e n_{Z,j+1} \cdot 4 \left( \frac{E_\gamma - E_{\text{edge}}}{kT_e} \right) (2\pi m_e kT_e)^{-1/2} \cdot \sigma^{\text{rec}}(E_\gamma - E_{\text{edge}}) \times E_\gamma \exp\left( - \frac{E_\gamma - E_{\text{edge}}}{kT_e} \right). \quad (3.8)$$

When  $T_e \ll E_{\text{edge}}$ , the following expression for equation 3.8 is obtained:

$$\frac{dW}{dE} \propto \exp\left( - \frac{E_\gamma - E_{\text{edge}}}{kT_e} \right). \quad (3.9)$$

### Two-photon radiation

The two-photon process is known as one of the bound-bound transitions. Upon the simultaneous absorption of two photons of identical or different energies to excite an atom from one state to a higher energy state, such radiation occurs. The energy of each photon of the pair is not determined, while the sum of the energies of the two emitted photons conserves the transition energy. For this reason, the spectrum of this radiation is very

broad and continuous.

### 3.2.2 Emission lines

The energy and flux of an emission line depend on the ionization state and electron temperature. We explain this feature in this subsection. Emission lines are caused by the transition of an electron between two quantized energy states ( $n$  and  $n'$ ) in an ion, therefore they are called either emission lines or bound-bound emissions. In the case of a H-like ion, which has an electron similarly to hydrogen, we obtain the state formula known as the Rydberg formula as follows:

$$E_n = R_y \left( \frac{1}{n^2} - \frac{1}{n'^2} \right), \quad (3.10)$$

where  $R_y$  is the Rydberg constant ( $=13.6$  eV) and  $n < n'$ . For heavy elements,  $E_n$  depends on the atomic number,  $Z$ , and is written as

$$E_n \sim Z^2 R_y \left( \frac{1}{n^2} - \frac{1}{n'^2} \right). \quad (3.11)$$

These H-like transitions are known as the ‘‘Lyman series’’. The transitions are named Ly $\alpha$  ( $n = 2 \rightarrow 1$ ), Ly $\beta$  ( $n = 3 \rightarrow 1$ ), Ly $\gamma$  ( $n = 4 \rightarrow 1$ ), and so forth.

The emission line for an ion state with two or more electrons is not as simple as that for a H-like ion. For example, He-like ions emit three intense lines: resonance ( $1s2p \ ^1P_1 \rightarrow 1s^2 \ ^1S_0$ ), forbidden ( $1s2p \ ^3S_1 \rightarrow 1s^2 \ ^1S_0$ ), and intercombination ( $1s2p \ ^3P_{2,1} \rightarrow 1s^2 \ ^1S_0$ ) transition lines. In this thesis, the sum of the K $\alpha$  lines of a He-like ion is denoted as ‘‘He $\alpha$ ’’ ( $n = 2 \rightarrow 1$ ). He-like K $\beta$  and He-like K $\gamma$  lines are denoted as ‘‘He $\beta$ ’’ ( $n = 3 \rightarrow 1$ ) and ‘‘He $\gamma$ ’’ ( $n = 4 \rightarrow 1$ ), respectively. The H-like and He-like line energies for major elements are listed in table 3.1.

The final ionization state of ions strongly depends on the electron temperature  $T_e$ . The ion fractions of major elements as a function of electron temperature in the CIE state are shown in figure 3.5. The range of the electron temperature is 0.01–20 keV. When  $T_e$  is higher, ions are stripped of more electrons. The speed of ionization depends on the elapsed time since the gas was heated by a shock,  $t$ , and the electron density,  $n_e$  which are very difficult to measure. We can use the ionization parameter  $n_e t$  (the product of  $n_e$  and  $t$ ) as a substitute for the parameter of the ionization speed. Figure 3.6 shows the emission

---

<sup>1</sup>HP: <http://www.atomdb.org>

**Table 3.1:** K-shell line energies of H-like and He-like ions\*.

	H-like ion			He-like ion				
	Ly $\alpha$	Ly $\beta$	Ly $\gamma$	He $\alpha(r)$ <sup>†</sup>	He $\alpha(f)$ <sup>†</sup>	He $\alpha(i)$ <sup>†</sup>	He $\beta$	He $\gamma$
Ne	1022	1211	1277	921	905	914	1073	1127
Mg	1472	1745	1840	1252	1330	1343	1579	1660
Si	2006	2377	2506	1865	1840	1854	2183	2294
S	2623	3107	3277	2461	2431	2447	2884	3033
Ar	3323	3936	4151	3140	3104	3124	3685	3875
Ca	4101	4863	5129	3908	3866	3887	4582	4819
Fe	6966	8266	8732	6702	6641	6670	7798	8217

\* The unit is eV.

<sup>†</sup> He $\alpha(r)$ , He $\alpha(f)$ , and He $\alpha(i)$  indicate resonance, forbidden, and intercombination lines, respectively.

This energy list is from *AtomDB*<sup>1</sup>.

of a weighted line center energy for each element as a function of  $n_e t$ .

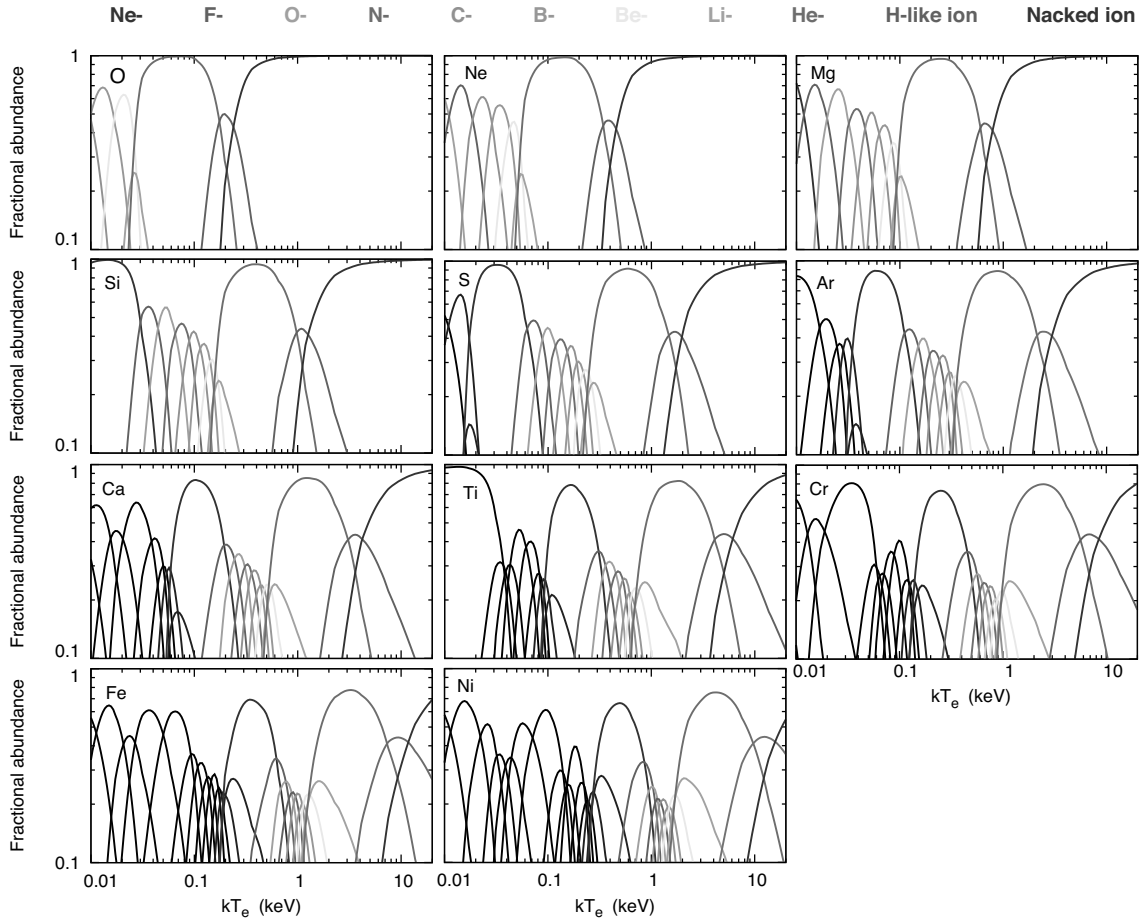


**Figure 3.5:** Ion fractions of several elements in collisional ionization equilibrium as a function of the electron temperature. Color lines represent the ionization state of the ion until Ne-like ion. Black lines show the ions with lower ionization state then Na-like. These figures are derived from the *AtomDB*.

The line flux ratio allows us to obtain further information. When the amount of H-like ions is larger than that of He-like ions, the emission from a H-like ion (e.g.  $\text{Ly}\alpha$  and  $\text{Ly}\beta$  lines) becomes dominant. The  $\text{Ly}\alpha/\text{He}\alpha$  flux ratio directly depends on the ionization state of the plasma. Figure 3.7 shows the  $\text{Ly}\alpha/\text{He}\alpha$  flux ratio for some elements as a function of  $n_e t$ .

The line flux ratio of K-shell emission from the same ion state (e.g.,  $\text{He}\beta/\text{He}\alpha$  or  $\text{Ly}\beta/\text{Ly}\alpha$  flux ratio) depends on the electron temperature. Now, we consider that the state of this atom has a Boltzmann distribution. The approximate relationship for the

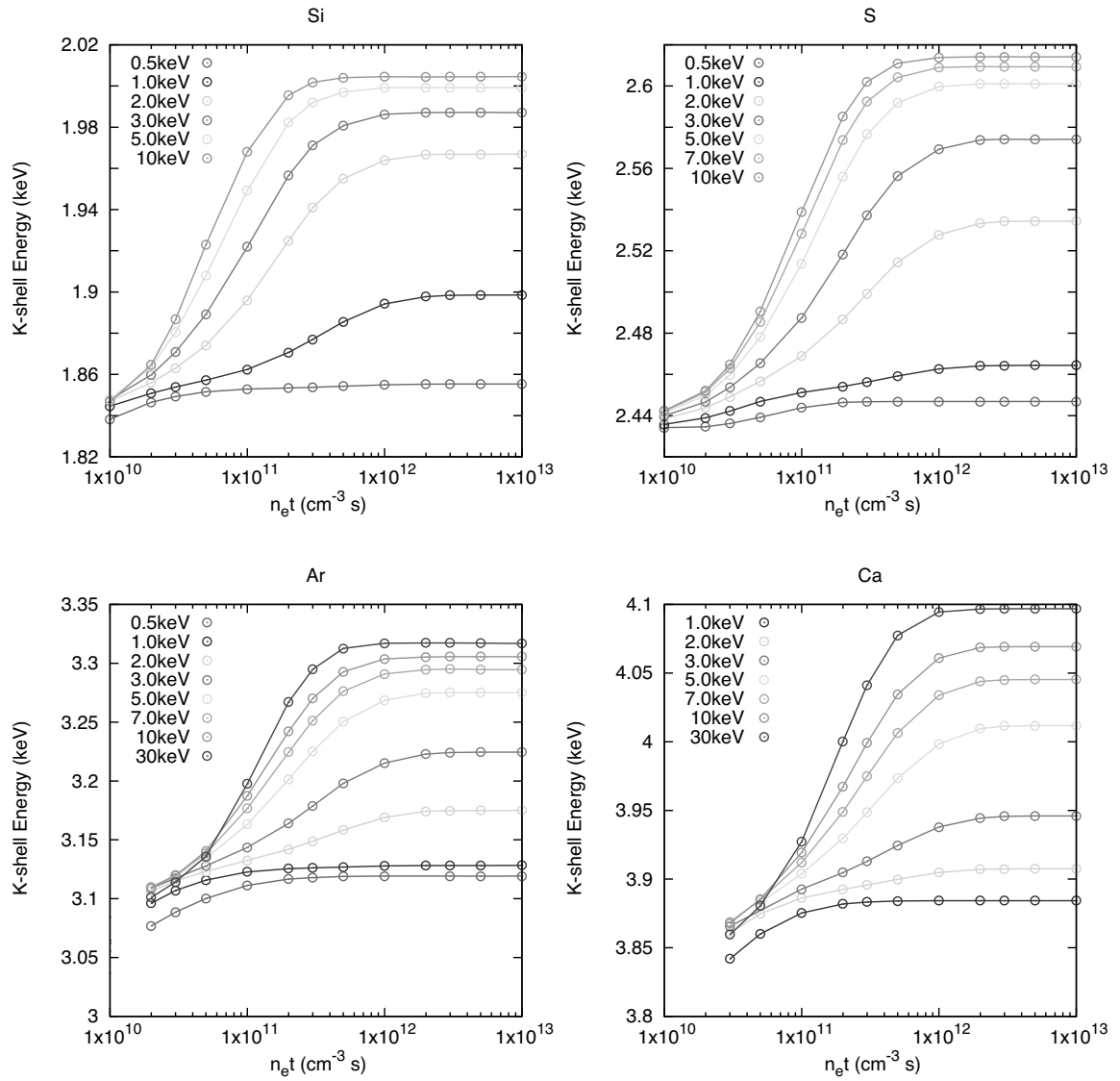


**Figure 3.6:** Centroid K-shell energy as a function of ionization state  $n_e t$  for Si, S, Ar, and Ca. Colors shows the several electron temperatures. These figures are derived from the *AtomDB*.

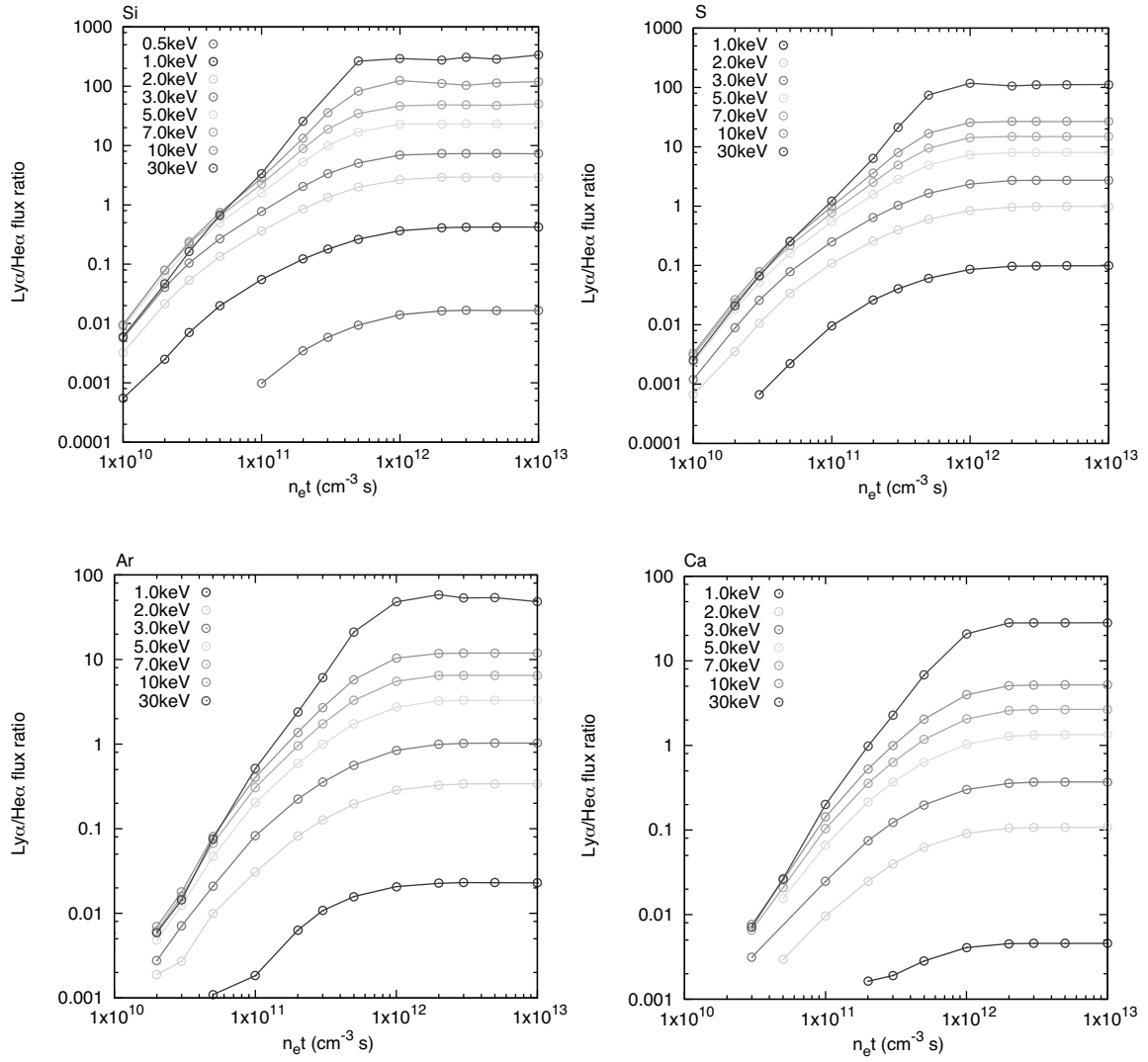


**Figure 3.7:**  $Ly\alpha/He\alpha$  flux ratio as a function of ionization state  $n_e t$  for Si, S, Ar, and Ca. Colors shows the several electron temperatures. These figures are derived from the *AtomDB*.

flux ratio (e.g.,  $F_{He\beta}/F_{He\alpha}$ ) for each emission line is

$$\begin{aligned}
 \frac{F_{He\beta}}{F_{He\alpha}} &\propto \frac{n_{He\beta}}{n_{He\alpha}} \\
 &\propto \frac{\exp(-E_{He\beta}/kT_e)}{\exp(-E_{He\alpha}/kT_e)} \\
 &\propto \exp(-1/kT_e),
 \end{aligned} \tag{3.12}$$

where  $n_{He\alpha}$  and  $n_{He\beta}$  are the numbers of electrons transiting from one excited state to a lower excited one for the  $He\alpha$  and  $He\beta$  lines, respectively. To obtain the electron temperature, the most direct method is to use the line flux ratio. In figures 3.8 and 3.9, we show the  $He\beta/He\alpha$  and  $Ly\alpha/He\alpha$  flux ratios as a function of the electron temperature

for Si, S, Ar, and Ca, respectively.

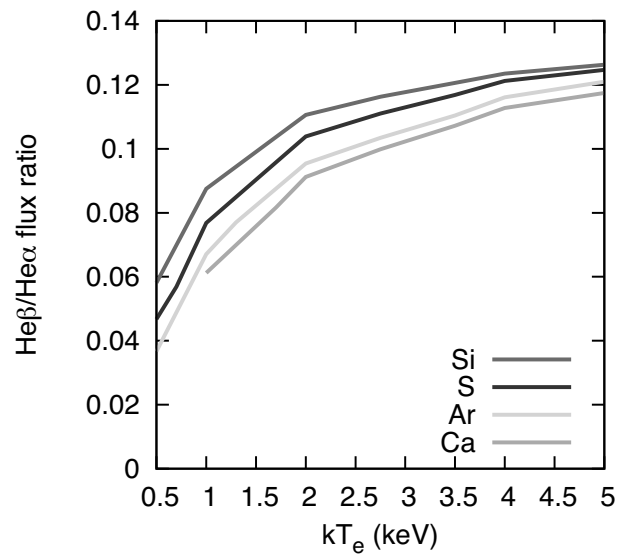


**Figure 3.8:**  $\text{He}\beta/\text{He}\alpha$  flux ratio as a function of the electron temperature for Si, S, Ar, and Ca in CIE state. This figure is derived from the *AtomDB*.

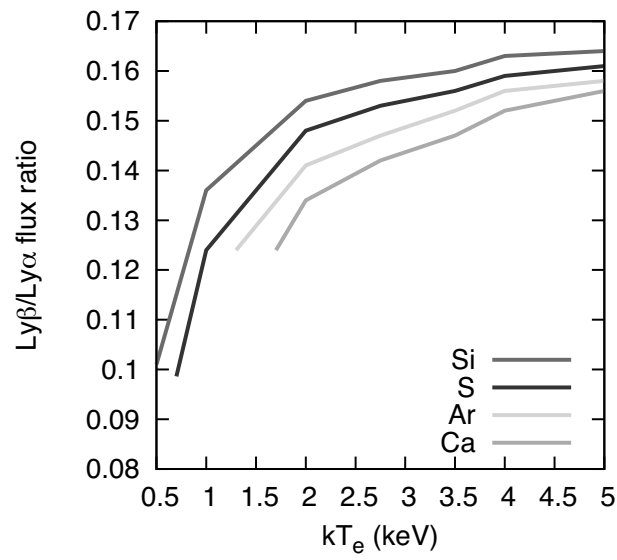


**Figure 3.9:**  $Ly\beta/Ly\alpha$  flux ratio as a function of the electron temperature for Si, S, Ar, and Ca in CIE state. This figure is derived from the *AtomDB*.



## Chapter 4

# X-RAY OBSERVATIONS OF SNRS

At present, a total of  $\sim 300$  SNRs are known in our Galaxy (Green, 2014). In the LMC and SMC, the nearest irregular dwarf galaxies from us, 77 SNRs are also known from multiwavelength observations (Badenes *et al.*, 2010). Most of them were found by radio and X-ray observations. SNRs have two merits for observing chemical abundances. First, the radiation from SNRs is mainly from the optically thin hot plasma. Thus, we can directly observe through the entire structures of SNRs. Second, we can observe SNRs any time and as many times as we would like since they are luminous for typically over  $10^4$  yr, unlike SNe, which are bright for about a month. The progenitor type is one of the most important pieces of information. However, often their type is still unknown. In this chapter, we explain the X-ray observations of SNRs and the method of determining the progenitor type using X-ray data.

### 4.1 Compact Objects

About 30% of X-ray-detected SNRs have been identified as CC SNRs. CC SNRs are distinguished by their association with a compact object (neutron star or black hole) because a neutron star or a black hole remains in the center of the SNR when a CC SNR explodes as explained in § 2.1.2. The origin of the X-rays is synchrotron radiation from a neutron star or its nebula. A highly magnetized and rapidly rotating neutron star becomes a pulsar. The pulsar emits a powerful beam of electromagnetic radiation, which can be observed from Earth. Also, a pulsar wind composed of charge particles accelerated

by pulsar blows from a neutron star, which sweeps up the ISM around it. This form of nebula is called a pulsar wind nebula (PWN). A typical PWN is the Crab nebula, which was created in the year 1054 AD and is shown in figure 4.1. At the centre of the Crab nebula, the pulsar emits pulses of radiation with a frequency of 33 Hz.

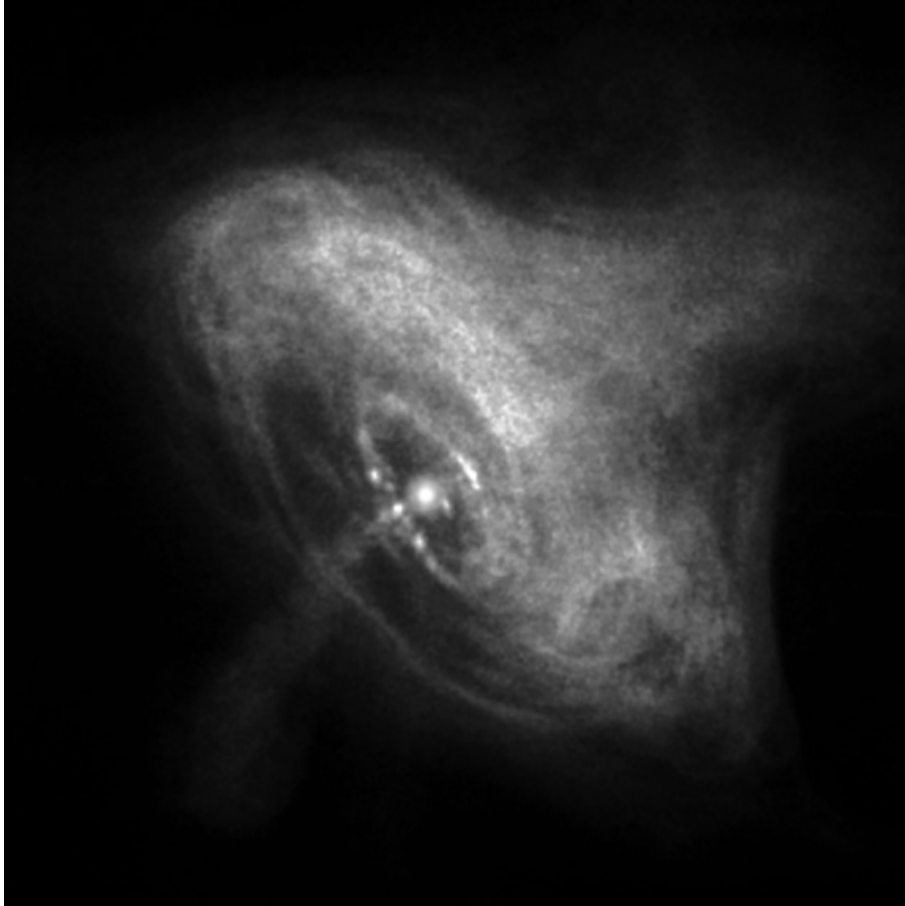


**Figure 4.1:** X-ray image of the Crab nebula and its pulsar. This figure is taken by *Chandra*. This image shows dynamic rings, wisps, and jets around the pulsar. The inner ring is about one light year across. Scale: square region is  $2.24'$  across. Image credit: NASA/CXC/ASU/J.

## 4.2 X-ray Abundance

The general method used to determine the SN type is to examine the difference in the abundance pattern between Type Ia and CC SNe as explained in § 2.1.1 and 2.1.2. In this section, we introduce two SNR results for Type Ia and CC SNRs as examples. N103B, one of the LMC SNRs, is one of the brightest known radio and X-ray sources. The *ASCA* observation of this remnant shows strong emission lines of Si, S, Ar, Ca, and

Fe, while the K-shell emission from O, Ne, and Mg is weak (Hughes *et al.*, 1995). The abundance pattern is consistent with the nucleosynthesis products of Type Ia (Nomoto *et al.*, 1984; Iwamoto *et al.*, 1999). Lewis *et al.* (2003) confirmed that this SNR is Type Ia from *Chandra* observations. As shown in figure 4.2, there are strong emission lines of metals produced by Type Ia. On the other hand, figure 4.3 shows X-ray images and the spectrum of SNR 0049–73.6. Emission lines of O and Ne were found in the spectrum of the central nebula of SNR 0049–73.6 in the SMC (Hendrick *et al.*, 2005). On the basis of this ejecta composition, this SNR was identified as a CC SNR.

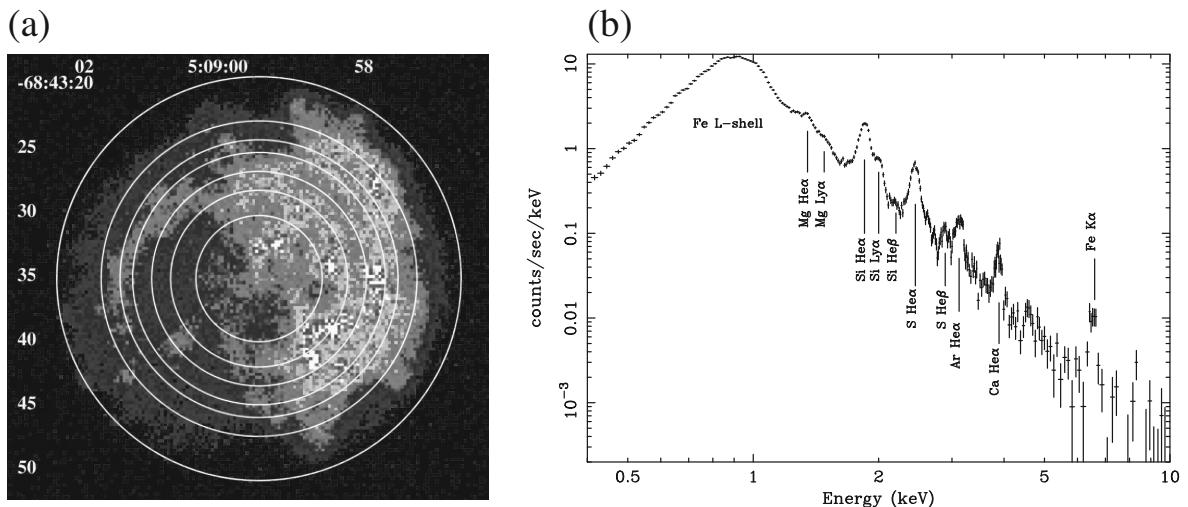


**Figure 4.2:** (a) *Chandra* X-ray intensity map of N103B in the LMC. Linear scaling ranging from 0 (black) to 75 (white) counts pixel<sup>-1</sup>. (b) Integrated spectrum. The main emission lines are labeled. All figures taken from Lewis *et al.* (2003).

### 4.3 Morphology

Lopez *et al.* (2009, 2011) performed a systematic analysis of X-ray line emission morphology with *Chandra* for young SNRs including Type Ia and CC SNRs. They carried out a multipole statistical analysis of the X-ray surface brightness distribution of SNRs. The circular asymmetry provides the normalized third moment,  $P_3/P_0$ , whereas the mirror asymmetry of the emission gives large values for  $P_2/P_0$ . Soft X-ray images of all the analyzed SNRs are shown in figure 4.4. Figure 4.5 shows the results of a statistical analysis of the soft X-ray and Si XIII emission images. Lopez *et al.* (2011) found that Type Ia SNRs clearly occupy a different area of the plot from CC SNRs. The CC SNRs are sta-

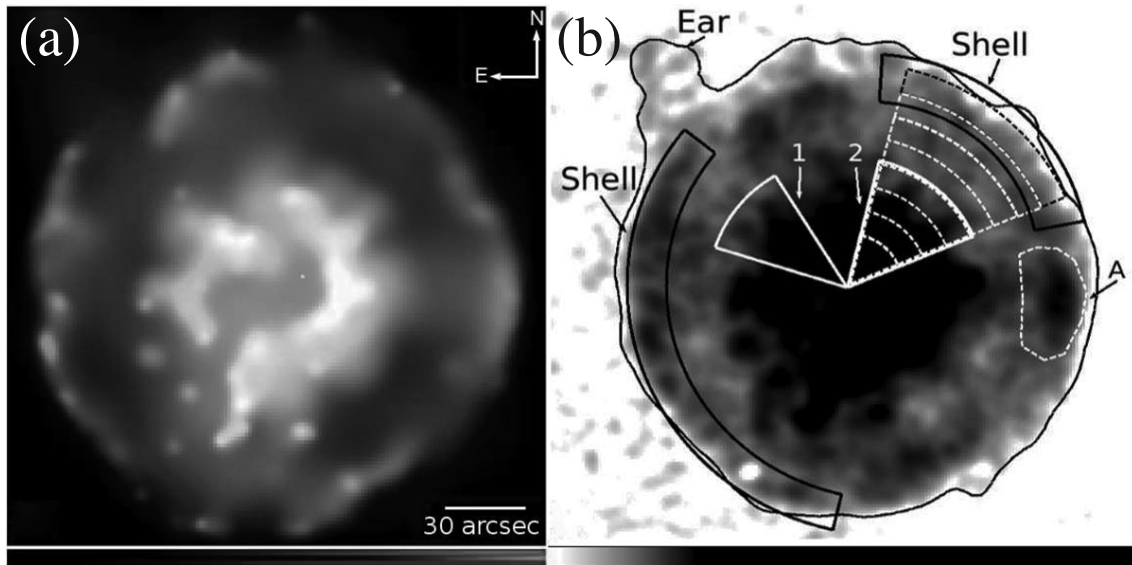


**Figure 4.3:** (a) *Chandra* X-ray image of SNR 0049–73.6 in the SMC. Color codes are red: 0.3–0.7 keV, green: 0.7–1.1 keV, and blue: 1.1–3.0 keV. (b) A gray-scale broadband image of this SNR. (c) Best-fit models and residuals of X-ray spectra from Region 1 (black) and Region 2 (brown). All figures taken from Schenck *et al.* (2014).

tistically more elongated than the Type Ia SNRs. This result is helpful for understanding the distinct explosion mechanisms and circumstellar material structures of Type Ia and CC SNRs.

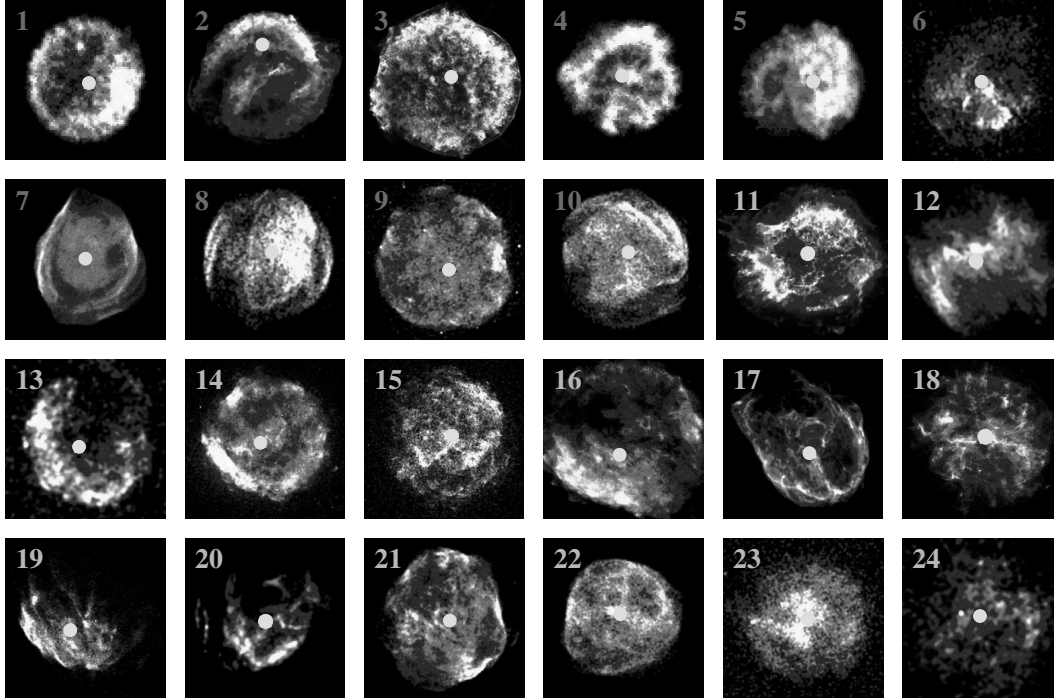


**Figure 4.4:** *Chandra* soft X-ray images (0.5–2.1 keV) of 24 SNRs in our Galaxy and the LMC. The cyan circles mark the full-band centroids of each SNR use in their method. Red and light blue numbers denote Type Ia and CC SNRs, respectively. All figures taken from Lopez *et al.* (2011). Note: (1)0509–67.5, (2)Kepler, (3)Tycho, (4)0519–69.0, (5)N103B, (6)G336.2–0.7, (7)DEML71, (8)0548–70.4, (9)G272.2–3.2, (10)0534–69.9, (11)Cas A, (12)W49B, (13)G15.9+0.2, (14)G11.2–0.3, (15)Kes 73, (16)RCW 103, (17)N132D, (18)G292.0+1.8, (19)0506–68.0, (20)Kes 79, (21)N49B, (22)B0453–685, (23)N206, (24)G344.7–0.1.

#### 4.4 Property of Fe K-shell Emission

Yamaguchi *et al.* (2014a) suggested a new observational diagnostic to decide the progenitor type and the constraint of the ambient medium density of SNRs using only Fe K-shell emission. They analyzed the *Suzaku* observations of 23 young or middle-aged SNRs and detected Fe  $K\alpha$  emission. As shown in figure 4.6, the centroid energy of Fe  $K\alpha$  for each SNR clearly distinguishes CC SNRs from Type Ia SNRs. The Fe ejecta in the CC SNRs are more highly ionized than those in the Type Ia SNRs. Since the selected SNRs have similar ages and sizes, this large difference is related to the ionization state due to the significantly higher ambient medium densities in the CC SNRs. Within each

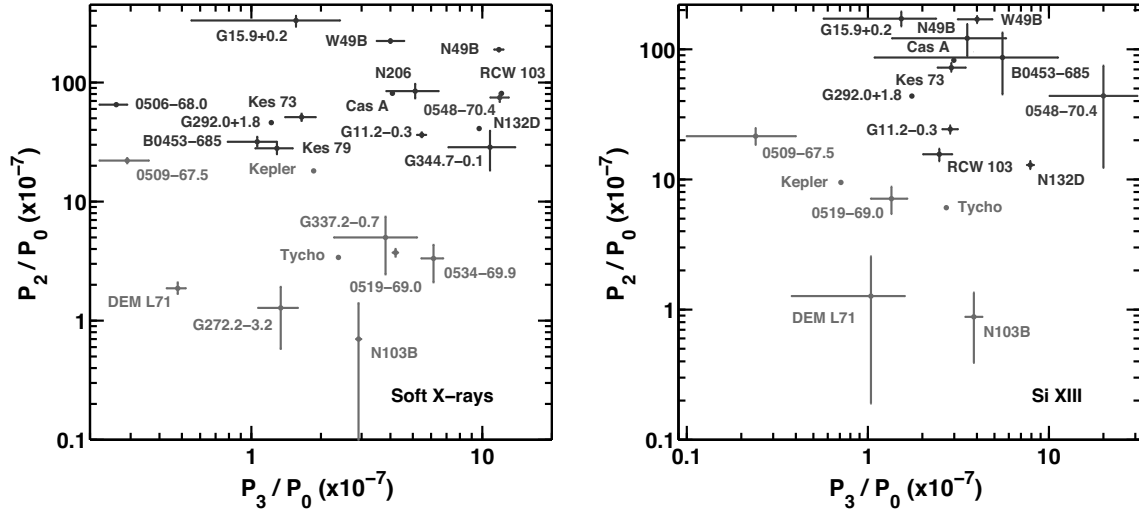


**Figure 4.5:** Results from a statistical analysis using line emission image with *Chandra*. Left: The correlation of the mirror symmetry ( $P_2/P_0$ ) and the circular symmetry ( $P_3/P_0$ ) of the 0.5–2.1 keV X-ray band for 24 SNRs in our Galaxy and the LMC. Right: The same plot, but using only Si XIII emission ( $\sim 1.75$ – $2.0$  keV) in the 17 SNRs dominated thermal emission. The red and blue marks are Type Ia SNR and CC SNRs, respectively. SNR 0548–70.4 is in purple because of its anomalous ejecta properties that make its type uncertain. All figures taken from Lopez *et al.* (2011).

progenitor group, the Fe  $K\alpha$  luminosity and centroid are well correlated, with more luminous objects having more highly ionized Fe. The correlation in Type Ia SNRs is explained by theoretical predictions based on SNR models obtained from Type Ia SN ejecta profiles evolving in a uniform ambient medium density.

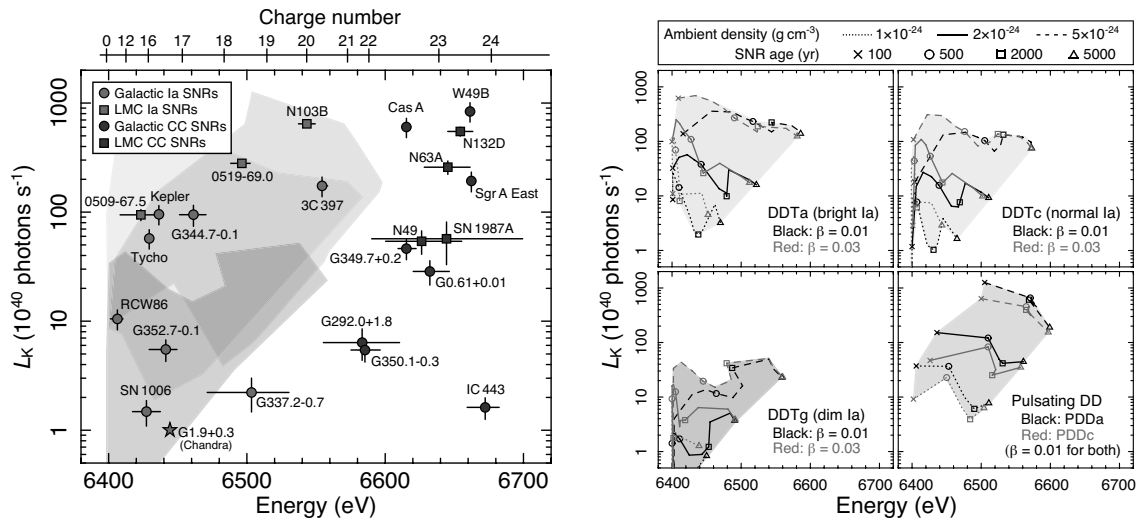


**Figure 4.6:** Diagnostic for progenitor type using Fe K $\alpha$  line with *Suzaku*. Left: Fe K $\alpha$  centroid energy as function of line luminosities of Fe K $\alpha$  from various SNRs in our Galaxy and the LMC. This plot corresponds to the effective charge state of Fe (Yamaguchi *et al.*, 2014b). The color regions indicate the theoretical predictions of Type Ia SNR evolution. Right: predicted Fe K $\alpha$  parameters for the various models of Type Ia SNRs evolving in a uniform ambient medium densities of  $1 \times 10^{-24}$  (dotted),  $2 \times 10^{-24}$  (solid), and  $5 \times 10^{-24}$   $g\ cm^{-3}$  (dashed). These shaded regions are plotted in this left figure (Yamaguchi *et al.*, 2014a).



## Chapter 5

# INSTRUMENTS

### 5.1 Overview of the *Suzaku* Satellite

*Suzaku* (Mitsuda *et al.*, 2007) is Japan's fifth X-ray astronomy satellite, the successor to the *ASCA* satellite (Tanaka *et al.*, 1994). It was launched from JAXA's<sup>1</sup> Uchinoura Space Center on July 10, 2005, and put into an approximately circular orbit at  $\sim 570$  km altitude with an inclination of  $31^\circ$ . The orbital period is about 90 min. Figure 5.1 shows schematic and side views of *Suzaku*. Its weight is 1.7 tons and its length is 6.5 m along the telescope axis after deployment of an extensible optical bench (EOB). *Suzaku* is composed of five collection mirrors (X-ray Telescopes, XRTs; Serlemitsos *et al.*, 2007) and three distinct types of soft and hard X-ray detector; the X-ray Imaging Spectrometer (XIS; Koyama *et al.*, 2007), the X-ray Spectrometer (XRS; Kelley *et al.*, 2007), and the Hard X-ray Detector (HXD; Takahashi *et al.*, 2007). Each XIS and XRS is placed in the focal plane of a dedicated XRT.

---

<sup>1</sup>Japan Aerospace Exploration Agency

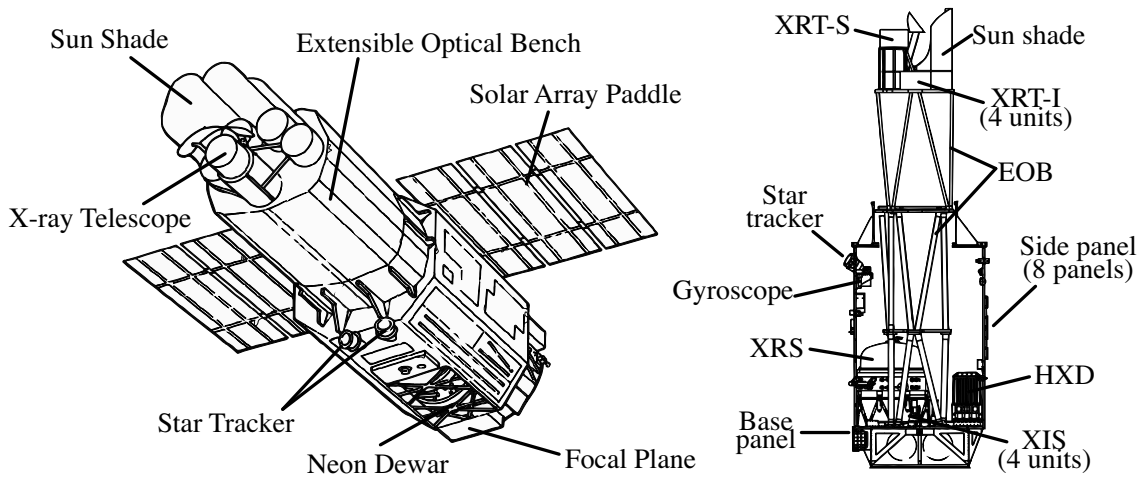


**Figure 5.1:** Schematic view (left) and side-view (right) of *Suzaku* (Mitsuda *et al.*, 2007).

**Table 5.1:** *Suzaku* performance (Mitsuda *et al.*, 2007).

XRT	Focal length	4.75 m
	Field of view	17' (@ 1.5 keV) / 13' (@ 8 keV)
	Effective area	440 cm <sup>2</sup> (@ 1.5 keV) / 250 cm <sup>2</sup> (@ 8 keV)
	Angular resolution	2' (half power diameter, HPD)
XIS	Field of view (FoV)	17'8×17'8
	Energy range	0.2–12 keV
	Pixel grid	1024×1024
	Pixel size	24 μm×24 μm
	Energy resolution	FWHM ~ 130 eV (@ 6 keV)
	Effective area	330 (FI) & 370 (BI) cm <sup>2</sup> (@ 1.5 keV)
	(including XRT)	160 (FI) & 110 (BI) cm <sup>2</sup> (@ 8 keV)
HXD	Field of view (FoV)	34'×34' (≲ 100 keV) / 4.°5×4.°5 (≳ 100 keV)
	Energy range	PIN: 10–70 keV / GSO: 40–600 keV

The XIS performs imaging and spectroscopy with high energy resolution for the 0.5–12 keV soft X-ray band. The XRS is an X-ray microcalorimeter, which performs X-ray

spectroscopy with the ultrahigh energy resolution of  $\sim 5$  eV. However, the XRS system became inoperable about a month after the launch (on August 8, 2005) due to a serious accident involving the loss of the liquid helium coolant, despite entering orbit. The HXD has high hard-X-ray sensitivity in the 10–600 keV energy band without imaging. The HXD sensor actually consists of two types: a GSO scintillator detector and PIN silicon diodes. The detector capabilities are summarized in table 5.1. Below we introduce the XRT and XIS in more detail.

## 5.2 X-ray Telescope (XRT)

There are five XRT (Serlemitsos *et al.*, 2007) modules in *Suzaku*, which were developed jointly by NASA/GSFC, Tokyo Metropolitan University, Nagoya University, and ISAS/JAXA. Figure 5.2 shows a photograph of the XRT without the thermal shield. A schematic view of the XRT mounted on the *Suzaku* EOB is shown in figure 5.3. The XRT is composed of Wolter I grazing-incidence reflection optics in which thin-foil conical mirror shells are nested tightly with a total of 175 quadrant mirrors with a 40 cm aperture. Incident X-rays are reflected twice by these mirror surfaces, which are arranged in a parabolic and hyperbolic pattern, and concentrated on the detector within  $< \sim 1^\circ$ . The focal lengths of the XRT are 4.75 m for the XIS (XRT-I) and 4.5 m for the XRS (XRT-S). These high performances are achieved within the limited mass of  $< 20$  kg per telescope.

The effective areas per unit are typically  $440 \text{ cm}^2$  at 1.5 keV and  $250 \text{ cm}^2$  at 8 keV. The field of view (FoV) for XRT-I is about  $17'$  at 1.5 keV. The angular resolution of the XRT is  $\sim 2'$  (half-power diameter, HPD). Figure 5.4 shows the dependence of the effective area on the X-ray incident angle, called the vignetting effect. The effect was calculated by a ray-tracing simulator and confirmed in the observation of the Crab nebula.

## 5.3 X-ray Imaging Spectrometer (XIS)

### 5.3.1 Overview

The XIS CCD systems were developed by Kyoto University, Osaka University, Massachusetts Institute of Technology, Rikkyo University, Ehime University, and ISAS<sup>2</sup>/JAXA. The XIS, as shown in figure 5.5, employs X-ray-sensitive silicon charge-coupled devices

---

<sup>2</sup>Institute of Space and Astronautical Science

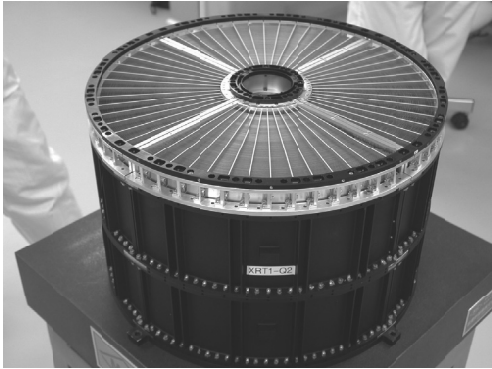


**Figure 5.2:** Photograph of the XRT without the thermal shield (Serlemitsos *et al.*, 2007).

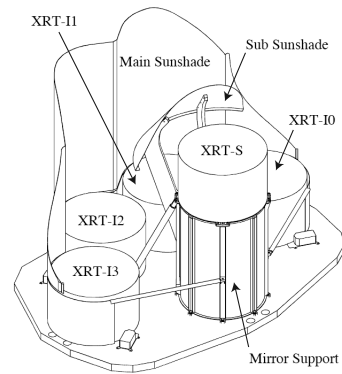


**Figure 5.3:** Schematic view of the XRT mounted on the *Suzaku* EOB (Serlemitsos *et al.*, 2007).

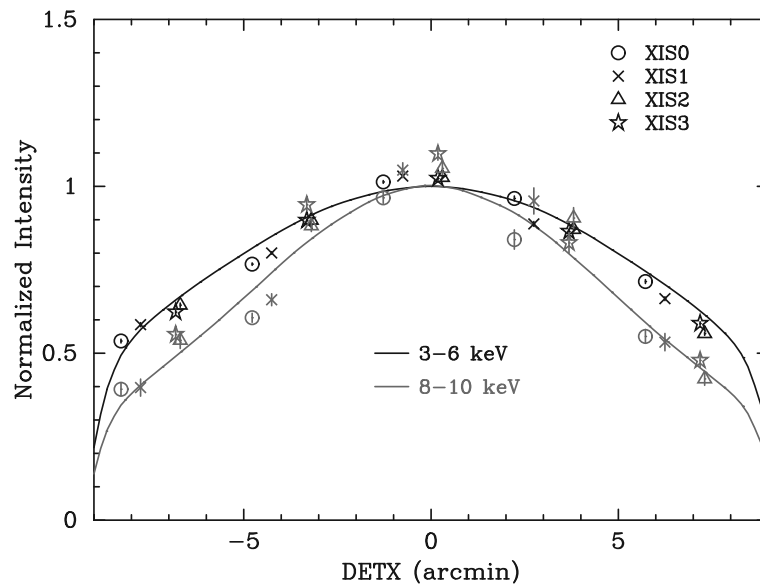


**Figure 5.4:** Vignetting of the four XRT-I modules using the measured data of the Crab nebula in the two energy bands. The model curves (solid line) are simulated with a spectral model of the Crab nebula (Serlemitsos *et al.*, 2007). Black and red are the result of 3–6 keV and 8–10 keV, respectively.

(CCDs) and sets of four sensors, with each sensor having one CCD chip. Three of the sensors (XIS0, XIS2, and XIS3) are front-illuminated (FI) CCDs and the other (XIS1) is a back-illuminated (BI) CCD. Each CCD is composed of four segments (A, B, C, and D) as shown in figure 5.6.

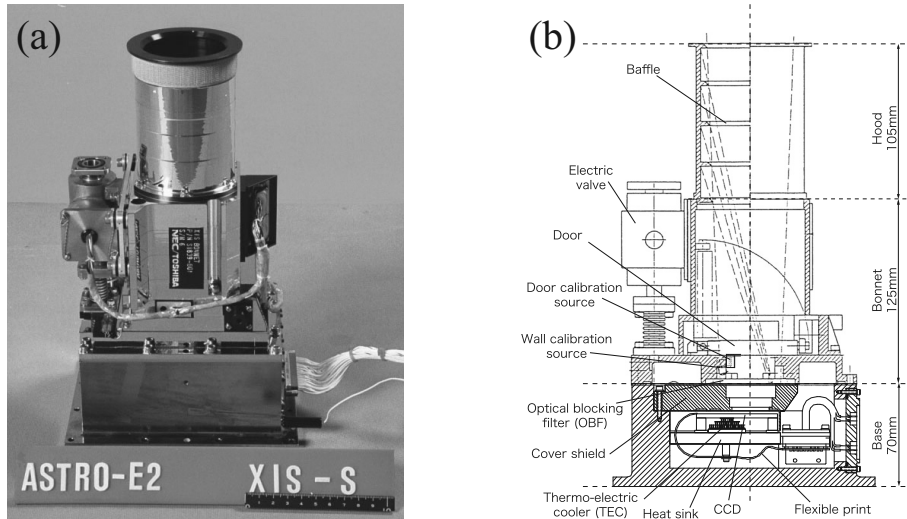


**Figure 5.5:** Photograph and side-view of the XIS CCD (Koyama *et al.*, 2007).

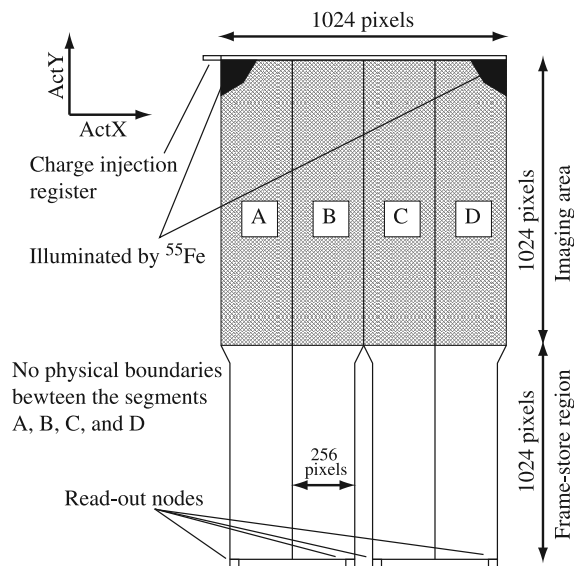


**Figure 5.6:** Top view of the XIS CCD (Koyama *et al.*, 2007).

Each CCD chip is composed of pixels of  $24 \times 24 \mu\text{m}^2$ , which are arranged in an array of  $1024 \times 1024$  pixels. The size of the CCD is therefore  $25 \times 25 \text{mm}^2$ . The depletion layer of the FI CCD ( $\sim 65 \mu\text{m}$ ) is thicker than that of the BI CCD ( $\sim 42 \mu\text{m}$ ). The quantum

efficiency at a high energy is higher for the FI CCD than for the BI CCD as shown in figure 5.7. The XIS can detect the energy and position of incident X-rays in the energy range of 0.2–12 keV, which are coupled with the XRT. The FoV is  $17'8 \times 17'8$ , and the effective area of the XIS including the XRT is shown in figure 5.8. The total effective area of the four XRTs including the detector efficiency is shown in figure 5.9 and is compared with that for other X-ray missions. The XRT is provided with imaging capability in the 0.2–12 keV energy band.

For on-orbit calibration, we used two  $^{55}\text{Fe}$  calibration sources emitting a fluorescent X-ray of a Mn K-shell line ( $K\alpha$ : 5.895 keV). These sources are attached on the bonnet wall of each sensor (figure 5.5 (b)). Each camera has an optical blocking filter (OBF) located above the imaging area to prevent the intrusion of optical and UV light into the sensor. The OBF is made of aluminum and a polyimide film that is opaque to visible light ( $\leq 5 \times 10^{-5}$ ) but transparent to X-rays ( $\geq 80\%$  above 0.7 keV). Thus, the former has a better energy response and a lower background level, while the latter has superior sensitivity in the soft X-ray band. XIS2 went out of operation on November 9, 2006, caused by the impact of a micrometeorite.

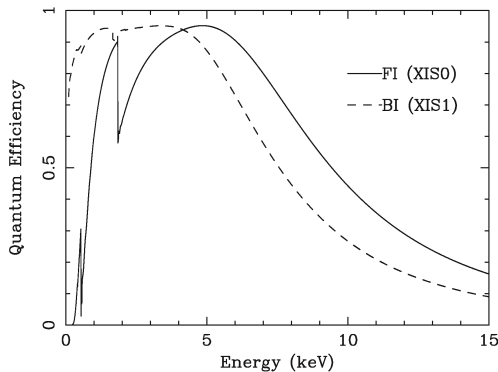


**Figure 5.7:** Quantum efficiency of the XIS as function of incident X-ray energy for FI and BI CCD (Koyama *et al.*, 2007).

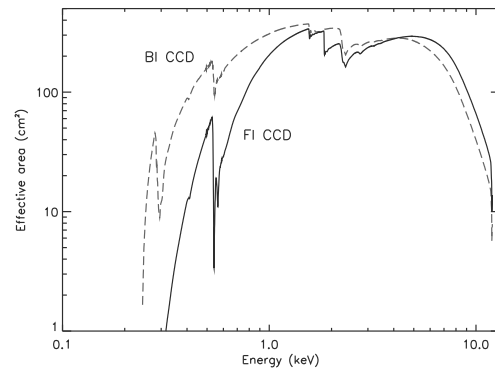


**Figure 5.8:** Effective area of the XIS including the XRT for FI and BI CCD, respectively (Mitsuda *et al.*, 2007).

### 5.3.2 Basic performance

Even if monochromatic X-rays enter the XIS, the observed spectrum has a complicated shape as shown in figure 5.10. This response to monochromatic X-rays is called the “response function” and is measured mainly on the basis of ground calibration. The response function used in the data analysis software XSPEC (Arnaud, 1996) is contained in the response matrix files (RMFs), which were created with the `xisrmfgen` software

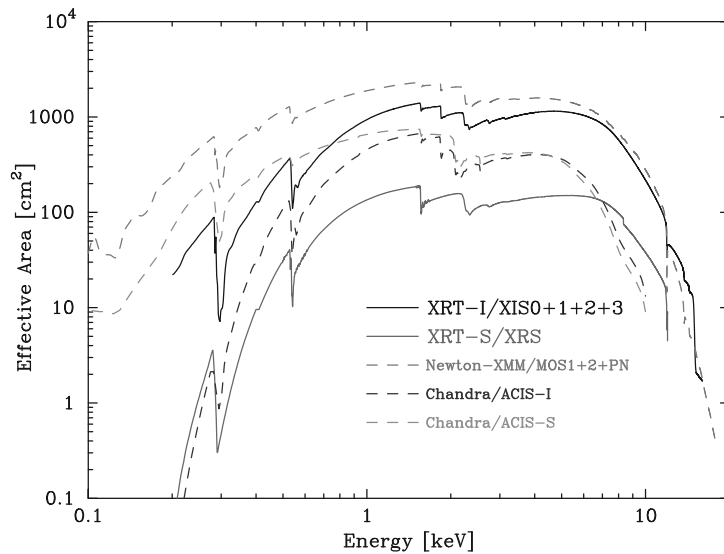


**Figure 5.9:** The total effective area of the XRT-I combined to the XIS compared with that of *Chandra* and *XMM-Newton* (Serlemitsos *et al.*, 2007).

(Ishisaki *et al.*, 2007).

Figure 5.11 shows the background rate of the XIS in the 0.5–10 keV band. Those for other X-ray missions, *ASCA*, *Chandra*, and *XMM-Newton*, which are normalized by the effective area and by the FoV, are plotted for comparison in figure 5.11. The XIS has the lowest background, which is the same as that for *ASCA* SIS, owing to a combination of the lower orbit of *Suzaku* and the instrument design. At the Fe K-line energy ( $\sim 6.4$ –7 keV), the XIS has the largest effective area with the lowest background, which makes it an essential tool for the investigation of high-energy sources.

### 5.3.3 Radiation damage

When part of a silicon crystal in a CCD chip is microscopically damaged by radiation, some of the charge is trapped there. This generally causes an increase in the dark current. Therefore, the performance of the *Suzaku* XIS CCDs (energy gain and resolution) has been gradually degrading since the launch as shown in figure 5.12. The damage increases the charge transfer inefficiency (CTI). To reduce this effect, XIS team members utilize a calibration source and charge injection. They monitor the time variability of the instrument gain using  $^{55}\text{Fe}$  sources. Each XIS CCD is equipped with charge injection capability, which is useful for measuring and even suppressing the CTI. These results have been used for calibration of the data observed by *Suzaku*.

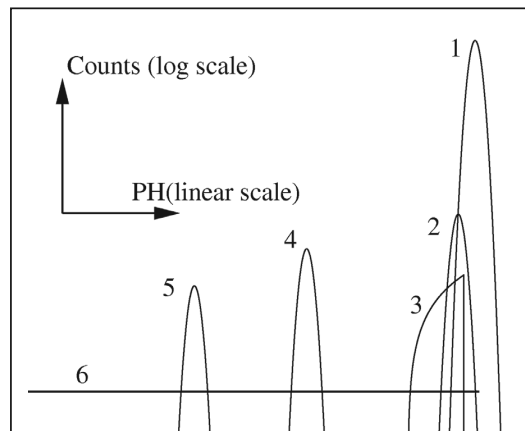


**Figure 5.10:** The XIS response function to incident monochromatic X-ray. There are (1) main peak, (2) sub peak, (3) triangle component, (4) silicon escape peak, (5) silicon fluorescent peak, and (6) constant tail component (Koyama *et al.*, 2007).

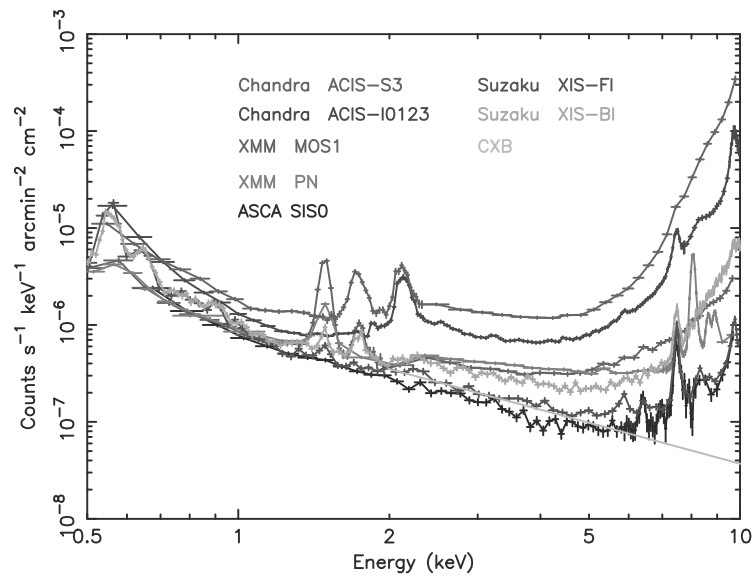


**Figure 5.11:** Background count rate of XIS as a function of energy compared with that of *ASCA*, *Chandra*, and *XMM-Newton*. The background rate was normalized to the same effective area and the field of view (Mitsuda *et al.*, 2007).

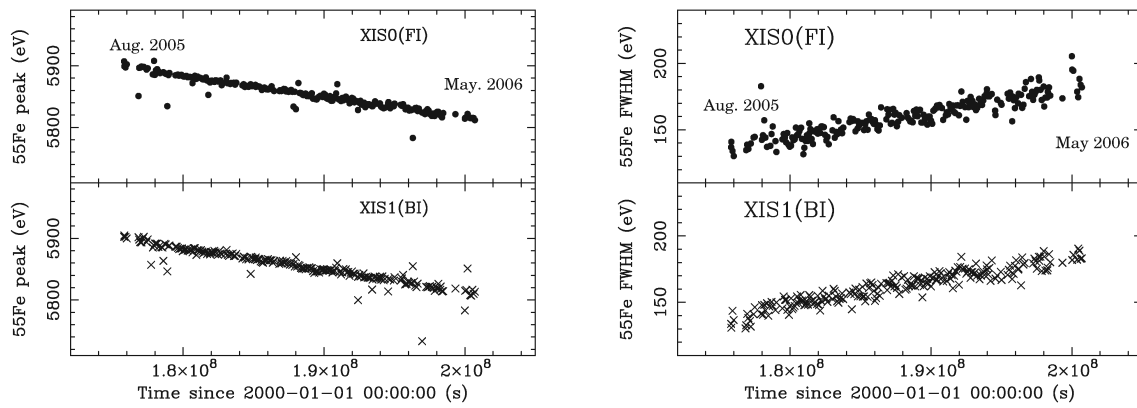


**Figure 5.12:** Left: The time history of the peak for center energy of Mn  $K\alpha$  line from the  $^{55}\text{Fe}$  calibration sources for XIS0 (FI CCD: upper) and for XIS1 (BI CCD: lower). Right: Same as the left figure but for the energy resolution (Koyama *et al.*, 2007).



## Chapter 6

# OBSERVATIONS

### 6.1 Target Selection

We should select suitable targets for systematic analysis to diagnose plasma states and metal abundances using emission lines from the ‘spatially integrated’ spectra with the *Suzaku* XIS as explained in § 5.3. A systematic X-ray study of Galactic SNRs is not easy due to the large ISM absorption and the ambiguity of the source distance. Thus, we focus on the SNRs in both Magellanic Clouds (MCs), the Large Magellanic Cloud (LMC) and the Small Magellanic Cloud (SMC). The MCs are one of the nearest satellite galaxies of our Milky Way. Figure 6.1 shows visible images of the LMC and SMC taken by the Anglo-Australian Observatory. The LMC has dimensions of  $\sim 10.8 \times 9.2$ , whereas the SMC has dimensions of  $\sim 4.7 \times 2.7$ . The disk of the LMC is tilted toward us such that it appears that we are looking at it from above. The LMC and SMC are particularly suitable for this systematic study owing to their low foreground extinction (Dickey & Lockman, 1990) because of their high Galactic latitude (LMC:  $-32^\circ$ , SMC:  $-44^\circ$ , Westerlund, 1990). Figure 6.2 shows the locations of the MCs relative to our Galaxy. The absorption volume toward the MCs is approximately two orders of magnitude lower than that toward the Galactic center. Another merit of the SNRs in the MCs is that the distances to the SNRs are regarded as the same as those to the LMC and SMC because the MCs have been regarded as a thin flat disk (thickness:  $\sim 1.5$  kpc, Westerlund, 1990) seen nearly face-on. The distances to the LMC and SMC have been measured to be 50 kpc and 60 kpc using Cepheid variable stars, respectively (Westerlund, 1990). 77 SNRs are known to exist in the MCs by multiwavelength observations from radio to X-ray, which have been catalogued by Badenes *et al.* (2010). Although the angular resolution of *Suzaku* does not allow us to

spatially resolve the SN ejecta in the MCs from the swept-up ISM, its excellent energy resolution has enabled the clear separation of emission lines in the soft X-ray band. We choose 20 SNRs observed by *Suzaku*. Table 6.1 gives a list of the MCs SNRs observed by *Suzaku*.

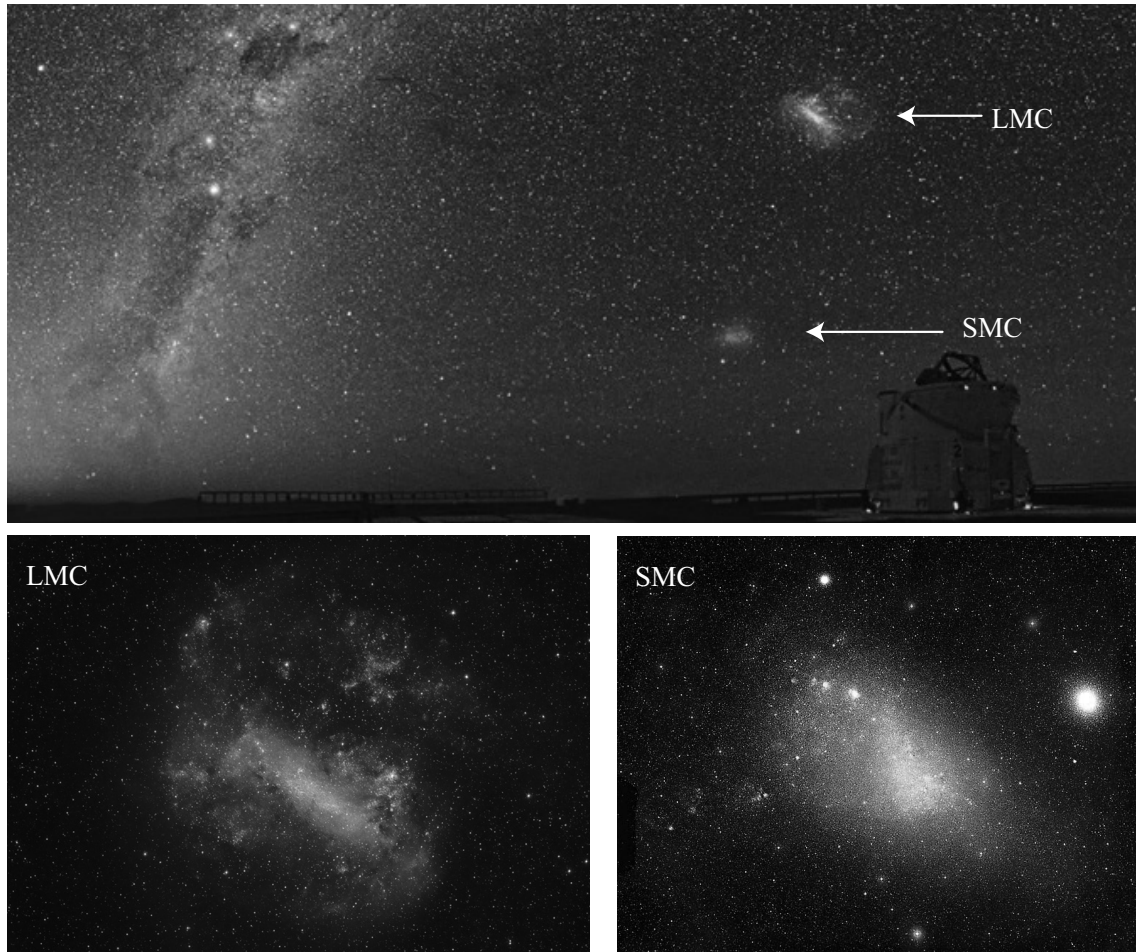


**Figure 6.1:** Optical images of the LMC and SMC. All images taken by Anglo-Australian Observatory.

**Table 6.1:** List of the MCs SNRs observed by *Suzaku*.

Name	Obs ID	Exposure (ks)	Observation Date	Position R.A. Decl.	Radius (arcsec / pc)	Age (yr)	Ref.*
LMC SNRs:							
0509-67.5	5080720[1-2]0	328	2013 Apr 11, July 18	05 <sup>h</sup> 09 <sup>m</sup> 33 <sup>s</sup> -67 <sup>d</sup> 30 <sup>m</sup> 40 <sup>s</sup>	15/3.6	400 ± 120	1, 2
0519-69.0	806026010	348	2011 Aug. 9	05 <sup>h</sup> 19 <sup>m</sup> 37 <sup>s</sup> -69 <sup>d</sup> 02 <sup>m</sup> 19 <sup>s</sup>	17/4.0	600 ± 200	3, 4
N103B	804039010	223	2009 Dec. 29	05 <sup>h</sup> 08 <sup>m</sup> 55 <sup>s</sup> -68 <sup>d</sup> 43 <sup>m</sup> 18 <sup>s</sup>	30/7.3	860	3, 6
N132D	11 Obs**	254		05 <sup>h</sup> 24 <sup>m</sup> 58 <sup>s</sup> -69 <sup>d</sup> 39 <sup>m</sup> 33 <sup>s</sup>	50/12.1	~3,000	3, 7
N63A	508071010	82	2013 Dec. 2	05 <sup>h</sup> 35 <sup>m</sup> 43 <sup>s</sup> -66 <sup>d</sup> 02 <sup>m</sup> 20 <sup>s</sup>	34/8.2	2,000-5,000	3, 8
N23	807008010	102	2008 May 15	05 <sup>h</sup> 05 <sup>m</sup> 46 <sup>s</sup> -67 <sup>d</sup> 52 <sup>m</sup> 15 <sup>s</sup>	28/6.7	3,800	5
N49	807007010	185	2012 May 9	05 <sup>h</sup> 26 <sup>m</sup> 02 <sup>s</sup> -66 <sup>d</sup> 04 <sup>m</sup> 36 <sup>s</sup>	34/8.2	~4,400	3, 9
DEM L71	807008010	102	2012 Apr 4	05 <sup>h</sup> 05 <sup>m</sup> 46 <sup>s</sup> -67 <sup>d</sup> 52 <sup>m</sup> 13 <sup>s</sup>	43/10.4	4,700	5
N49B	807007010	185	2012 May 9	05 <sup>h</sup> 25 <sup>m</sup> 29 <sup>s</sup> -65 <sup>d</sup> 59 <sup>m</sup> 05 <sup>s</sup>	70/17	3,000-10,000	3
SN 1987A	801090010	40	2006 June 8	05 <sup>h</sup> 35 <sup>m</sup> 26 <sup>s</sup> -69 <sup>d</sup> 15 <sup>m</sup> 30 <sup>s</sup>	0.8/0.2	28	9
DEM L238†	505063010	200	2010 Apr 22	05 <sup>h</sup> 34 <sup>m</sup> 24 <sup>s</sup> -70 <sup>d</sup> 33 <sup>m</sup> 12 <sup>s</sup>	80/20	13,500	12
DEM L249†	505063010	200	2010 Apr 22	05 <sup>h</sup> 36 <sup>m</sup> 13 <sup>s</sup> -70 <sup>d</sup> 38 <sup>m</sup> 10 <sup>s</sup>	~80/ ~20,000	10,000-15,000	12
0534-69.9	505064010	109	2010 Mar 31	05 <sup>h</sup> 34 <sup>m</sup> 01 <sup>s</sup> -69 <sup>d</sup> 54 <sup>m</sup> 22 <sup>s</sup>	57 / 13.7	10,100	13
0548-70.4	505065010	104	2010 July 1	05 <sup>h</sup> 74 <sup>m</sup> 52 <sup>s</sup> -70 <sup>d</sup> 25 <sup>m</sup> 01 <sup>s</sup>	51 / 12.1	7,100	13
B0532-71.0	803038010	49	2008 Apr 28	05 <sup>h</sup> 31 <sup>m</sup> 59 <sup>s</sup> -71 <sup>d</sup> 00 <sup>m</sup> 03 <sup>s</sup>	87/21	23,000-27,000	14
B0532-67.5‡	806007010	82	2011 Nov 6	05 <sup>h</sup> 32 <sup>m</sup> 23 <sup>s</sup> -67 <sup>d</sup> 31 <sup>m</sup> 16 <sup>s</sup>	48/11.6	—	15
SMC SNRs:							
E0102.2-7219	26 Obs††	629		01 <sup>h</sup> 04 <sup>m</sup> 04 <sup>s</sup> -72 <sup>d</sup> 01 <sup>m</sup> 43 <sup>s</sup>	20/5.9	~1,000	10
0103-72.6	501077010	49	2006 Apr 23	01 <sup>h</sup> 05 <sup>m</sup> 07 <sup>s</sup> -72 <sup>d</sup> 23 <sup>m</sup> 19 <sup>s</sup>	85 / 24.7	18,000	16
0049-73.6	503094010	120	2008 June 12	00 <sup>h</sup> 51 <sup>m</sup> 09 <sup>s</sup> -73 <sup>d</sup> 21 <sup>m</sup> 54 <sup>s</sup>	72 / 20.5	14,000	17
0104-72.3	803002010	107	2008 May 15	01 <sup>h</sup> 06 <sup>m</sup> 19 <sup>s</sup> -72 <sup>d</sup> 05 <sup>m</sup> 41 <sup>s</sup>	55 / 16	17,600	18

\* Representative references — (1) Rest *et al.* (2005); (2) Warren & Hughes (2004); (3) Rest *et al.* (2005); (4) Kosenko *et al.* (2010); (5) Hughes *et al.* (1998); (6) Lewis *et al.* (2003); (7) Borkowski *et al.* (2007); (8) Warren *et al.* (2003); (9) Park *et al.* (2012); (10) Maggi *et al.* (2012); (11) Westerlund (1990); (12) Borkowski *et al.* (2006); (13) Hendrick *et al.* (2003); (14) Williams *et al.* (2005); (15) Badenes *et al.* (2010); (16) Park *et al.* (2003a); (17) Hendrick *et al.* (2005); (18) Lopez *et al.* (2014)

† These two SNRs were observed in the same FoV.

‡ The age of B0532-67.5 is previously unreported.

\*\* Obs. ID: 100002010, 100002060, 105011010, 1060100[1-2]0, 1070080[1-2]0, 1080080[2-5]0, 1090090[1-2]0

†† Obs. ID: 1010050[1-7,9]0, 1010051[0-2]0, 10200[1-6]010, 102021010, 1030010[1-6]0

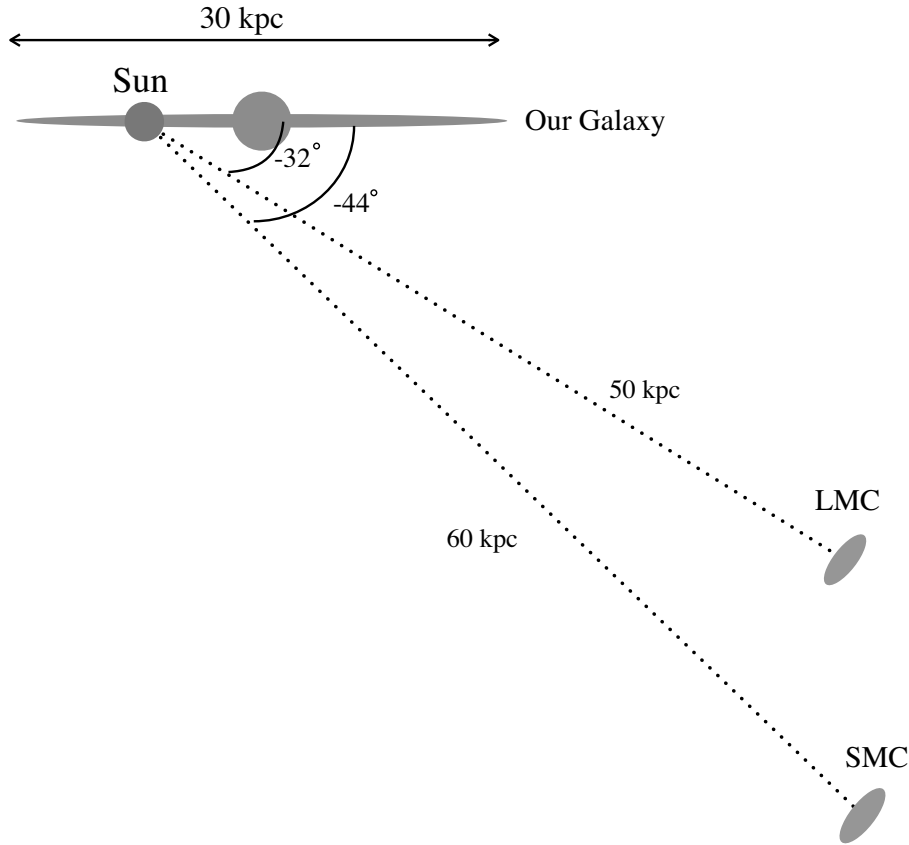


**Figure 6.2:** Locations of the LMC and SMC relative to our Galaxy.

## 6.2 Observation and Data Reduction

For data reduction, we used the HEASoft version 16.6 software package. We utilized the data with the  $5 \times 5$  and  $3 \times 3$  editing modes. We reprocessed the data using the `aepipeline` task with the latest calibration data released in May 2015. To exclude high-background events, we removed time intervals corresponding to the South Atlantic Anomaly and the elevation angles from the night and day of Earth of less than  $5^\circ$  and  $20^\circ$ , respectively. We also utilized only events with grades of 0, 2, 3, 4, and 6 in the following spectral analysis. Screening with an appropriate time interval, which was to obtain data for analysis from raw data, was performed in accordance with the standard criteria to obtain the effective exposures given in table 6.1. For each SNR, we extracted XIS spectra from a circular region centered at the source with a radius of  $\sim 180''$ . The background spectrum was extracted from an annular region surrounding the source with inner and outer diameters of  $\sim 180''$  and  $\sim 400''$ , respectively. The parameters of the regions used for the source

**Table 6.2:** Select region for spectral analysis.

Name	source region			background region		
	Position (J2000)		radius (")	Position (J2000)		outer/inner (")
	R.A.	Decl.		R.A.	Decl.	
LMC SNRs:						
0509–67.5	05 <sup>h</sup> 09 <sup>m</sup> 33 <sup>s</sup>	–67 <sup>d</sup> 30 <sup>m</sup> 40 <sup>s</sup>	180	05 <sup>h</sup> 09 <sup>m</sup> 43 <sup>s</sup>	–67 <sup>d</sup> 32 <sup>m</sup> 41 <sup>s</sup>	422/180
0519–69.0	05 <sup>h</sup> 19 <sup>m</sup> 37 <sup>s</sup>	–69 <sup>d</sup> 02 <sup>m</sup> 19 <sup>s</sup>	180	05 <sup>h</sup> 19 <sup>m</sup> 44 <sup>s</sup>	–69 <sup>d</sup> 02 <sup>m</sup> 15 <sup>s</sup>	903×1039*/180
0534–69.9	05 <sup>h</sup> 34 <sup>m</sup> 01 <sup>s</sup>	–69 <sup>d</sup> 54 <sup>m</sup> 22 <sup>s</sup>	180	05 <sup>h</sup> 34 <sup>m</sup> 01 <sup>s</sup>	–69 <sup>d</sup> 54 <sup>m</sup> 22 <sup>s</sup>	453/180
0548–70.4	05 <sup>h</sup> 74 <sup>m</sup> 52 <sup>s</sup>	–70 <sup>d</sup> 25 <sup>m</sup> 01 <sup>s</sup>	180	05 <sup>h</sup> 74 <sup>m</sup> 52 <sup>s</sup>	–70 <sup>d</sup> 25 <sup>m</sup> 01 <sup>s</sup>	432/180
N23	05 <sup>h</sup> 05 <sup>m</sup> 46 <sup>s</sup>	–67 <sup>d</sup> 52 <sup>m</sup> 15 <sup>s</sup>	180	05 <sup>h</sup> 05 <sup>m</sup> 48 <sup>s</sup>	–67 <sup>d</sup> 56 <sup>m</sup> 38 <sup>s</sup>	482/180
N49	05 <sup>h</sup> 26 <sup>m</sup> 02 <sup>s</sup>	–66 <sup>d</sup> 04 <sup>m</sup> 36 <sup>s</sup>	210	05 <sup>h</sup> 25 <sup>m</sup> 58 <sup>s</sup>	–66 <sup>d</sup> 05 <sup>m</sup> 09 <sup>s</sup>	425/210
N49B	05 <sup>h</sup> 25 <sup>m</sup> 29 <sup>s</sup>	–65 <sup>d</sup> 59 <sup>m</sup> 05 <sup>s</sup>	253×347*	05 <sup>h</sup> 26 <sup>m</sup> 06 <sup>s</sup>	–66 <sup>d</sup> 04 <sup>m</sup> 21 <sup>s</sup>	475/319×479*+231
N63A	05 <sup>h</sup> 35 <sup>m</sup> 43 <sup>s</sup>	–66 <sup>d</sup> 02 <sup>m</sup> 20 <sup>s</sup>	180	05 <sup>h</sup> 35 <sup>m</sup> 38 <sup>s</sup>	–66 <sup>d</sup> 02 <sup>m</sup> 24 <sup>s</sup>	390/180
N103B	05 <sup>h</sup> 08 <sup>m</sup> 55 <sup>s</sup>	–68 <sup>d</sup> 43 <sup>m</sup> 18 <sup>s</sup>	180	05 <sup>h</sup> 08 <sup>m</sup> 35 <sup>s</sup>	–68 <sup>d</sup> 44 <sup>m</sup> 44 <sup>s</sup>	390/180
N132D	05 <sup>h</sup> 24 <sup>m</sup> 58 <sup>s</sup>	–69 <sup>d</sup> 39 <sup>m</sup> 33 <sup>s</sup>	180	05 <sup>h</sup> 25 <sup>m</sup> 06 <sup>s</sup>	–69 <sup>d</sup> 38 <sup>m</sup> 43 <sup>s</sup>	1020×1020*/270
DEM L71	05 <sup>h</sup> 05 <sup>m</sup> 46 <sup>s</sup>	–67 <sup>d</sup> 52 <sup>m</sup> 13 <sup>s</sup>	180	05 <sup>h</sup> 05 <sup>m</sup> 48 <sup>s</sup>	–67 <sup>d</sup> 56 <sup>m</sup> 37 <sup>s</sup>	482/180
DEM L238	05 <sup>h</sup> 34 <sup>m</sup> 20 <sup>s</sup>	–70 <sup>d</sup> 32 <sup>m</sup> 59 <sup>s</sup>	210	05 <sup>h</sup> 35 <sup>m</sup> 16 <sup>s</sup>	–70 <sup>d</sup> 34 <sup>m</sup> 34 <sup>s</sup>	440/240
DEM L249	05 <sup>h</sup> 36 <sup>m</sup> 13 <sup>s</sup>	–70 <sup>d</sup> 38 <sup>m</sup> 10 <sup>s</sup>	120	05 <sup>h</sup> 35 <sup>m</sup> 16 <sup>s</sup>	–70 <sup>d</sup> 34 <sup>m</sup> 34 <sup>s</sup>	440/285×380*
SN 1987A	05 <sup>h</sup> 35 <sup>m</sup> 25 <sup>s</sup>	–69 <sup>d</sup> 15 <sup>m</sup> 47 <sup>s</sup>	180	05 <sup>h</sup> 35 <sup>m</sup> 25 <sup>s</sup>	–69 <sup>d</sup> 15 <sup>m</sup> 47 <sup>s</sup>	480/180
B0532–71.0	05 <sup>h</sup> 31 <sup>m</sup> 59 <sup>s</sup>	–71 <sup>d</sup> 00 <sup>m</sup> 03 <sup>s</sup>	180	05 <sup>h</sup> 31 <sup>m</sup> 59 <sup>s</sup>	–71 <sup>d</sup> 00 <sup>m</sup> 03 <sup>s</sup>	526/180+274
B0532–67.5	05 <sup>h</sup> 32 <sup>m</sup> 23 <sup>s</sup>	–67 <sup>d</sup> 31 <sup>m</sup> 16 <sup>s</sup>	150	05 <sup>h</sup> 32 <sup>m</sup> 23 <sup>s</sup>	–67 <sup>d</sup> 31 <sup>m</sup> 16 <sup>s</sup>	360/150
SMC SNRs:						
E0102.2–7219	01 <sup>h</sup> 04 <sup>m</sup> 04 <sup>s</sup>	–72 <sup>d</sup> 02 <sup>m</sup> 11 <sup>s</sup>	240	01 <sup>h</sup> 04 <sup>m</sup> 02 <sup>s</sup>	–72 <sup>d</sup> 01 <sup>m</sup> 52 <sup>s</sup>	480/240
0103–72.6	01 <sup>h</sup> 05 <sup>m</sup> 03 <sup>s</sup>	–72 <sup>d</sup> 23 <sup>m</sup> 19 <sup>s</sup>	180	01 <sup>h</sup> 05 <sup>m</sup> 03 <sup>s</sup>	–72 <sup>d</sup> 23 <sup>m</sup> 19 <sup>s</sup>	420/180
0049–73.6	00 <sup>h</sup> 51 <sup>m</sup> 09 <sup>s</sup>	–73 <sup>d</sup> 21 <sup>m</sup> 54 <sup>s</sup>	180	00 <sup>h</sup> 51 <sup>m</sup> 10 <sup>s</sup>	–73 <sup>d</sup> 21 <sup>m</sup> 42 <sup>s</sup>	480/180+150×3cycle
0104–72.3	01 <sup>h</sup> 06 <sup>m</sup> 17 <sup>s</sup>	–72 <sup>d</sup> 05 <sup>m</sup> 34 <sup>s</sup>	270	01 <sup>h</sup> 06 <sup>m</sup> 14 <sup>s</sup>	–72 <sup>d</sup> 08 <sup>m</sup> 42 <sup>s</sup>	470/270+247

\*: The shape of the region is a box.

and background are listed in table 6.2. Figure 6.3 shows *Suzaku* XIS images of SNR 0534–69.9 for each detector with the source and background regions. We used several different background regions and confirmed that there was no significant change in the measured spectral parameters. We created XIS redistribution matrix files (RMFs) and ancillary response files (ARFs) using the `xismfgen` and `xissimarfgen` tasks (Ishisaki *et al.*, 2007). The following spectral analysis was performed with the XSPEC software version 12.8.2 (Arnaud, 1996).

### 6.3 Classification of SNRs

We categorize SNRs into two groups by their age, which is related to their evolution stage. The borderline is set at  $\sim 10^4$  yr, which is sufficient time for the reverse shock to reach the SNR center and for all ejecta to be heated. The SNR age we use was obtained

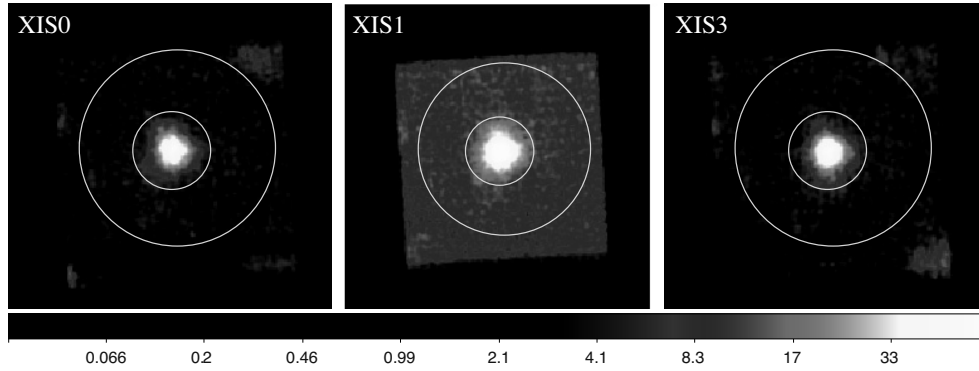


**Figure 6.3:** Each XIS image of SNR 0534-69.9 in the LMC (full energy bound). The color bar shows the count rate. The slightly higher counts at the corner in the whole images are from the calibration source,  $^{55}\text{Fe}$ . The size of SNR is a radius of  $\sim 57''$ , which is regarded as a point source with the *Suzaku* HPD.

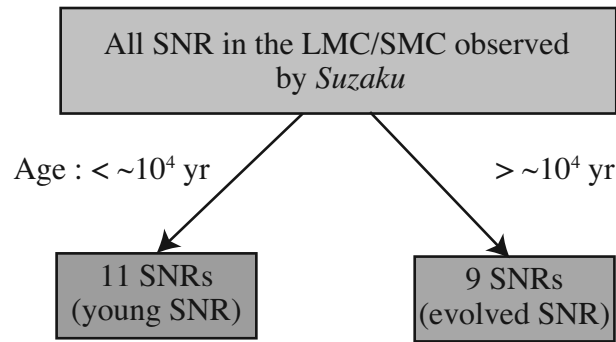


**Figure 6.4:** Classification scheme for our targets based on the SNR age.

in previous works as shown in table 6.1. Figure 6.4 shows the classification scheme for our targets. We define eleven SNRs, all of which are “young”, whereas the other SNRs are “evolved SNRs” in this thesis. Table 6.3 lists the SNRs grouped by our criterion. The spectra of all the SNRs are analyzed, but we do not discuss those of the young SNRs; because the plasma state in these SNRs is too complex, we cannot systematically study the young SNRs. For the young SNRs, the spectral features and the results of analysis are summarized in the appendix.

**Table 6.3:** List of SNR we analyzed.

All SNRs in the LMC/SMC (20 SNRs)	
young SNR (under $10^4$ yr)	Evolved SNR (over $10^4$ yr)
0509–67.5	DEM L238
0519–69.0	DEM L249
N103B	0534–69.9
N132D	0548–70.4
N63A	B0532–71.0
N49	B0532–67.5
N49B	0103–72.6
N23	0049–73.6
DEM L71	0104–72.3
SN 1987A	
E0102.2–7219	



## Chapter 7

# ANALYSIS AND RESULTS

### 7.1 Spectral Features

In this section, we analyze old SNRs defined as “evolved SNRs” in § 6.3. These SNRs can also be categorized into two groups by their spectral features. Figure 7.1 shows the typical wide-band spectra of SNR 0049–73.6 and DEM L249. We find that the spectral features around 1 keV are considerably different among the SNRs. The K-shell emission of O, Ne, and Mg is clearly resolved in 0049–73.6, which is a feature of CC SNRs (see § 2.1.2). In contrast, the broad Fe L-shell emission is enhanced in DEM L249, which is a feature of Type Ia SNRs (see § 2.1.1). The difference between the spectra is quantitatively estimated by a uniform analysis procedure. We focus on the 0.5–3.0 keV data in the following spectral analysis since none of the SNRs show a significant signal above  $\sim 3$  keV. Here we perform unbiased spectral modeling, although the previous *Chandra* observations revealed a degree of chemical inhomogeneity in some SNRs.

### 7.2 Model Fitting

#### 7.2.1 One-temperature NEI model

We first fit the spectra with a single-component variable-abundance non-equilibrium ionization (NEI) plasma model based on *AtomDB*<sup>1</sup> version 3.0.2 using the *vnei* model in XSPEC. The free parameters are  $kT_e$ ,  $n_e t$ , the normalization, and the abundances of O, Ne, Mg, Si, S, and Fe, where  $kT_e$  and  $n_e t$  are the electron temperature and the ionization parameter ( $n_e$  and  $t$  are the electron density and the elapsed time since the gas was

---

<sup>1</sup><http://www.atomdb.org/index.php>

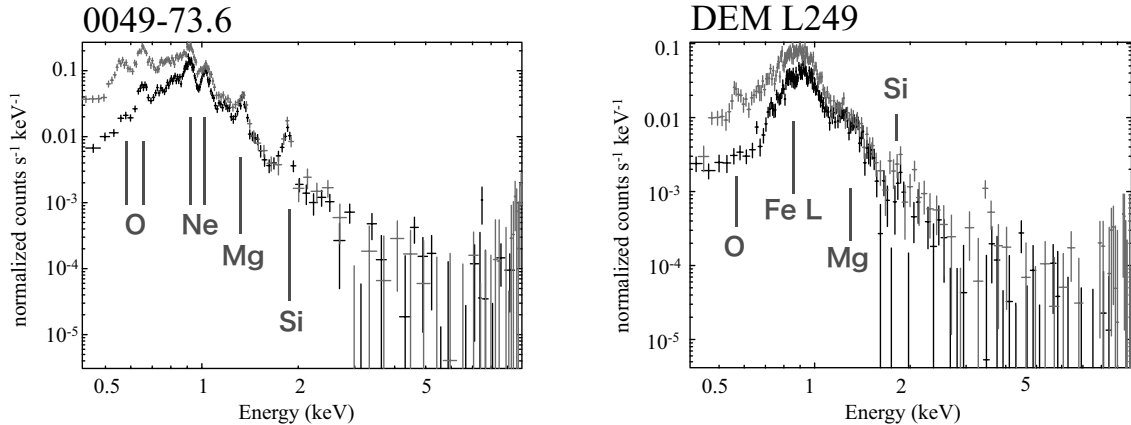


**Figure 7.1:** Background-subtracted XIS spectra. The black and red points are FI and BI CCDs, respectively. The main emission lines are labeled.

heated by shock), respectively. The normalization is represented by  $10^{-14}/4\pi D^2 \int n_e n_H dV$  ( $\text{cm}^{-5}$ ), where  $D$ ,  $n_H$ , and  $dV$  are the distance to the source from Earth, the hydrogen density, and the volume element of the plasma, respectively. The emission measure (EM) is defined by  $n_e n_H V$  ( $\text{cm}^{-3}$ ). For several SNRs, however, we fixed the O, Si, and/or S abundances to the mean LMC/SMC ISM values of Russell & Dopita (1992) or Lewis *et al.* (2003), respectively listed in tables 7.1 and 7.2, because otherwise the fit did not converge. The abundances of the other elements were fixed to the mean LMC/SMC values, except for Ni, whose abundance was tied to that of Fe. The interstellar extinction was separately considered in the Galaxy and the MCs. The Galactic absorption column density with the solar abundances was fixed at  $N_H^{\text{Gal.}} = 6 \times 10^{20} \text{ cm}^{-2}$  on the basis of the Galactic HI observations of Dickey & Lockman (1990). The other component ( $N_H^{\text{MC}}$ ) was a free parameter, with the assumption of the LMC/SMC metal abundances (using the *vphabs* model in XSPEC). Figure 7.2 and table 7.3 show the spectra fitted by a one-temperature ( $1-kT_e$ ) NEI model and the spectral parameters, respectively. This model and the assumptions yielded reasonable fits with  $\chi_\nu^2 \sim 1.2\text{--}2.0$ .

**Table 7.1:** Mean LMC ISM abundances.

Element	$12+\log N(\text{X}/\text{H})_{\text{LMC}}^*$	$(\text{X}/\text{H})_{\text{LMC}}$	$(\text{X}/\text{H})_{\odot}^{\dagger}$	$X_{\text{LMC}}/X_{\odot}$
He	10.94	$8.71 \times 10^{-2}$	$9.77 \times 10^{-2}$	0.891
C	8.04	$1.10 \times 10^{-4}$	$3.63 \times 10^{-4}$	0.302
N	7.14	$1.38 \times 10^{-5}$	$1.12 \times 10^{-4}$	0.123
O	8.35	$2.24 \times 10^{-4}$	$8.51 \times 10^{-4}$	0.263
Ne	7.61	$4.07 \times 10^{-5}$	$1.23 \times 10^{-4}$	0.331
Na	5.83	$6.76 \times 10^{-7}$	$2.14 \times 10^{-6}$	0.316
Mg	7.08	$1.20 \times 10^{-5}$	$3.80 \times 10^{-5}$	0.316
Al	5.98	$9.55 \times 10^{-7}$	$2.95 \times 10^{-6}$	0.324
Si	7.04	$1.10 \times 10^{-5}$	$3.55 \times 10^{-5}$	0.309
S	6.70	$5.01 \times 10^{-6}$	$1.62 \times 10^{-5}$	0.309
Cl	4.76	$5.75 \times 10^{-8}$	$3.16 \times 10^{-7}$	0.182
Ar	6.29	$1.95 \times 10^{-6}$	$3.63 \times 10^{-6}$	0.537
Ca	5.89	$7.76 \times 10^{-7}$	$2.29 \times 10^{-6}$	0.339
Cr	5.47	$2.95 \times 10^{-7}$	$4.68 \times 10^{-7}$	0.631
Fe	7.01	$1.02 \times 10^{-5}$	$4.68 \times 10^{-5}$	0.219
Co	4.41	$2.57 \times 10^{-8}$	$8.32 \times 10^{-8}$	0.309
Ni	6.04	$1.10 \times 10^{-6}$	$1.78 \times 10^{-6}$	0.616

\* The reference is Lewis *et al.* (2003).† The solar abundance table is from the *anqr* model (Anders & Grevesse, 1989).

**Table 7.2:** Mean SMC ISM abundances.

Element	$12+\log N(X/H)_{\text{SMC}}^*$	$(X/H)_{\text{SMC}}$	$(X/H)_{\odot}^{\dagger}$	$X_{\text{SMC}}/X_{\odot}$
He	10.91	$8.13 \times 10^{-2}$	$9.77 \times 10^{-2}$	0.832
C	7.73	$5.37 \times 10^{-5}$	$3.63 \times 10^{-4}$	0.148
N	6.63	$4.27 \times 10^{-6}$	$1.12 \times 10^{-4}$	0.038
O	8.03	$1.07 \times 10^{-4}$	$8.51 \times 10^{-4}$	0.126
Ne	7.27	$1.86 \times 10^{-5}$	$1.23 \times 10^{-4}$	0.151
Na	5.96	$9.12 \times 10^{-7}$	$2.14 \times 10^{-6}$	0.426
Mg	6.98	$9.55 \times 10^{-6}$	$3.80 \times 10^{-5}$	0.251
Al	6.40	$2.51 \times 10^{-6}$	$2.95 \times 10^{-6}$	0.851
Si	7.03	$1.07 \times 10^{-5}$	$3.55 \times 10^{-5}$	0.302
S	6.59	$3.89 \times 10^{-6}$	$1.62 \times 10^{-5}$	0.240
Cl	4.70	$5.01 \times 10^{-8}$	$3.16 \times 10^{-7}$	0.159
Ar	5.81	$6.46 \times 10^{-7}$	$3.63 \times 10^{-6}$	0.178
Ca	5.69	$4.90 \times 10^{-7}$	$2.29 \times 10^{-6}$	0.214
Cr	5.10	$1.26 \times 10^{-7}$	$4.68 \times 10^{-7}$	0.269
Fe	6.84	$6.92 \times 10^{-6}$	$4.68 \times 10^{-5}$	0.148
Ni	5.85	$7.08 \times 10^{-7}$	$1.78 \times 10^{-6}$	0.398

\* The reference is Russell &amp; Dopita (1992).

† The solar abundance table is from the *angr* model (Anders & Grevesse, 1989).

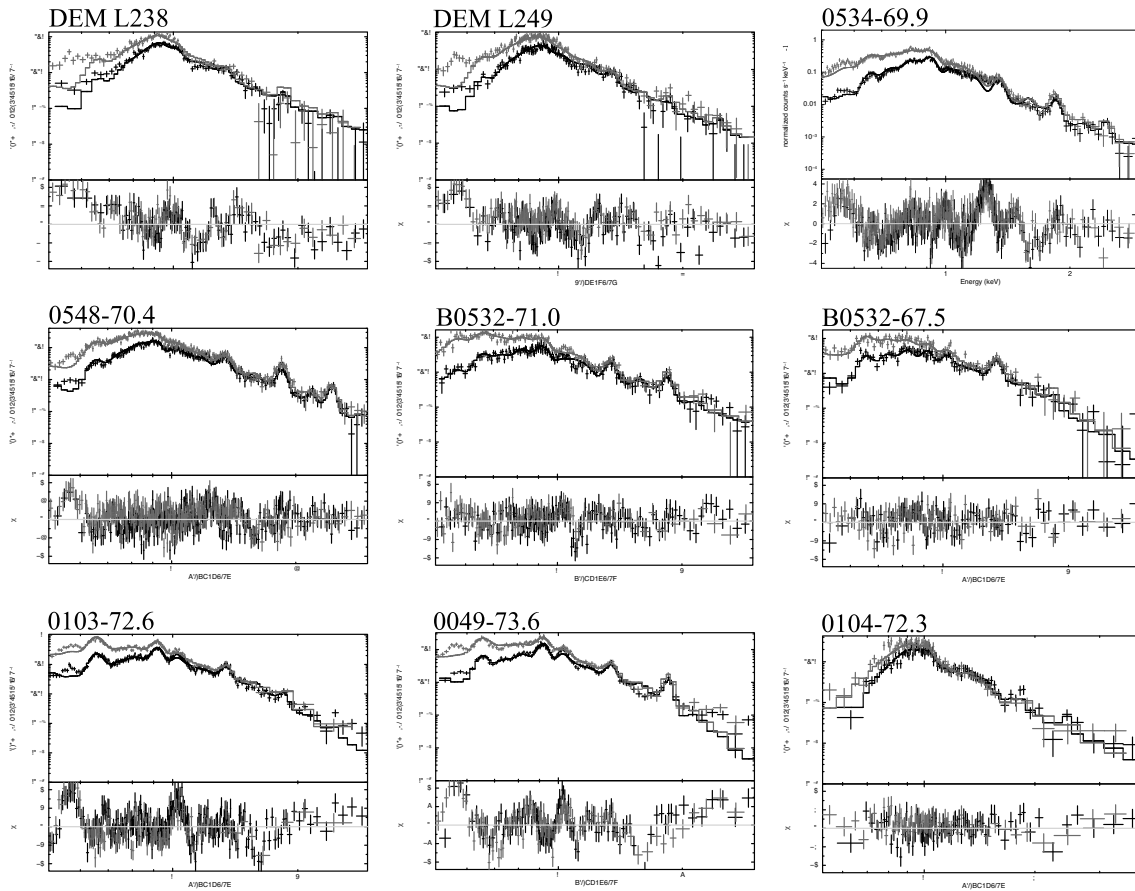


**Figure 7.2:** *Suzaku* XIS spectra of the MCs SNRs fitted with the  $1-kT_e$  NEI fit model. The names of the SNRs are labeled in upper left of each figure. The lower panel shows the residual from the best-fit model. The spectral parameters are listed in table 7.3. XIS FI and BI spectra are represented with black and red, respectively. The best-fit models are indicated by the solid curve.

**Table 7.3:** The best-fit spectral parameters of the one-temperature component with NEI<sup>◊</sup>.

Parameters	DEM L238	DEM L249	0534–69.9	0548–70.4	B0532–71.0	B0532–67.5	0103–72.6	0049–73.6	0104–72.3
$N_{\text{H}}^{\text{IC}*}$	0.0 (fixed)	0.0 (fixed)	0.0 (fixed)	0.0 (fixed)	0.0 (fixed)	0.0 (fixed)	0.0 (fixed)	0.0 (fixed)	$0_{-0}^{+13}$
(High temperature component)									
$kT_e$	$1.12 \pm 0.04$	$0.89 \pm 0.02$	$0.76 \pm 0.02$	$0.72_{-0.03}^{+0.03}$	$1.0_{-0.1}^{+0.2}$	$0.353_{-0.008}^{+0.012}$	$0.306 \pm 0.002$	$0.309 \pm 0.002$	$0.87 \pm 0.02$
$n_e t^\dagger$	$0.60 \pm 0.08$	$0.80 \pm 0.09$	$0.23 \pm 0.02$	$0.91 \pm 0.09$	$0.10_{-0.02}^{+0.03}$	100 (fixed)	100 (fixed)	100 (fixed)	100 (fixed)
(Abundances)									
O	0.263 (fixed)	0.263 (fixed)	0.263 (fixed)	0.263 (fixed)	0.263 (fixed)	0.263 (fixed)	0.16 $\pm$ 0.01	0.17 $\pm$ 0.02	0.126 (fixed)
Ne	$0.57 \pm 0.10$	$0.32 \pm 0.07$	$0.66 \pm 0.02$	$0.36_{-0.05}^{+0.04}$	$0.32_{-0.03}^{+0.03}$	$0.21_{-0.03}^{+0.04}$	$0.21 \pm 0.01$	$0.28 \pm 0.02$	$1.5_{-0.6}^{+0.8}$
Mg	$0.26 \pm 0.06$	$0.24 \pm 0.05$	$0.42 \pm 0.02$	$0.37_{-0.05}^{+0.05}$	$0.29_{-0.05}^{+0.06}$	$0.43_{-0.09}^{+0.10}$	$0.17 \pm 0.01$	$0.20 \pm 0.02$	$0.6_{-0.3}^{+0.4}$
Si	$0.7_{-0.2}^{+0.2}$	$0.13 \pm 0.07$	$0.51 \pm 0.04$	$0.74_{-0.09}^{+0.10}$	$0.7_{-0.2}^{+0.2}$	0.309 (fixed)	$0.22 \pm 0.03$	$0.88 \pm 0.08$	$0.3_{-0.2}^{+0.2}$
S	0.309 (fixed)	$0.3 \pm 0.2$	$1.4 \pm 0.2$	$1.5_{-0.3}^{+0.3}$	0.309 (fixed)	0.309 (fixed)	0.24 (fixed)	0.24 (fixed)	$1.2_{-0.5}^{+0.7}$
Fe	$0.83 \pm 0.07$	$0.67 \pm 0.07$	$0.50 \pm 0.01$	$0.34_{-0.03}^{+0.03}$	$0.22_{-0.03}^{+0.03}$	$0.08_{-0.01}^{+0.01}$	$0.024 \pm 0.002$	$0.043 \pm 0.004$	$0.36_{-0.07}^{+0.12}$
$\chi^2(d.o.f)$	3.07 (173)	2.17 (266)	2.46 (482)	1.50 (469)	1.22 (245)	1.22 (173)	2.64 (326)	3.22 (211)	1.19(88)

<sup>◊</sup>The uncertainties are in the 90% confidence range.

\* The unit is  $10^{20} \text{ cm}^{-2}$ .

† The unit is  $10^{11} \text{ cm}^{-3} \text{ s}$ .

The Galactic absorption ( $N_{\text{H}}^{\text{Gal}}$ ) was fixed to  $6 \times 10^{20} \text{ cm}^{-2}$ .

### 7.2.2 Two-temperature NEI model

The  $1-kT_e$  model yielded reasonable fits with  $\chi^2_\nu \sim 1.2\text{--}2.0$ , but introducing a two-temperature ( $2-kT_e$ ) NEI model resulted in significantly better fits for all the SNRs other than 0104–72.3. Next, we employed the  $2-kT_e$  NEI model for spectral fitting. We allowed  $kT_e$  and  $n_e t$  to vary independently in the two NEI components, but the elemental abundances were linked between them. Typical electron temperatures of the high- $kT_e$  and low- $kT_e$  components were 0.5–1.0 keV and 0.2–0.3 keV, respectively. The ionization parameter of the low- $kT_e$  component was found to be very high ( $\gtrsim 10^{12} \text{ cm}^{-3} \text{ s}$ ) in most SNRs, suggesting that this component is almost in the CIE state (see § 3.1). In this case, we fixed  $n_e t$  to  $1 \times 10^{13} \text{ cm}^{-3} \text{ s}$ , where the plasma is considered to be in the full CIE state. Introducing a two-temperature NEI model resulted in significantly better fits for all the SNRs other than 0104–72.3 as shown in figure 7.3. The  $2-kT_e$  NEI model best-fit parameters we obtained are given in table 7.4. Only in 0104–72.3 did the second component with a free electron temperature fail to improve the fit at all. Nevertheless, we attempted modeling with the two components by fixing the low- $kT_e$  value to 0.3 keV to determine the upper limit of the low- $kT_e$  emission measure. We also fitted the data of all the SNRs assuming the LMC/SMC abundances for the low- $kT_e$  component, but the abundances of the other component did not change significantly from the values listed in table 7.4.

The best-fit models and the residuals are shown in figure 7.3. In the first four spectra (DEML238, DEML249, 0534–69.9, and 0548–70.4), apparent disagreement between the data and model can be seen at energies around 1.2 keV. Given that large residuals are found only in the Fe-rich remnants (see table 7.4), this feature is likely to be associated with Fe L-shell emission. In fact, similar residuals were reported in a number of previous works (e.g., Brickhouse *et al.*, 2000; Yamaguchi *et al.*, 2011), and interpreted as Fe L-shell emission transitions from high quantum numbers ( $n > 5$ ), which are missing from the present plasma code. If we add a Gaussian to compensate for these missing lines, the  $\chi^2_\nu$  values are significantly reduced, but no change in the other best-fit parameters is confirmed.

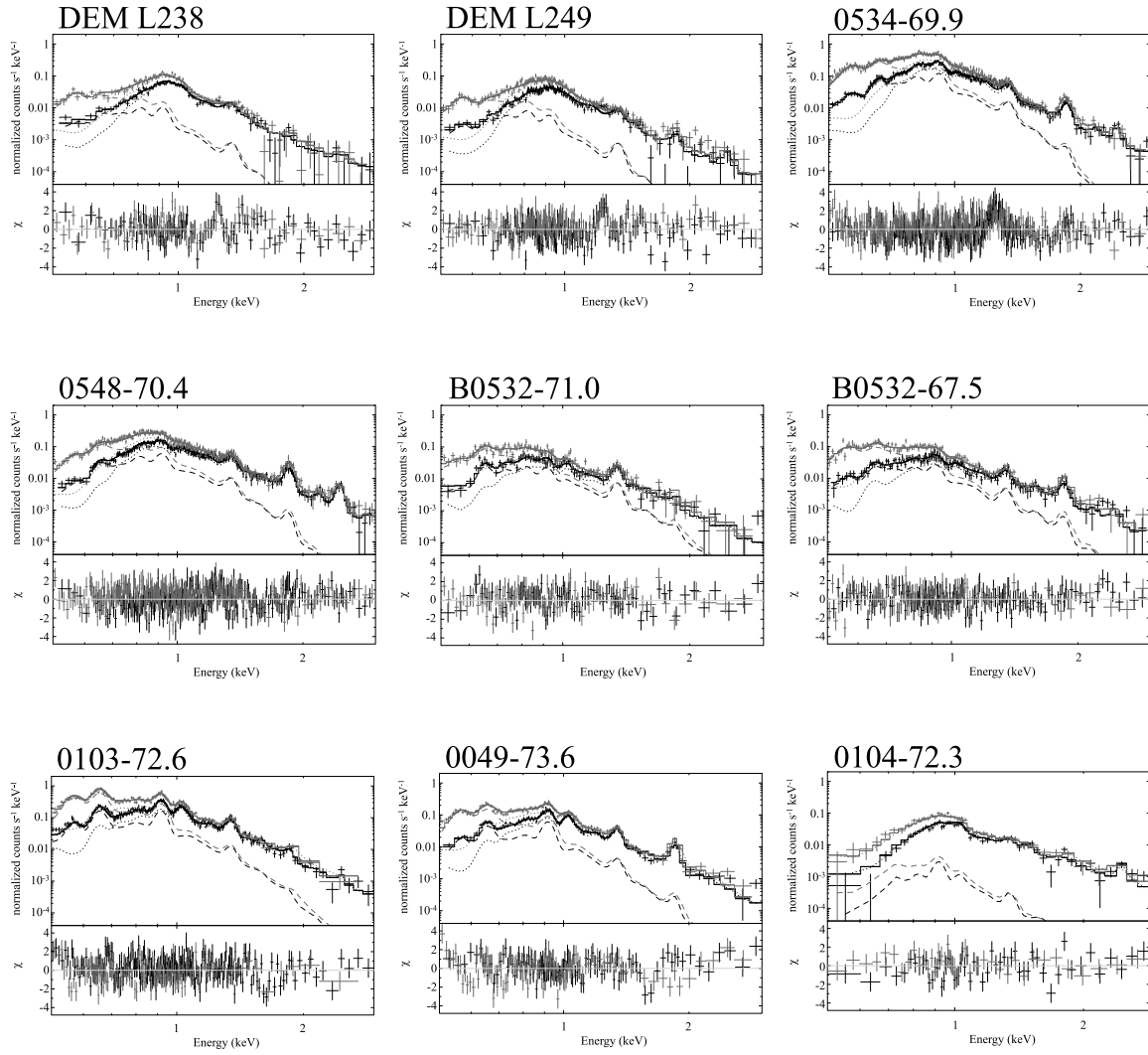


**Figure 7.3:** Same as figure 7.2 for a fit with the  $2\text{-}kT_e$  NEI model. The fit parameters we obtain are given in table 7.4.

Table 7.4: The best-fit spectral parameters of the two-temperature NEI model<sup>◊</sup>.

Parameters	DEM L238	DEM L249	0534-69.9	0548-70.4	B0532-71.0	B0532-67.5	0103-72.6	0049-73.6	0104-72.3
$N_{\text{H}}^{\text{MC}*}$	$0.0^{+6.3}_{-0.0}$	$4.3^{+13.8}_{-4.3}$	$34.2^{+11.8}_{-3.6}$	$49^{+12}_{-11}$	$0.16^{+9.07}_{-0.16}$	$8.2^{+22.5}_{-8.2}$	$0.0^{+1.2}_{-0.0}$	$0.0^{+1.3}_{-0.0}$	$0.45^{+12.83}_{-0.45}$
(High temperature component)									
$kT_e$	$1.05^{+0.10}_{-0.09}$	$0.86^{+0.14}_{-0.04}$	$0.68^{+0.03}_{-0.03}$	$0.68^{+0.04}_{-0.04}$	$0.63^{+0.15}_{-0.12}$	$0.73^{+0.25}_{-0.18}$	$0.52^{+0.04}_{-0.10}$	$0.63^{+0.03}_{-0.03}$	$0.88^{+0.05}_{-0.03}$
$n_e t^\dagger$	$1.16^{+0.72}_{-0.46}$	$2.06^{+1.58}_{-1.12}$	$1.47^{+0.48}_{-0.32}$	$1.53^{+0.99}_{-0.39}$	$2.44^{+9.21}_{-1.05}$	$1.09^{+3.37}_{-0.51}$	$3.34^{+4.84}_{-1.12}$	$1.81^{+0.51}_{-0.33}$	100 (fixed)
EM <sup>‡</sup>	$2.77^{+1.14}_{-0.90}$	$2.35^{+0.99}_{-0.90}$	$20.4^{+3.9}_{-2.9}$	$26.0^{+5.0}_{-3.7}$	$13.4^{+10.2}_{-4.6}$	$10.2^{+7.2}_{-3.9}$	$54^{+35}_{-11}$	$11.3^{+2.6}_{-2.3}$	$9.2^{+2.2}_{-2.1}$
(Low temperature component)									
$kT_e$	$0.172^{+0.005}_{-0.005}$	$0.173^{+0.018}_{-0.012}$	$0.169^{+0.003}_{-0.008}$	$0.181^{+0.007}_{-0.006}$	$0.259^{+0.035}_{-0.034}$	$0.277^{+0.153}_{-0.089}$	$0.202^{+0.011}_{-0.009}$	$0.186^{+0.007}_{-0.004}$	0.3 (fixed)
$n_e t^\dagger$	100 (fixed)	$10.2 \pm 9.3$	100 (fixed)	100 (fixed)	100 (fixed)	$0.89^{+3.30}_{-0.84}$	100 (fixed)	100 (fixed)	100 (fixed)
EM <sup>‡</sup>	$31^{+27}_{-16}$	$26^{+48}_{-15}$	$670^{+590}_{-250}$	$310^{+200}_{-130}$	$41^{+21}_{-15}$	$33^{+157}_{-29}$	$153^{+30}_{-23}$	$52^{+14}_{-11}$	$0.66^{+3.94}_{-0.66}$
(Abundances)									
O	$0.22^{+0.24}_{-0.12}$	$0.25^{+0.38}_{-0.13}$	$0.29^{+0.06}_{-0.08}$	$0.31^{+0.13}_{-0.04}$	0.263 (fixed)	0.263 (fixed)	$0.36^{+0.07}_{-0.06}$	$0.51^{+0.15}_{-0.11}$	0.126 (fixed)
Ne	$0.57^{+0.38}_{-0.32}$	$0.47^{+0.41}_{-0.36}$	$0.41^{+0.11}_{-0.09}$	$0.38^{+0.10}_{-0.07}$	$0.25^{+0.12}_{-0.06}$	$0.27^{+0.09}_{-0.04}$	$0.62^{+0.13}_{-0.06}$	$1.09^{+0.27}_{-0.19}$	$1.47^{+0.84}_{-0.77}$
Mg	$0.60^{+0.50}_{-0.26}$	$0.96^{+0.99}_{-0.45}$	$0.52^{+0.13}_{-0.09}$	$0.45^{+0.14}_{-0.08}$	$0.61^{+0.12}_{-0.15}$	$0.27^{+0.08}_{-0.07}$	$0.37^{+0.09}_{-0.06}$	$0.71^{+0.18}_{-0.14}$	$0.57^{+0.4}_{-0.27}$
Si	$0.18^{+0.3}_{-0.18}$	$0.74^{+0.81}_{-0.25}$	$0.76^{+0.19}_{-0.15}$	$0.97^{+0.25}_{-0.15}$	0.309 (fixed)	$0.66^{+0.25}_{-0.16}$	$0.21^{+0.06}_{-0.07}$	$1.25^{+0.3}_{-0.24}$	$0.26^{+0.23}_{-0.18}$
S	0.309 (fixed)	$1.12^{+0.94}_{-0.91}$	$0.70^{+0.33}_{-0.31}$	$1.75^{+0.49}_{-0.34}$	0.309 (fixed)	$0.59^{+0.72}_{-0.45}$	0.24 (fixed)	0.24 (fixed)	$1.24^{+0.72}_{-0.53}$
Fe	$1.62^{+0.81}_{-0.48}$	$1.96^{+1.13}_{-0.65}$	$1.12^{+0.23}_{-0.18}$	$0.60^{+0.17}_{-0.11}$	$0.17^{+0.06}_{-0.05}$	$0.16^{+0.05}_{-0.04}$	$0.10^{+0.01}_{-0.04}$	$0.32^{+0.09}_{-0.07}$	$0.36^{+0.13}_{-0.08}$
$\chi^2(d.o.f)$	1.41 (168)	1.25 (261)	1.26 (478)	1.22 (465)	1.16 (170)	1.00 (240)	1.31 (323)	1.30 (208)	1.20 (87)

<sup>◊</sup>The uncertainties are in the 90% confidence range.

\* The unit is  $10^{20} \text{ cm}^{-2}$ .

† The unit is  $10^{11} \text{ cm}^{-3} \text{ s}$ .

‡ The unit is  $10^{57} \text{ cm}^{-3}$ .

The Galactic absorption ( $N_{\text{H}}^{\text{Gal.}}$ ) was fixed to  $6 \times 10^{20} \text{ cm}^{-2}$ .



## Chapter 8

# DISCUSSION

We performed systematic studies of the nine evolved SNRs in the MCs using the spatially integrated spectra of the *Suzaku* XIS with the uniform data reduction and spectral modeling described in § 7.1. Despite the simplicity of our spectral modeling, we have been able to obtain reasonable fits and constraints on the elemental abundances of individual heavy elements. We found a significant variation in the chemical abundance pattern among the objects. In this section, we first give a brief summary of preceding works for comparison with our results, and then identify the best spectral feature to discriminate the progenitor type of the evolved SNRs (without spatially resolved analysis). Finally, we discuss the future outlook for the *ASTRO-H* and *Athena* X-ray missions on the basis of this analysis method.

### 8.1 Brief Summary of the Preceding Works and Our Results

#### 8.1.1 DEM L238 & DEM L249

Both SNRs were studied in detail with the *Chandra* and *XMM-Newton* X-ray satellites by Borkowski *et al.* (2006). Using the *Chandra* high-resolution data, they revealed that prominent Fe L-shell emission dominates the spectra from the SNR center, which suggests an SN Ia origin for both SNRs. Our analysis also confirms enhanced Fe abundances, whereas the abundances of the lighter elements (i.e., O, Ne, and Mg) are comparable to the mean LMC values. On the other hand, the ionization parameters we obtained (for the high- $kT_e$  component) are significantly an order of magnitude less than the previous measurements by Borkowski *et al.* (2006).

### 8.1.2 0534–69.9 & 0548–70.4

The first detailed studies of these SNRs were made by *Chandra* observations (Hendrick *et al.*, 2003). Similarly to DEML238 and DEML249, the SNR center spectra indicate strong Fe L-shell emission. The Balmer-dominated optical spectra of 0548–70.4 also suggest its SN Ia origin (Smith *et al.*, 1991, 1994). However, the O/Fe number ratio observed in this SNR is comparable to or higher than the mean LMC value (Hendrick *et al.*, 2003), which is unusual for SN Ia ejecta composition. As their interpretation, they considered two scenarios. One is that O is located in denser ejecta than Fe. The other is that they overestimated the electron temperature owing to the existence of unshocked Fe, which may still remain in the center. Our results confirm the strong Fe L-shell emission and reveal that the O/Fe ratio is significantly lower than in the previous measurement allowing us to reasonably conclude that it is as an evolved Type Ia SNR.

### 8.1.3 B0532–71.0

This SNR is associated with the HII region N206 in the LMC, and thus is sometimes called “the N206 SNR”. An elongated radio emission area can be observed between the SNR center and the east rim (Klinger *et al.*, 2002). A non-thermal X-ray emission is associated with this feature, suggesting the presence of a pulsar wind nebula and hence a CC origin of this SNR (Williams *et al.*, 2005). Abundance measurements were made by *Chandra* and *XMM-Newton* observations (Williams *et al.*, 2005). Our results are basically consistent with those of Williams *et al.* (2005).

### 8.1.4 B0532–67.5

The only preceding study of this SNR was performed by *ROSAT* (Haberl & Pietsch, 1999). Although *XMM-Newton* has also observed this SNR, the result is still unreported. We therefore also analyzed the *XMM-Newton* image, determining its angular size as given in table 6.1. An X-ray spectrum with sufficient photon statistics has been obtained by *Suzaku* (i.e., this work) for the first time.

### 8.1.5 0103–72.6

This SNR is located within the HII region DEMS125 in the SMC (e.g., Filipovic *et al.*, 1998), which implies its massive-star origin. The *ASCA* observation of this SNR

confirmed its elevated metal abundances (Yokogawa *et al.*, 2002), but the detailed chemical composition was not well constrained. The subsequent *Chandra* observation spatially resolved the central ejecta from the swept-up ISM shell (Park *et al.*, 2003a). The center spectrum indicates overabundances of O and Ne, consistent with the CC scenario. Our measurement also confirms enhanced Ne abundance even in the integrated spectrum of the entire SNR.

### 8.1.6 0049–73.6

This SNR is the one of three brightest X-ray SNRs in the SMC. A spatially resolved spectral analysis was performed in detail with *Chandra* (Hendrick *et al.*, 2005). The bright interior regions are dominated by O- and Ne-rich ejecta, suggesting a CC origin for this SNR, but the progenitor mass of  $\gtrsim 40 M_{\odot}$  was ruled out from the lack of a large stellar-wind bubble (which is expected for a very massive star). In addition, the latest *Chandra* measurement indicates out small metal-rich ejecta features extending to the outside, and the Si-rich material is highly structured (Schenck *et al.*, 2014). They suggested that this SNR was produced by an asymmetric core-collapse explosion of a  $\sim 13$ – $15 M_{\odot}$  massive star. Similarly to 0103–72.6, we confirm high abundances of Ne from the spatially integrated spectral data, whereas the Fe abundance is comparable to the mean SMC value.

### 8.1.7 0104–72.3 (a.k.a. IKT 25)

The progenitor type of this SNR in the SMC has been controversial. Using *XMM-Newton* data, van der Heyden *et al.* (2004) revealed an overabundance of Fe, and hence proposed an SN Ia origin. This was supported by a later *Chandra* observation by Lee *et al.* (2011). However, using higher-statistics *Chandra* data, Lopez *et al.* (2014) found that the measured Ne/Fe abundance ratio is consistent with an aspherical CC SN of a massive progenitor. They therefore proposed that this SNR arose from a jet-driven bipolar SN explosion. The star formation history at the periphery of this SNR also supports the CC scenario. Our analysis indicates a high Ne/Fe ratio, supporting the latest *Chandra* measurement by Lopez *et al.* (2014). This will be discussed in more detail in the following subsections.

## 8.2 Classification of SNRs with the Fe/Ne Abundance Ratio

As described above, we have confirmed the abundance enhancement of either Fe or lighter elements (i.e., O, Ne, and Mg) in most SNRs. For each, the progenitor type inferred from the abundance pattern agrees with the previous conclusions achieved by spatially resolved analysis with *Chandra*. This indicates that the integrated X-ray spectra of old (and thus ISM-dominant) SNRs are still contributed to by the SN ejecta and thus can be used to discriminate the progenitor types with simple, unbiased spectral modeling. It should be noted that the *ASCA* observations of the middle-aged Magellanic SNRs (Hughes *et al.*, 1998) did not indicate significantly elevated metal abundances, although the soft X-ray luminosities of their targets ( $L_{0.5-5 \text{ keV}} \approx 10^{36-37} \text{ erg s}^{-1}$ ) were one or two orders of magnitude higher than those of our samples (see table 7.4). Therefore, spectral sensitivity (i.e., effective area and energy resolution) is essential for precise progenitor determination, particularly for X-ray faint SNRs.

The most prominent difference in spectral features among the nine SNRs (figure 7.3) can be seen around 1 keV, where either Fe L-shell or Ne K-shell emission is dominant. In figure 8.1, we plot the measured Fe and Ne abundances (relative to H) for each SNR, clearly separating the remnants into the two distinct groups. Given this fact, we propose the Fe/Ne mass ratio as the best quantity to distinguish the progenitor type of evolved SNRs (especially when a spatially resolved spectrum is unavailable). The merit of this ratio is also justified from the theoretical viewpoint. First, Fe and Ne are the major products of Type Ia and CC SNe, respectively. Second, measurements of their abundance ratio are hardly affected by foreground extinction or the electron temperature of plasmas because of the similar transition energies of the Fe L-shell and Ne K-shell emission. Figure 8.2 shows the Fe/Ne mass ratio as a function of the SNR radius. All the values are significantly different from the mean LMC/SMC values for most SNRs.

We verify here that the measured mass ratios make sense by comparing them with theoretically expected values in which the ISM contribution is taken into account. The total observed mass of Fe and Ne can be divided into those of the ISM and ejecta components as

$$\frac{M_{\text{Fe}}}{M_{\text{Ne}}} = \frac{M_{\text{ISM,Fe}} + M_{\text{ejecta,Fe}}}{M_{\text{ISM,Ne}} + M_{\text{ejecta,Ne}}}. \quad (8.1)$$

Assuming a uniform ambient density of  $n_0$ , the Fe (and similarly Ne) mass in the ISM

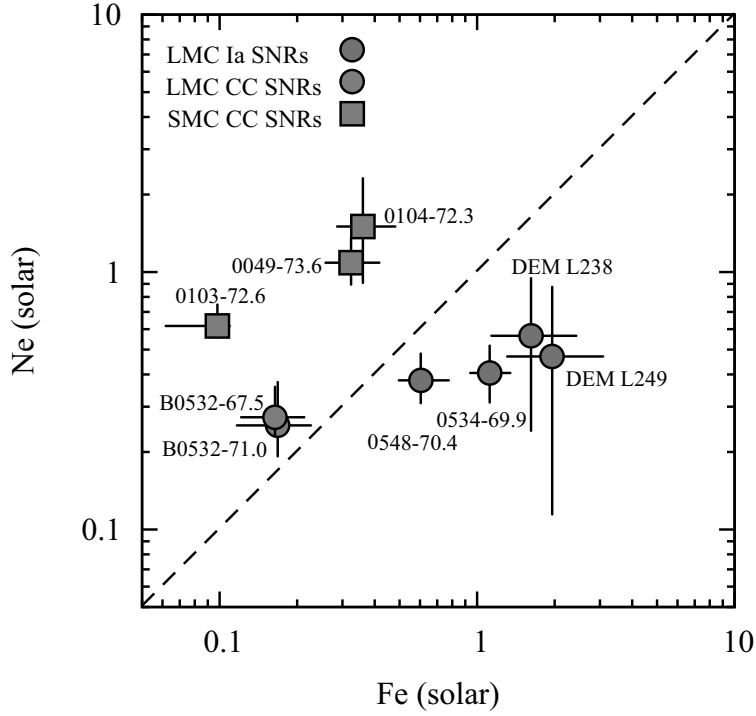


**Figure 8.1:** The relation of measured abundances of Fe and Ne for the SNRs in the LMC (circles) and the SMC (squares). Red and blue represent candidates of Type Ia and CC SNRs, respectively. The dash line indicate that the abundance of Ne is equal to that of Fe. (Takeuchi *et al.*, 2016)

component is calculated as

$$\begin{aligned}
 M_{\text{ISM, Fe}} &= m_{\text{Fe}} \cdot n_0 \left( \frac{n_{\text{Fe}}}{n_{\text{H}}} \right)_{\text{LMC}} \cdot V_{\text{SNR}} \\
 &= m_{\text{Fe}} \cdot n_0 \left( \frac{n_{\text{Fe}}}{n_{\text{H}}} \right)_{\text{LMC}} \left( \frac{4}{3} \pi R_{\text{SNR}}^3 \right), \quad (8.2)
 \end{aligned}$$

where  $m_{\text{Fe}}$ ,  $(n_{\text{Fe}}/n_{\text{H}})_{\text{LMC}}$ , and  $V_{\text{SNR}}$  are the mass of a single Fe atom, the mean Fe/H number ratio of the LMC (Russell & Dopita, 1992, see table 7.1), and the SNR volume, respectively. For  $n_0$ , we consider various values in the range between  $0.1 \text{ cm}^{-3}$  and  $10 \text{ cm}^{-3}$ . The assumption of uniform ambient density should be valid for most Type Ia SNRs (e.g., Badenes *et al.*, 2007; Yamaguchi *et al.*, 2014a). A massive star such as a red supergiant (RSG), on the other hand, usually explodes in circumstellar matter (CSM) formed by its own pre-explosion stellar wind. However, given a typical wind velocity ( $\sim 10 \text{ km s}^{-1}$ ) and length of the RSG stage ( $\sim 10^5 \text{ yr}$ ), the CSM contribution should be significant only up to a few parsecs (e.g., Dwarkadas, 2005), and thus the swept-up mass of the evolved SNRs should be dominated by the pre-existing ISM. The metal masses of the ejecta component

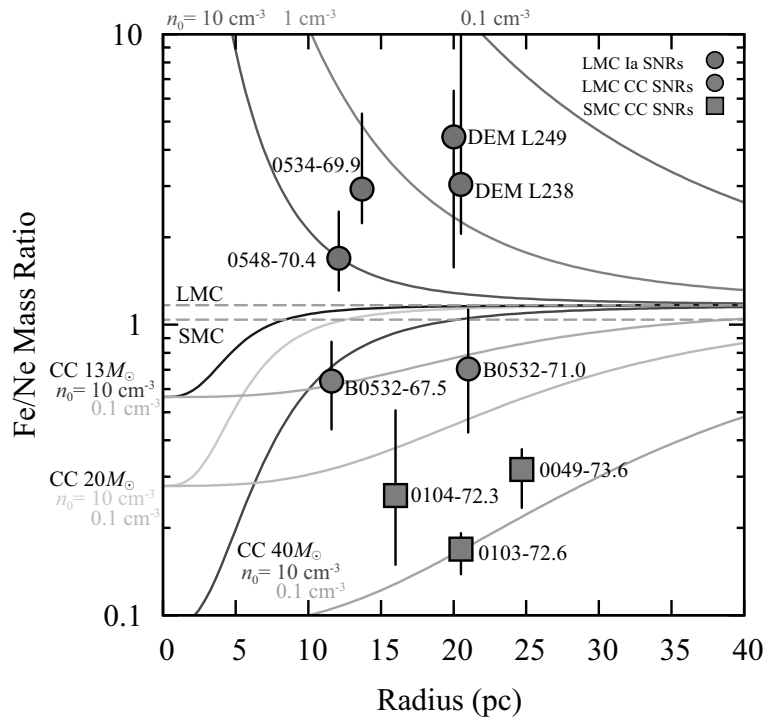


**Figure 8.2:** Fe/Ne mass ratios as a function of the SNR radius. The mean LMC and SMC mass ratios are indicated as dashed lines. The solid curves show the theoretical mass ratios, where both ISM and ejecta contributions are taken into account (see text for more details). For the ISM component, uniform ambient densities ( $n_0$ ) of 0.1–10  $\text{cm}^{-3}$  are assumed. The metal masses of the SN Ia ejecta are assumed to be those of the WDD2 model (Iwamoto *et al.*, 1999). For the CC SNRs, we use the values predicted by Kobayashi *et al.* (2006) for various progenitor masses between 13  $M_\odot$  and 40  $M_\odot$  with a metallicity of  $Z = 0.004$ . (Takeuchi *et al.*, 2016)

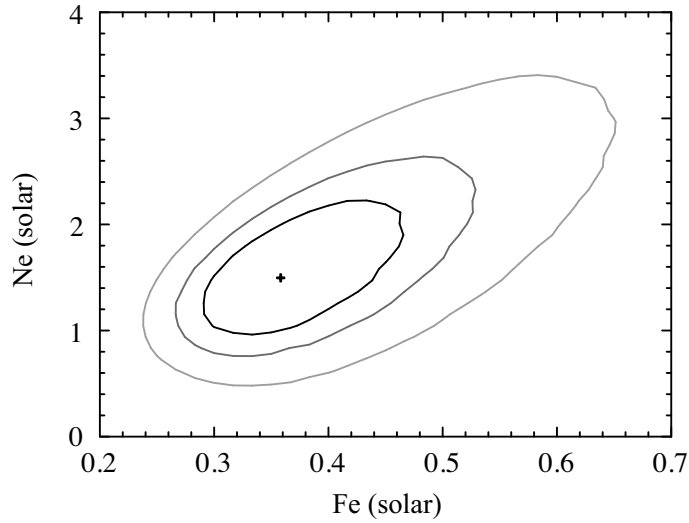


**Figure 8.3:** Confidence contour for the abundance ratio of Fe to Ne determined from the spectrum of 0104–72.3. Black, red, and green contours are given for confidence levels of 68%, 90%, and 99%, respectively. (Takeuchi *et al.*, 2016)

are taken from the literature values of Iwamoto *et al.* (1999) and Kobayashi *et al.* (2006) for SNe Ia and CC SNe, respectively. The calculated mass ratios as a function of the SNR radius are shown as the solid curves in figure 8.2. We confirm that most SNRs (both Type Ia and CC) are in good agreement with the theoretical curves.

More specifically, the mass ratios observed in the Type Ia SNRs DEM L238 and DEM L249 suggest their low ambient density ( $\lesssim 1 \text{ cm}^{-3}$ ), roughly consistent with the previous measurements (Borkowski *et al.*, 2006). On the other hand, the SNR 0548–70.4 requires a relatively high density ( $\sim 10 \text{ cm}^{-3}$ ), which is unusual for the LMC ISM. This implies that part of the Fe ejecta is still unshocked or forms a low-density plasma as explained in § 8.1. According to the theoretical curve for CC, several CC SNRs require a high progenitor mass. However, the absolute Fe ejecta mass of a CC SN is sensitive to a “mass cut” and is thus known to be somewhat uncertain. In fact, we find that some other CC SN models (e.g., Thielemann *et al.*, 1996) predict significantly lower Fe/Ne mass ratios for any progenitor mass. For  $13 M_{\odot}$ ,  $(M_{\text{Fe}}/M_{\text{Ne}})_{\text{ej.}} \sim 0.05$ . Moreover, our abundance measurements are based on phenomenological analysis with simple spectral modeling. We caution, therefore, that a plot such as figure 8.2 should not be used to accurately determine the progenitor mass of CC SNRs, although it is definitely useful for immediate SN-type discrimination.

The spectrum of SNR 0104–72.3 is somewhat peculiar. Despite no obvious feature of

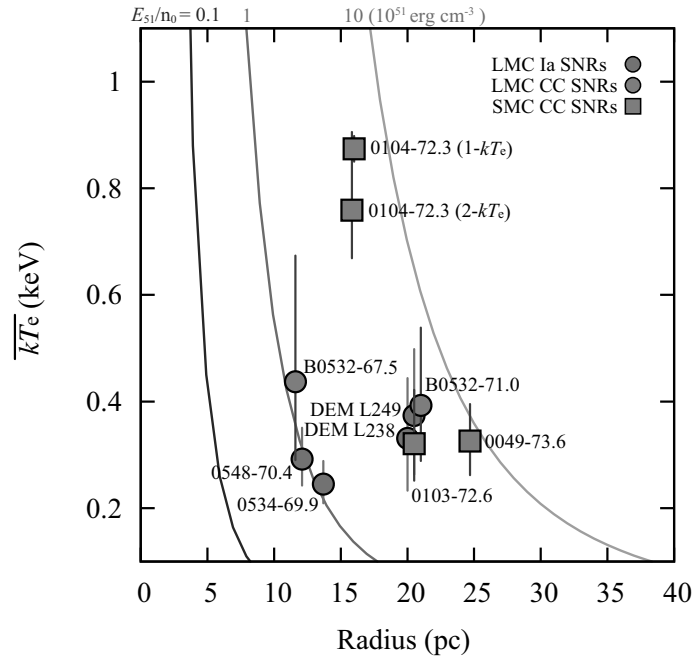


**Figure 8.4:** Density-weighted electron temperature as a function of the SNR radius. The solid curves indicate the relationship obtained from the Sedov solution with  $E_{51}/n_0 = 0.1$  (blue), 1 (red), and 10 (green), where  $E_{51}$  is the SN explosion energy in the unit of  $10^{51}$  erg.

Ne K-shell emission, the derived Fe/Ne ratio is similar to those of the other CC SNRs. As presented in figure 8.3, we show confidence contours for the abundance ratio of Fe to Ne, which is almost consistent with the previous measurements by Lopez *et al.* (2014). Unlike the other eight SNRs, 0104–72.3 does not require  $2\text{-}kT_e$  components to fit the spectrum, but we confirm that an additional low- $kT_e$  component (with a fixed temperature in the 0.1–0.3 keV range) does not change the Fe/Ne abundance ratio significantly. It is worth noting that the fitting results of 0104–72.3 (figures 7.2 and 7.3) show no residuals around 1.2 keV, which are commonly seen for the other Type Ia SNRs. This might be another piece of evidence for a low Fe abundance.

### 8.3 Electron Temperature Trend

Finally, we plot in figure 8.4 the density-weighted electron temperature ( $\overline{kT_e}$ ) for each SNR as a function of the SNR radius, which is calculated as

$$\overline{kT_e} = \frac{\sqrt{EM_{\text{high}}} \times kT_{e,\text{high}} + \sqrt{EM_{\text{low}}} \times kT_{e,\text{low}}}{\sqrt{EM_{\text{high}}} + \sqrt{EM_{\text{low}}}}. \quad (8.3)$$

The Sedov solution (see § 2.3.3) gives the following relationship between the electron temperature and the SNR radius:

$$kT_e = 0.56 \left( \frac{E_{51}}{n_0} \right) \left( \frac{R}{10 \text{ [pc]}} \right)^{-3} \text{ [keV]}, \quad (8.4)$$

where  $E_{51}$  is the SN explosion energy in the unit of  $10^{51}$  erg. The solid curves in figure 8.4 indicate this relationship for various combinations of  $E_{51}$  and  $n_0$ . Although this is a rough estimate, we can safely rule out the case of  $E_{51}/n_0 \lesssim 0.1$  (i.e., a very low energy explosion and/or a very high ambient density). According to the figure, DEM L238, DEM L249, B0532–71.0, and the three SMC CC SNRs should have evolved in the low-density ISM ( $n_0 \sim 0.1 \text{ cm}^{-3}$ ), as long as they had a normal explosion energy of  $\sim 10^{51}$  erg. This is consistent with the conclusion from the observed Fe/Ne mass ratios (figure 8.2) and/or the previous claims (Borkowski *et al.*, 2006; Williams *et al.*, 2005; Park *et al.*, 2003a; Hendrick *et al.*, 2005). On the other hand, the parent SNe of 0534–69.9 and 0548–70.4 may have been low-energy Type Ia explosions if they have a similar low ambient density. This is also consistent with previous works (Hendrick *et al.*, 2003).

## 8.4 Future Prospects

In this work, we have proved that the Fe/Ne mass ratio determined from a spatially integrated soft X-ray spectrum of an evolved SNR clearly discriminates its progenitor type when combined with sufficient energy resolution of the detector. *ASTRO-H*, the sixth Japanese X-ray Astronomy Mission, was launched in February 2016, and will enable the first high-resolution spectroscopy for greatly extended sources. The evolved Magellanic SNRs are suitable targets for this mission, because the typical spatial extent of the sources is too large to be observed with a grating spectrometer but is still smaller than the field of view of the Soft X-ray Spectrometer (SXS) aboard *ASTRO-H* ( $3' \times 3'$ : Takahashi *et al.*, 2014). The performance of the *ASTRO-H* SXS compared with that of *Suzaku* is listed in table 8.1.

Figure 8.5 (a) shows simulated SXS spectra of SNR 0104–72.3 with an exposure of only 25 ks, where we assume our best-fit model (black) or the Fe/Ne abundance ratio reported by Lee *et al.* (2011) (red). The two cases (i.e., CC and Type Ia) can easily be distinguished with this short exposure time since the strong Ly $\alpha$  emission is only expected for the CC scenario. For the other ‘normal’ SNRs, such as DEM L249 and 0103–72.6, we can resolve

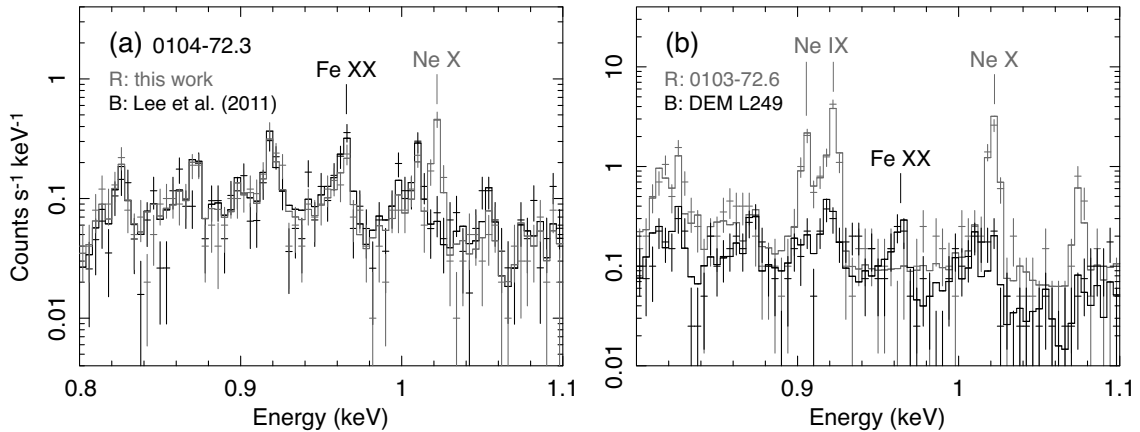


**Figure 8.5:** (a) Simulated spectra of SNR 0104–72.3 in the 0.8–1.1 keV band for observations with the SXS aboard *ASTRO-H*. We use parameters of our best-fit model (table 7.4) and the Fe/Ne abundance ratio reported by Lee *et al.* (2011) for the red and black data points, respectively. The assumed exposure time is only 25 ks for both cases. We can easily distinguish the two cases with this short exposure. (b) Simulated SXS spectra of DEM L249 (black) and 0103–72.6 (red) with the assumed exposures of 10 ks and 5 ks, respectively. (Takeuchi *et al.*, 2016)

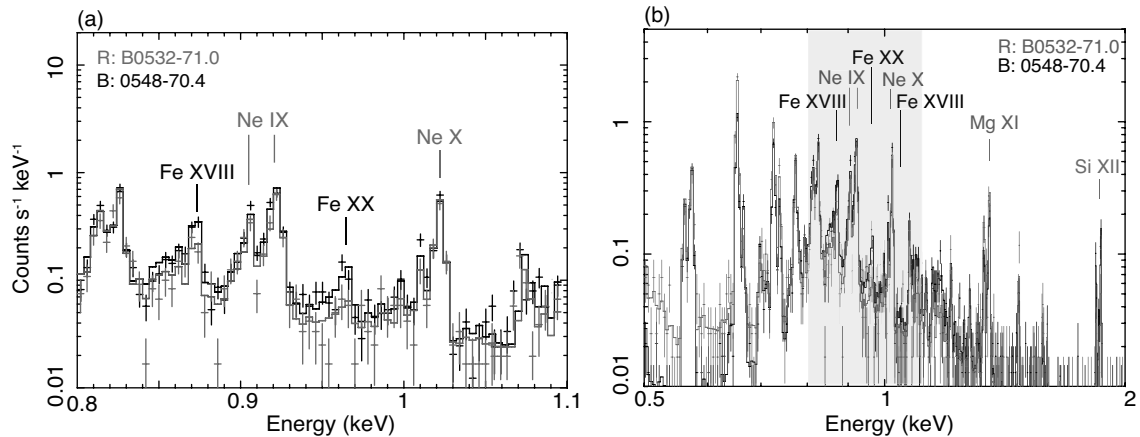


**Figure 8.6:** Simulated spectra of SNR B0532–71.0 (red) and SNR 0548–70.4 (black) which are relatively dominated by ISM component. The energy range is in (a) the 0.8–1.1 keV and (b) 0.5–2.0 keV. The left plot (a), linear scale, is the zoom of the bluish center part of right plot (b), log scale. The assumed exposure time is only 30 ks. The type of these SNRs can be marginally distinguished by Fe XVIII and Fe XX lines.

**Table 8.1:** Parameters of future X-ray mission instruments.

Satellite	<i>Suzaku</i>	<i>ASTRO-H</i> *	<i>Athena</i> †
Parameter	XIS (FI)	SXS	X-IFU
Detector technology	X-ray CCD	microcalorimeter	microcalorimeter
Field of View	17'8 × 17'8	~ 3' × 3'	goal 7'
Angular resolution	1'8 (HPD)	< 1'3 (HPD)	goal 3'' on-axis
Energy range	0.2–12 keV	0.3–12 keV	0.3–12 keV
Energy resolution	150 eV @ 6 keV	< 7 eV	goal 1.5 eV
Effective area	340 cm <sup>2</sup> @ 1.5 keV 350 cm <sup>2</sup> @ 8 keV	160 cm <sup>2</sup> @ 1 keV 210 cm <sup>2</sup> @ 6 keV	goal 2.5 m <sup>2</sup> @ 1 keV goal 0.3 m <sup>2</sup> @ 6 keV

\* Reference: Takahashi *et al.* (2014)

† Website :<http://www.the-athena-x-ray-observatory.eu>. Reference: Barret *et al.* (2015)

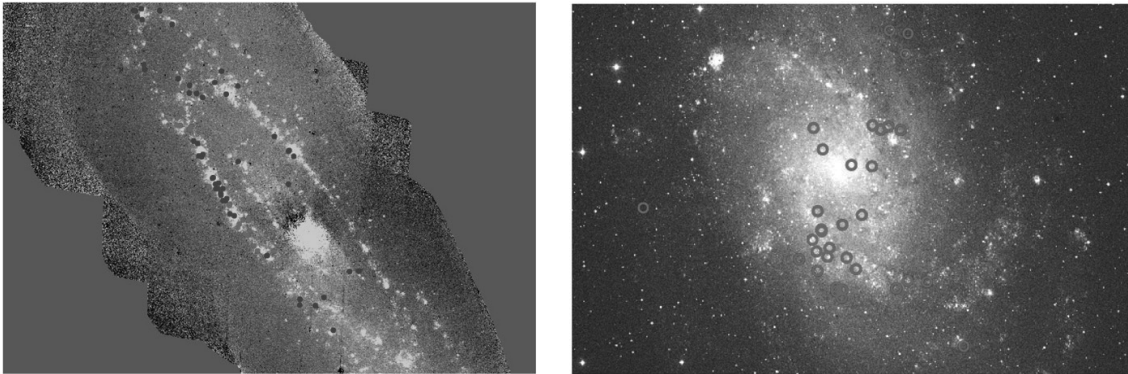


**Figure 8.7:** Left: Location map of the M31 SNRs superposed on a star-subtracted H $\alpha$  image of M31. SNRs are plotted as blue and red points. Right: Same as left figure, but for M33 SNRs. All figures taken from Jennings *et al.* (2014).

the key spectral features with an even shorter exposure time (5–10 ks) as demonstrated in figure 8.5 (b). The simulated spectra for the case of SNRs in which the ISM contribution is relatively large (e.g., B0532–71.0 and 0548–70.4) are shown in figure 8.6. We can marginally distinguish the progenitor type from the Fe XVIII and Fe XX lines even for these SNRs. Therefore, a systematic study of evolved SNRs is promising for *ASTRO-H*. In addition, *Athena* has been proposed as the next X-ray observatory for the European Space Agency (ESA) science mission, which is scheduled to be launched in 2028. The performance of the microcalorimeter called the X-ray Integral Field Unit (X-IFU) onboard *Athena* is greater than that of the *ASTRO-H* SXS (see table 8.1). Also the *Athena* mission is expected to have a  $\sim 100$  times larger effective area than *ASTRO-H*, compensating for the decrease in flux due to the large distance to the outer galaxies. Furthermore, because of the large distance to the SNRs and the high spatial resolution of the X-ray mirror, multiple SNRs can be detected in the observation and resolved with a single pointing observation. As a concrete example, M31, the closest spiral galaxy, known as the Andromeda galaxy, is a distance of  $\sim 750$  kpc. In the optical band, the *Hubble Space Telescope* discovered 86 SNRs in M31 and 33 SNRs in the M33 galaxy (second closest spiral galaxy, distance:  $\sim 900$  kpc; Jennings *et al.*, 2012) and obtained location maps of the combined M31 and M33 SNRs as presented in figure 8.7. In the X-ray band, the *XMM-Newton* EPIC (CCD camera) has so far detected 15 SNR candidates in M31. This observation image of M31 is shown in figure 8.8. Assuming SNRs with radius of 10 pc in M31, their angular size is estimated to be  $\sim 3''$ . Owing to its sufficient angular resolution, *Athena* will be able to detect these SNR candidates, which are observed similarly to a point source. *Athena* will be able to observe some SNR candidates in M33 with a typical angular size of  $\sim 2''.5$ . *Athena* will also allow us to perform similar studies on SNRs in closer galaxies. Thus, the study will help to understand the detailed chemical evolution in an entire spiral galaxy.

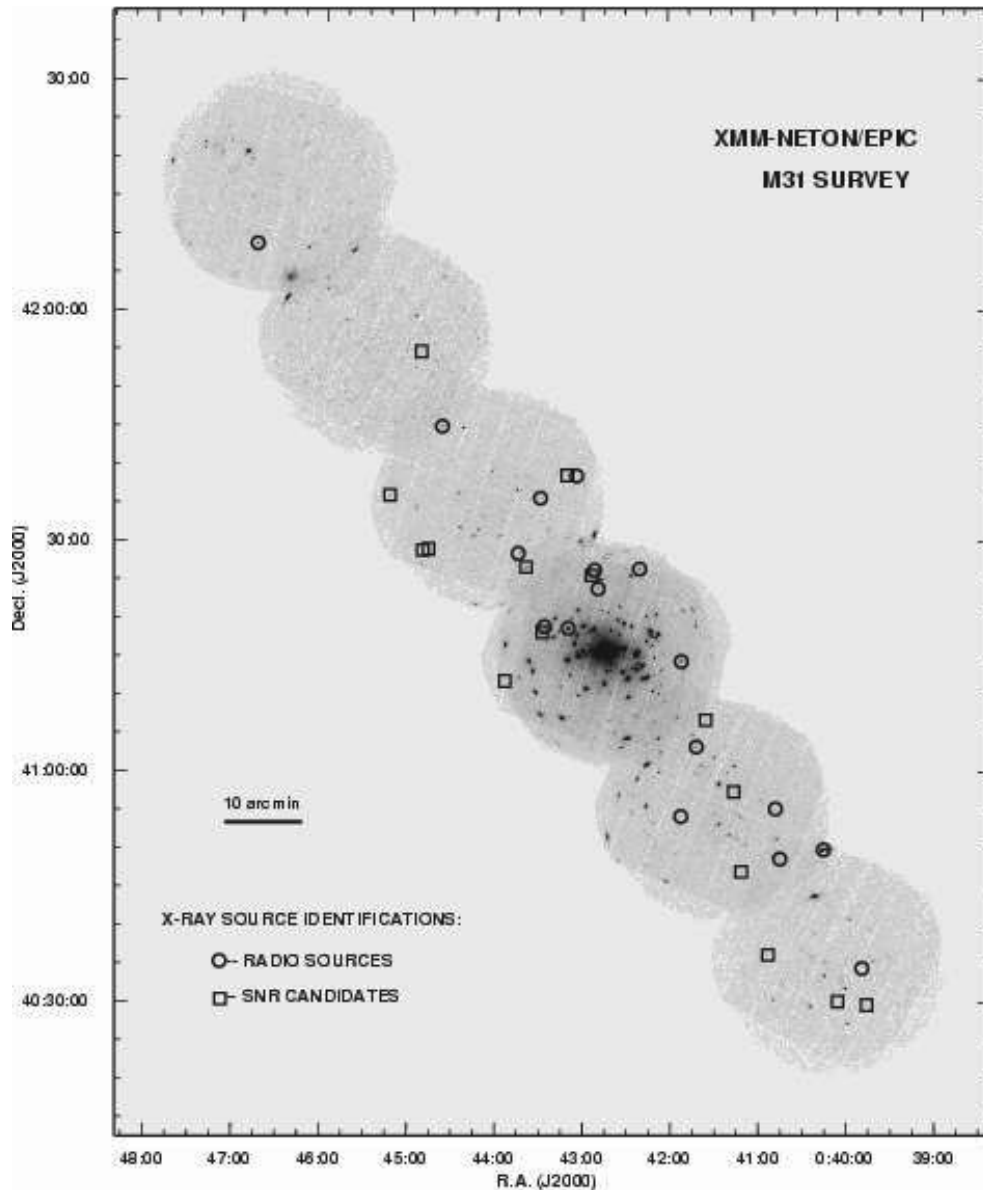


**Figure 8.8:** X-ray image of M31 with SNR candidates using the *XMM-Newton* EPIC (Trudolyubov & Priedhorsky, 2005).



## Chapter 9

# CONCLUSION

We have performed a systematic analysis of the SNRs in the LMC and SMC to establish a new observational diagnostic using high-energy-resolution spectra. The important results are summarized as follows:

- We have presented a systematic analysis of nine SNRs in the Magellanic Clouds (DEML238, DEML249, 0534–69.9, 0548–70.4, B0532–71.0, B0532–67.5, 0103–72.6, 0049–73.6, and 0104–72.3) observed with the *Suzaku* XIS. These are all evolved SNRs with an age of  $\gtrsim 10,000$  yr; thus, their integrated X-ray spectra in the soft X-ray band are dominated by the swept-up ISM. Nevertheless, we confirm clear signatures of the ejecta from all the observed targets.
- The Fe/Ne mass ratio derived from our simple unbiased spectral analysis clearly discriminates the progenitor types. DEML238, DEML249, 0534–69.9, and 0548–70.4 are classified as Type Ia remnants, while the other five are classified as CC SNRs; all these results are consistent with the previous *Chandra* results based on spatially resolved analysis. Since the Fe L-shell and Ne K-shell lines have almost the same energy range, measurements of their mass ratio are hardly affected by foreground extinction or the plasma temperature—this is a noteworthy advantage of this simple diagnostic.
- This analysis not only strengthens (or competes with) the previous classification made using *Chandra* but also identifies a key spectral feature that immediately distinguishes the SN type. This result should be useful for the future spectroscopic analysis of other galaxies. High-resolution spectroscopy using *ASTRO-H*/SXS will

resolve the key spectral features much more clearly with a very short exposure, enabling robust systematic studies of the Magellanic Sedov-phase SNRs. This will allow us to understand the recent chemical evolution in other galaxies in more detail.

# Appendix A

## ANALYSIS OF YOUNG SNRS

### A.1 Spectral Features

We analyze young SNRs, as defined in § 6.3. Figure A.1 shows the wide-band XIS FI and BI spectra of all young SNRs. The spectra of the two or three FI sensors were merged to improve the statistics because their response functions were almost identical. As shown in figure A.1, the K-shell emission of O, Ne, Mg, Si, S, Ar, Ca, and Fe, and/or the Fe L-shell emission are clearly separated in most spectra. Also, we detect the weak emission of iron-group elements (e.g., Cr, Mn, and Ni) in some spectra. On the other hand, some SNRs have no prominent lines above  $\sim 2$  keV. Since these spectra below 1.7 keV are dominated by Fe-L emission lines, we divided these spectra into two energy ranges: 0.5–1.7 keV for the lines of Ne and/or Fe L-shell and 1.7–9.0 keV for the K-shell emission lines of Si, S, Ar, Ca, and Fe. Below we focus on each energy range.

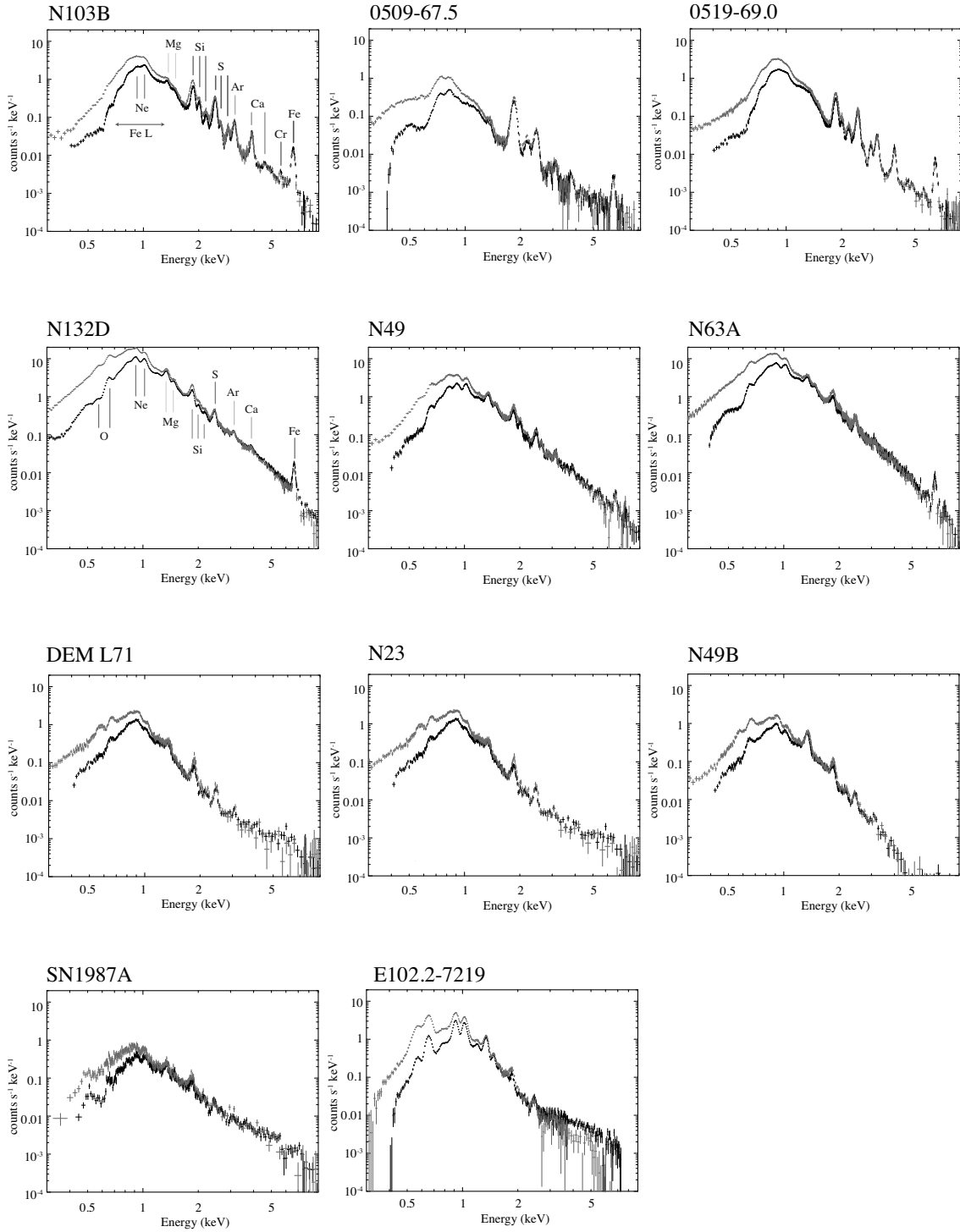


**Figure A.1:** *Suzaku* XIS spectra of the young LMC/SMC SNRs, where the background spectra are subtracted. The black and red data points represent the XIS FI and BI CCDs, respectively. The main emission lines are labeled in N103B and N132D.

## A.2 Model Fitting

### A.2.1 Two-temperature NEI model

To analyze these spectra around 1 keV and discuss the Fe and Ne abundance, we attempt to fit the 0.5–1.7 keV data by the  $2-kT_e$  NEI model, the same model as used for the evolved SNRs (see § 7.2.2). The best fit-model components and parameters are given in figure A.2 and table A.1, respectively. This model fails to reproduce the overall spectrum with an unacceptable  $\chi^2_\nu > 2.80$  other than for SN 1987A. In a young SNR, the reverse shock is still propagating toward the center of the ejecta. Because of different elapsed times from the shock passing through the element, the plasma state differs according to the location, making the plasma state very complex in a whole SNR. Thus, this method using the  $2-kT_e$  NEI model cannot be adapted to these young SNRs. We need to fit these spectra with a model base on multiple temperatures and the ionized state instead of the  $2-kT_e$  NEI model, which will not be attempted as part of this thesis.

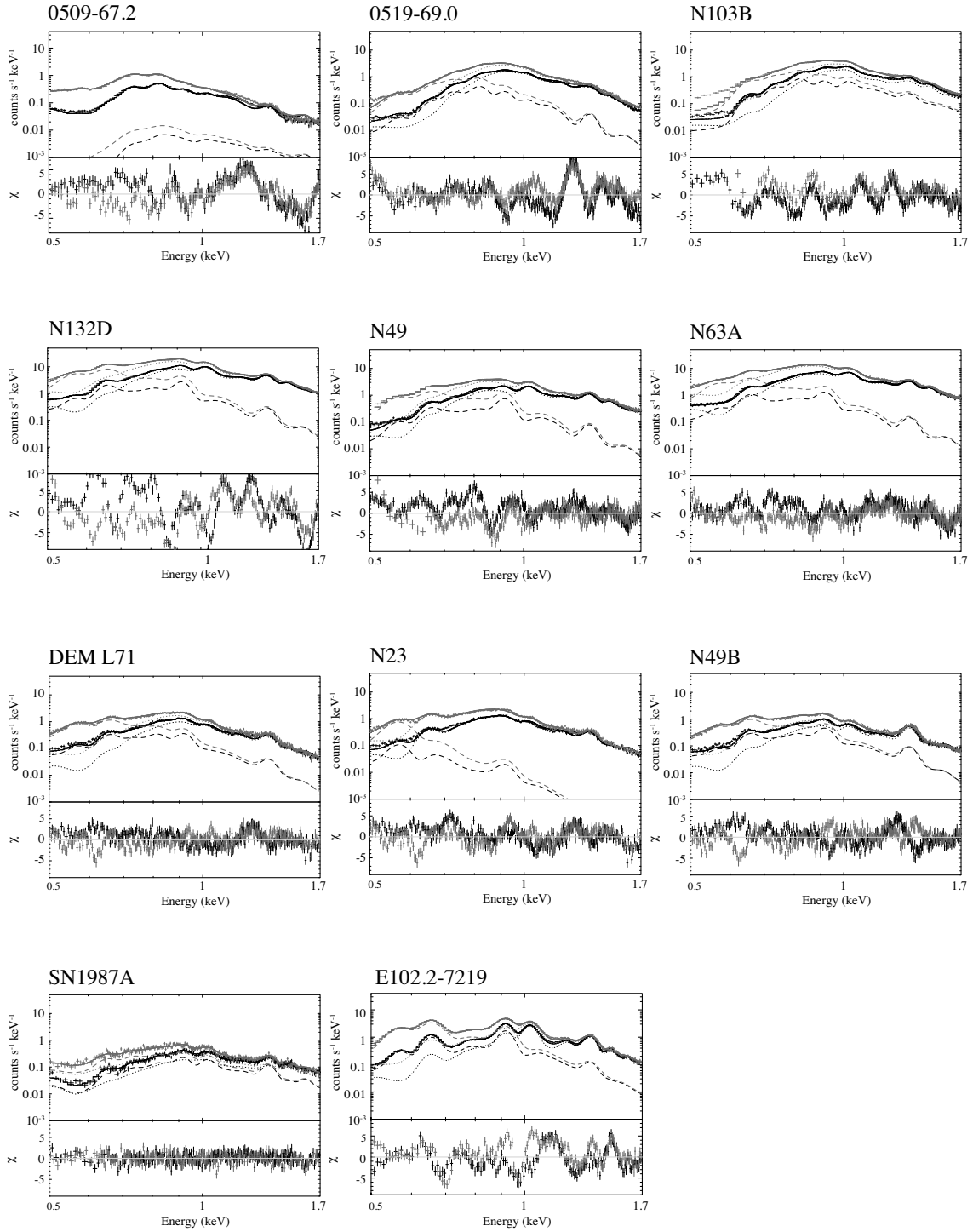


**Figure A.2:** *Suzaku* XIS spectra of the young MCs SNRs fitted with the  $2\text{-}kT_e$  NEI fit models. The names of the SNRs are labeled in upper left of each figure. The lower panel shows the residual from the best-fit model. The spectral parameters are listed in table A.1. The black and red data points represent the XIS FI and BI CCDs, respectively. The best-fit models are indicated by the solid curve.

**Table A.1:** The best-fit spectral parameters of the  $2-kT_e$  NEI model $^\diamond$ .

Parameters	0509-67.5	0519-69.0	N103B	N132D	N49	N63A	DEM L71	N23	N49B	SN 1987A
$N_{\text{H}}^{\text{MC}*}$	$3.57 \pm 0.16$	$5.3 \pm 0.11$	$7.58 \pm 0.10$	$1.35 \pm 0.03$	$4.8 \pm 0.17$	$1.1 \pm 0.1$	$0.91 \pm 0.20$	$0.00 \pm 0.01$	$2.8 \pm 0.3$	$0.034^{+0.031}_{-0.029}$
(High temperature component)										
$kT_e$	$0.58 \pm 0.44$	$0.819 \pm 0.002$	$0.907 \pm 0.001$	$0.713 \pm 0.001$	$0.604 \pm 0.004$	$0.688 \pm 0.003$	$0.78 \pm 0.01$	$0.764 \pm 0.005$	$0.651 \pm 0.008$	$0.86^{+0.06}_{-0.05}$
$\tau_{\text{e}t}^\dagger$	$2.2 \pm 23.8$	$2.75 \pm 0.09$	$4.39 \pm 0.20$	$4.38 \pm 0.06$	$16.7 \pm 5.9$	$5.90 \pm 0.21$	$1.58 \pm 0.10$	$1.15 \pm 0.04$	$1.61 \pm 0.11$	100 (fixed)
Norm $^\ddagger$	$0.16 \pm 0.49$	$4.95 \pm 0.09$	$9.2 \pm 0.3$	$105.3 \pm 0.6$	$22.5 \pm 0.8$	$71.4 \pm 1.7$	$5.0 \pm 0.2$	$5.4 \pm 0.2$	$10.1 \pm 0.2$	$4.0^{+0.6}_{-0.5}$
(Low temperature component)										
$kT_e$	$0.30 \pm 0.01$	$0.247 \pm 0.007$	$0.321 \pm 0.004$	$0.252 \pm 0.006$	$0.26 \pm 0.02$	$0.30 \pm 0.04$	$0.190 \pm 0.001$	$0.112 \pm 0.008$	$0.197 \pm 0.002$	$0.54^{+0.04}_{-0.05}$
$\tau_{\text{e}t}^\dagger$	$0.54 \pm 0.07$	$1.5 \pm 0.2$	100 (fixed)	$2.3 \pm 0.2$	$1.0 \pm 0.3$	$1.1 \pm 0.6$	100 (fixed)	100 (fixed)	$32 \pm 102$	$1.8^{+0.6}_{-0.3}$
Norm $^\ddagger$	$35.0 \pm 4.4$	$8.4 \pm 1.1$	$12.6 \pm 0.8$	$60.3 \pm 4.3$	$10.5 \pm 2.9$	$13.7 \pm 5.4$	$28.9 \pm 3.3$	$19.5 \pm 6.2$	$59.4 \pm 5.1$	$3.6^{+0.7}_{-0.6}$
(Abundances)										
O	$0.045 \pm 0.002$	$0.73 \pm 0.04$	$2.45 \pm 0.17$	$0.51 \pm 0.01$	$1.34 \pm 0.01$	$0.65 \pm 0.05$	$0.36 \pm 0.02$	$0.81 \pm 0.07$	$0.263$ (fixed)	$0.08 \pm 0.02$
Ne	$0.079 \pm 0.004$	$0.84 \pm 0.04$	$1.38 \pm 0.08$	$0.73 \pm 0.01$	$1.56 \pm 0.07$	$0.87 \pm 0.03$	$0.52 \pm 0.03$	$0.52 \pm 0.02$	$0.422 \pm 0.008$	$0.25^{+0.04}_{-0.03}$
Mg	$0.063 \pm 0.004$	$0.58 \pm 0.02$	$0.55 \pm 0.03$	$0.423 \pm 0.004$	$0.72 \pm 0.03$	$0.48 \pm 0.01$	$0.54 \pm 0.03$	$0.49 \pm 0.02$	$0.73 \pm 0.01$	$0.28 \pm 0.03$
Fe	$0.184 \pm 0.009$	$1.64 \pm 0.04$	$1.20 \pm 0.05$	$0.195 \pm 0.002$	$0.34 \pm 0.01$	$0.206 \pm 0.004$	$0.63 \pm 0.02$	$0.61 \pm 0.02$	$0.222 \pm 0.005$	$0.065^{+0.008}_{-0.004}$
$\chi^2_{\text{d.o.f}}$	5.15 (549)	7.90 (610)	9.06 (451)	22.6 (315)	4.60 (612)	3.80 (645)	2.80 (566)	3.95 (544)	3.84 (608)	1.17 (467)

$^\diamond$ The uncertainties are in the 90% confidence range.

\* The unit is  $10^{21} \text{ cm}^{-2}$ .

$^\dagger$  The unit is  $10^{11} \text{ cm}^{-3} \text{ s}$ .

$^\ddagger$  The unit is  $10^{-3} \text{ cm}^{-5}$ .

The Galactic absorption ( $N_{\text{H}}^{\text{Gal.}}$ ) was fixed to  $6 \times 10^{20} \text{ cm}^{-2}$ .

### A.2.2 Single Gaussian model

For a systematic analysis above  $\sim 1.7$  keV, we focus on prominent emission lines to determine each line parameter and plasma state. This method was inspired by previous research using Fe  $K\alpha$  emission (see § 4.4 and Yamaguchi *et al.*, 2014a). Six of the young SNRs have clear K-shell emissions of not only Si but also S, Ar, Ca, and Fe. Hereafter, we consider only these six SNRs: N103B, 0509–67.5, 0519–69.0, N49, N63A, and N132D. We used only the FI sensor data. The spectra of the FI sensors were merged to improve the statistics. In SNRs 0509–67.5 and N132D, moreover, the spectra of other observation IDs were merged.

We fitted these 1.7–9.0 keV spectra with a phenomenological model. This model we used is the absorbed continuum component(s) plus 25 Gaussian components for emission lines. We name this model the “single Gaussian model”, since a single Gaussian is applied to each line. The continuum emission originates from non-thermal synchrotron radiation, thermal bremsstrahlung radiation, and their combination. To estimate the continuum component, we assume the following four models:

- (1) a power-law model,
- (2) a bremsstrahlung model,
- (3) a power law + bremsstrahlung model,
- (4) a two-bremsstrahlung model.

Twenty of the Gaussians represent the  $\text{He}\alpha$  ( $n = 2 \rightarrow n = 1$  transition in He-like ion),  $\text{He}\beta$  ( $1s3p \rightarrow 1s^2$  transition in He-like ion),  $\text{He}\gamma$  ( $1s4p \rightarrow 1s^2$  transition in He-like ion),  $\text{Ly}\alpha$  ( $n = 2 \rightarrow n = 1$  transition in H-like ion), and  $\text{Ly}\beta$  ( $3p \rightarrow 1s$  transition in H-like ion) emission lines of Si, S, Ar, and Ca. The other five Gaussians represent the  $K\alpha$  emission lines of Fe, Cr, Mn, and Ni, and the  $K\beta$  emission line of Fe.

In the fitting, the free parameters were the line centroid, width, and flux of the prominent  $\text{He}\alpha$  lines of Si, S, Ar, and Ca and the  $\text{He}\beta$  lines of Si, and S, and  $K\alpha$  of Fe. Because the other lines are too weak, their energies were fixed to the energy difference from the  $\text{He}\beta$  line of the same element. For Cr, Mn, and Ni, however, we fixed the energy difference as that from Fe  $K\alpha$ . We used the energy difference from *AtomDB* in the fitting. The line widths were fixed to that of the  $\text{He}\beta$  line of the same element. The intensities of the prominent lines (e.g.,  $\text{He}\alpha$ ,  $\text{He}\beta$ , and  $\text{Ly}\alpha$ ) were not fixed. For other lines, we fixed the intensity ratios (e.g.,  $\text{He}\gamma = 0.3 \times \text{He}\beta$  and  $\text{Ly}\beta = \text{He}\beta / \text{He}\alpha \times \text{Ly}\alpha$ , tentatively assuming  $kT_e = 1$  keV and  $n_e t = 10^{11} \text{ cm}^{-3} \text{ s}$ , typical values for SNR N103B. Lewis *et al.*, 2003). The limits of

**Table A.2:** List of parameter conditions for the gaussian models.

Element	line	energy (keV)	width (eV)	intensity
Si	He $\alpha$	1.82 – 1.88	free	free
	He $\beta$	2.16 – 2.20	free	free
	He $\gamma$	=Si He $\beta$ +0.111	=Si He $\beta$	= 0.3 $\times$ Si He $\beta$
	Ly $\alpha$	=Si He $\beta$ -0.177	=Si He $\beta$	free
	Ly $\beta$	=Si He $\beta$ +0.194	=Si He $\beta$	=He $\beta$ /He $\alpha$ $\times$ Ly $\alpha$
S	He $\alpha$	2.42 – 2.48	free	free
	He $\beta$	2.84 – 2.90	free	free
	He $\gamma$	=S He $\beta$ +0.149	=S He $\beta$	= 0.3 $\times$ S He $\beta$
	Ly $\alpha$	=S He $\beta$ -0.261	=S He $\beta$	free
	Ly $\beta$	=S He $\beta$ +0.223	=S He $\beta$	=He $\beta$ /He $\alpha$ $\times$ Ly $\alpha$
Ar	He $\alpha$	3.00 – 3.17	free	free
	He $\beta$	=Ar He $\alpha$ +0.561	=Ar He $\alpha$	free
	He $\gamma$	=Ar He $\beta$ +0.190	=Ar He $\alpha$	= 0.3 $\times$ Ar He $\beta$
	Ly $\alpha$	=Ar He $\beta$ -0.362	=Ar He $\alpha$	free
	Ly $\beta$	=Ar He $\beta$ +0.251	=Ar He $\alpha$	=He $\beta$ /He $\alpha$ $\times$ Ly $\alpha$
Ca	He $\alpha$	3.68 – 4.00	free	free
	He $\beta$	=Ca He $\alpha$ +0.561	=Ca He $\alpha$	free
	He $\gamma$	=Ca He $\beta$ +0.190	=Ca He $\alpha$	= 0.3 $\times$ Ca He $\beta$
	Ly $\alpha$	=Ca He $\beta$ -0.362	=Ca He $\alpha$	free
	Ly $\beta$	=Ca He $\beta$ +0.251	=Ca He $\alpha$	=He $\beta$ /He $\alpha$ $\times$ Ly $\alpha$
Cr	K $\alpha$	5.40 – 5.75	=Fe K $\alpha$	free
Mn	K $\beta$	5.88 – 6.10	=Fe K $\alpha$	free
Fe	K $\alpha$	6.40 – 7.00	free	free
	K $\beta$	7.06 – 7.60	=Fe K $\alpha$	free
Ni	K $\alpha$	7.46 – 7.80	=Fe K $\alpha$	free

the Gaussian parameters are summarized in table A.2. The Galactic and MC absorption column densities were set to those in model in § 7.2, with the same conditions applied. We fitted the spectra of the six SNRs using the four models. Individual components of the best-fit models for the six SNRs are shown in figures A.3–A.8, and the best-fit parameters of all the fits are listed in tables A.3–A.8. We attempted a systematic study of young SNRs using line emission parameters but, unfortunately, we cannot find clear evidence of behavior distinguishing each progenitor type (Type Ia and CC SNR).

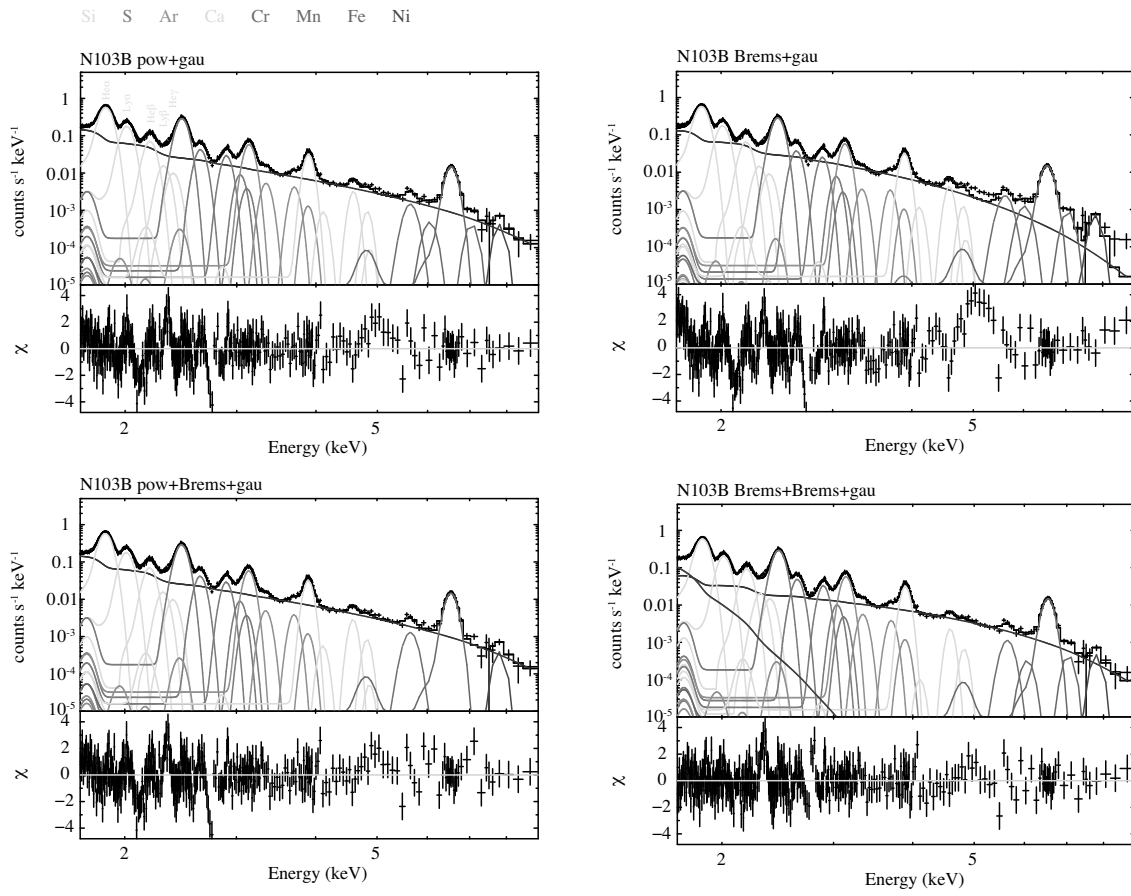


**Figure A.3:** The fitting results of SNR N103B for four type models.

Table A.3: The best-fit parameters with multi-gaussians + continuum model in N103B $\diamond$ .

Model	power-law			Brems.			power-law+Brems.			Brems.+Brems.		
	Centroid keV	Width eV	Norm $\dagger$	Centroid keV	Width eV	Norm $\dagger$	Centroid keV	Width eV	Norm $\dagger$	Centroid keV	Width eV	Norm $\dagger$
MC* $n_{\text{H}}$	0.36 (fixed)			0.36 (fixed)			0.36 (fixed)			0.36 (fixed)		
Continuum1	3.75 $\pm$ 0.014	1.20 $\pm$ 0.02		1.20 $\pm$ 0.02			3.69 $\pm$ 0.014			Brems.1: (keV)	2.11 $\pm$ 0.027	
Norm $\dagger$	4.93 $\pm$ 0.067	3.83 $\pm$ 0.15		3.83 $\pm$ 0.15			4.71 $\pm$ 0.063			Brems.2: (keV)	1.11 $\pm$ 0.02	
Continuum2	—	—		—			0.04 $\pm$ -1			0.1590 $^{+0.0006}_{-0.0006}$		
Norm $\dagger$	—	—		—			971 $\pm$ -1			17.8 $\pm$ 40.8		
Line	Centroid keV	Width eV	Norm $\dagger$	Centroid keV	Width eV	Norm $\dagger$	Centroid keV	Width eV	Norm $\dagger$	Centroid keV	Width eV	Norm $\dagger$
Si Hex	1.8632 $^{+0.0005}_{-0.0004}$	6.33 $^{+0.89}_{-0.91}$	549.4 $\pm$ 6.4	1.8619 $\pm$ 0.0003	8.33 $\pm$ 1.5	551.2 $\pm$ 12.0	1.8628 $^{+0.0005}_{-0.0004}$	5.75 $^{+0.92}_{-0.94}$	554.6 $\pm$ 6.5	1.8627 $\pm$ 0.0004	8.35 $^{+0.71}_{-0.77}$	556.3 $\pm$ 6.3
Si Ly $\alpha$	=Si He $\beta$ -0.177	=Si He $\beta$	108.7 $\pm$ 2.6	=Si He $\beta$ -0.177	=Si He $\beta$	107.3 $\pm$ 1.9	=Si He $\beta$ -0.177	=Si He $\beta$	109.4 $\pm$ 2.6	=Si He $\beta$ -0.177	=Si He $\beta$	124.6 $\pm$ 2.6
Si He $\beta$	2.1890 $^{+0.0023}_{-0.0023}$	6.7e-3 $\pm$ 0.05	40.7 $\pm$ 1.5	2.189 $\pm$ 0.001	3.4e-4 $\pm$ 0.3	37.3 $\pm$ 1.3	2.1889 $\pm$ 0.0009	0.001 $\pm$ -1	40.4 $\pm$ 1.5	2.189 $^{+0.002}_{-0.001}$	3.8e-4 $\pm$ 6.3e-3	53.5 $\pm$ 1.5
S Hex	2.4579 $^{+0.0010}_{-0.0007}$	16.1 $^{+2.2}_{-2.4}$	238.3 $\pm$ 3.5	2.458 $\pm$ 0.0006	15.0 $\pm$ 1.6	234.4 $\pm$ 2.3	2.4580 $^{+0.0010}_{-0.0007}$	17.1 $^{+2.1}_{-2.3}$	239.0 $\pm$ 3.5	2.4583 $^{+0.0009}_{-0.0008}$	19.2 $^{+1.9}_{-2.0}$	246.4 $\pm$ 3.5
S Ly $\alpha$	=S He $\beta$ -0.261	=S He $\beta$	30.0 $\pm$ 1.5	=S He $\beta$ -0.261	=S He $\beta$	26.37 $\pm$ 1.1	=S He $\beta$ -0.261	=S He $\beta$	29.4 $\pm$ 1.5	=S He $\beta$ -0.261	=S He $\beta$	34.4 $\pm$ 1.5
S He $\beta$	2.891 $^{+0.002}_{-0.003}$	0.89 $^{+5.20}_{-0.89}$	20.4 $\pm$ 1.1	2.893 $\pm$ 0.004	4.4e-3 $\pm$ 0.0	17.4 $\pm$ 0.8	2.8929 $^{+0.0008}_{-0.002}$	0.006 $\pm$ 0.154	20.0 $\pm$ 1.1	2.893 $^{+0.002}_{-0.003}$	1.9 $\pm$ 18.0	23.0 $\pm$ 1.0
Ar Hex	3.140 $\pm$ 0.002	18.0 $^{+5.5}_{-7.2}$	42.1 $\pm$ 1.5	3.139 $\pm$ 0.002	11.8 $\pm$ 5.7	40.4 $\pm$ 1.0	3.140 $\pm$ 0.002	16.7 $^{+5.8}_{-8}$	41.7 $\pm$ 1.5	3.141 $\pm$ 0.002	19.8 $^{+5.2}_{-6.5}$	42.4 $\pm$ 1.5
Ar Ly $\alpha$	=Ar He $\alpha$ +0.199	=Ar He $\alpha$	3.78 $\pm$ 0.74	=Ar He $\alpha$ +0.199	=Ar He $\alpha$	2.4 $\pm$ 0.5	=Ar He $\alpha$ +0.199	=Ar He $\alpha$	3.47 $\pm$ 0.73	=Ar He $\alpha$ +0.199	=Ar He $\alpha$	4.04 $\pm$ 0.74
Ar He $\beta$	=Ar He $\alpha$ +0.561	=Ar He $\alpha$	2.92 $\pm$ 0.59	=Ar He $\alpha$ +0.561	=Ar He $\alpha$	2.2 $\pm$ 0.4	=Ar He $\alpha$ +0.561	=Ar He $\alpha$	2.66 $\pm$ 0.59	=Ar He $\alpha$ +0.561	=Ar He $\alpha$	2.7 $\pm$ 0.6
Ca Hex	3.870 $\pm$ 0.003	13.3 $^{+9.9}_{-13}$	20.71 $\pm$ 0.94	3.897 $\pm$ 0.002	16.25 $\pm$ 6.8	20.7 $\pm$ 0.7	3.897 $\pm$ 0.003	11 $\pm$ 11	20.49 $\pm$ 0.93	3.896 $\pm$ 0.003	8 $^{+12}_{-8}$	20.23 $\pm$ 0.93
Ca Ly $\alpha$	=Ca He $\alpha$ +0.214	=Ca He $\alpha$	0.62 $\pm$ 0.45	=Ca He $\alpha$ +0.214	=Ca He $\alpha$	0.80 $\pm$ 0.32	=Ca He $\alpha$ +0.214	=Ca He $\alpha$	0.38 $^{+0.45}_{-0.38}$	=Ca He $\alpha$ +0.214	=Ca He $\alpha$	0.07 $\pm$ 0.51
Ca He $\beta$	=Ca He $\alpha$ +0.690	=Ca He $\alpha$	2.24 $\pm$ 0.41	=Ca He $\alpha$ +0.690	=Ca He $\alpha$	2.9 $\pm$ 0.3	=Ca He $\alpha$ +0.690	=Ca He $\alpha$	1.99 $\pm$ 0.41	=Ca He $\alpha$ +0.690	=Ca He $\alpha$	1.58 $\pm$ 0.41
Cr K $\alpha$	5.64 $\pm$ 0.03	=Fe K $\alpha$	1.90 $\pm$ 0.46	5.621 $\pm$ 0.017	=Fe K $\alpha$	3.3 $\pm$ 0.3	5.655 $\pm$ 0.04	=Fe K $\alpha$	1.72 $\pm$ 0.46	5.648 $\pm$ 0.03	=Fe K $\alpha$	1.45 $\pm$ 0.44
Mn K $\alpha$	6.07 $\pm$ 0.11	=Fe K $\alpha$	0.68 $\pm$ 0.27	6.03 $\pm$ 0.03	=Fe K $\alpha$	1.837 $\pm$ 0.3	5.938 $\pm$ -1	=Fe K $\alpha$	0.0 $\pm$ 0.0	6.067 $\pm$ 0.13	=Fe K $\alpha$	0.26 $\pm$ 0.29
Fe K $\alpha$	6.546 $\pm$ 0.006	94.3 $^{+6.2}_{-6.1}$	21.82 $\pm$ 0.91	6.546 $\pm$ 0.004	104.2 $\pm$ 3.7	23.6 $\pm$ 0.6	6.546 $\pm$ 0.006	96.3 $^{+6.6}_{-6.4}$	21.8 $\pm$ 0.9	6.545 $\pm$ 0.006	92.4 $^{+6.4}_{-6.3}$	21.64 $\pm$ 0.91
Fe K $\beta$	7.05 $^{+0.08}_{-7.0}$	=Fe K $\alpha$	0.82 $\pm$ 0.44	7.06 $\pm$ 0.06	=Fe K $\alpha$	1.8 $\pm$ 0.3	7.060 $\pm$ -1	=Fe K $\alpha$	0.0 $\pm$ 0.0	7.05 $^{+0.07}_{-7.1}$	=Fe K $\alpha$	0.85 $\pm$ 0.43
Ni K $\alpha$	7.8 $\pm$ 0.2	=Fe K $\alpha$	1.09 $\pm$ 0.33	7.8 $\pm$ 0.1	=Fe K $\alpha$	1.99 $\pm$ 0.34	7.80 $\pm$ 0.15	=Fe K $\alpha$	1.06 $\pm$ 0.34	7.8 $\pm$ 0.14	=Fe K $\alpha$	1.26 $\pm$ 0.34
Flux $\S$	5.44			5.40			5.40			5.41		
$\chi^2_{\nu}$ (d.o.f)	1.53 (338)			2.20 (338)			1.59 (336)			1.25 (336)		

$\diamond$  : The uncertainties are in the 90% confidence range.

\* : In unit of  $10^{21} \text{ cm}^{-2}$ .

$\dagger$  : In units of  $10^{-3} \text{ cm}^{-2} \text{ s}^{-1}$ .

$\ddagger$  : In units of  $10^{-6} \text{ cm}^{-2} \text{ s}^{-1}$ .

$\S$  : In units of  $10^{-12} \text{ erg cm}^{-2} \text{ s}^{-1}$  between 1.7–9.0 keV.

Flux of He $\gamma$  fixed to  $0.3 \times \text{He}\beta$ .

Flux of Ly $\beta$  fixed to  $\text{He}\beta/\text{He}\alpha \times \text{Ly}\alpha$ .

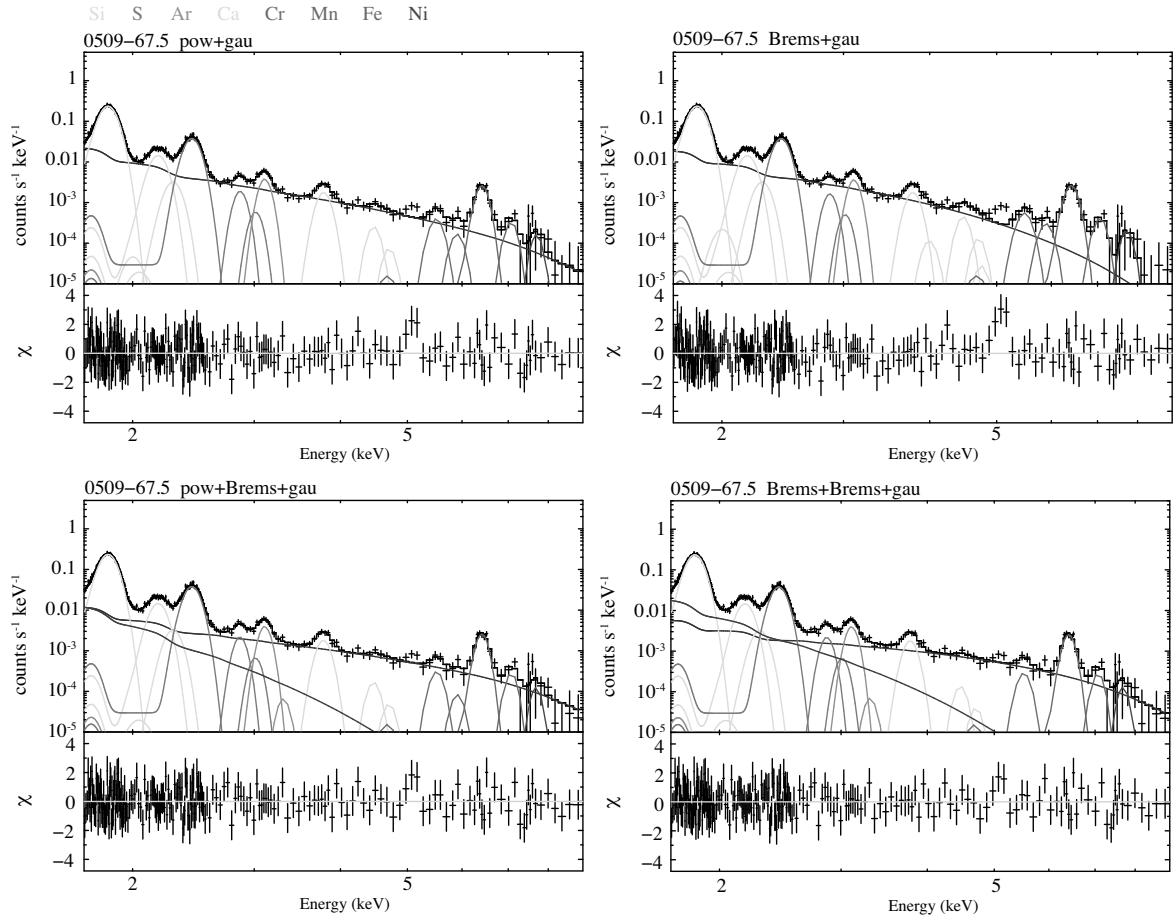


**Figure A.4:** The fitting results of SNR 0509–67.5 for four type models. The color lines represent the emission lines of each metal.

Table A.4: The best-fit parameters with multi-gaussians + continuum model in 0509–67.5 $^{\circ}$ .

Model	power-law			Brems.			power-law+Brems.			Brems.+Brems.		
	Centroid keV	Width eV	Norm $^{\dagger}$	Centroid keV	Width eV	Norm $^{\dagger}$	Centroid keV	Width eV	Norm $^{\dagger}$	Centroid keV	Width eV	Norm $^{\dagger}$
$\tau_{\text{H}}^{\text{C}^*}$	0.07 (fixed)	—	—	0.07 (fixed)	—	—	0.07 (fixed)	—	—	0.07 (fixed)	—	—
Continuum <sub>1</sub>	3.62 $^{+0.04}_{-0.03}$	—	—	1.25 $\pm 0.02$	—	—	2.89 $\pm 0.04$	—	—	3.63 $^{+0.25}_{-0.23}$	—	—
Norm $^{\dagger}$	0.62 $\pm 0.02$	—	—	0.47 $\pm 0.02$	—	—	0.22 $\pm 0.01$	—	—	0.074 $\pm 0.004$	—	—
Continuum <sub>2</sub>	—	—	—	—	—	—	0.48 $\pm 0.01$	—	—	0.55 $\pm 0.01$	—	—
Norm $^{\dagger}$	—	—	—	—	—	—	2.08 $\pm 0.2$	—	—	2.06 $\pm 0.12$	—	—
Line	Centroid keV	Width eV	Norm $^{\dagger}$	Centroid keV	Width eV	Norm $^{\dagger}$	Centroid keV	Width eV	Norm $^{\dagger}$	Centroid keV	Width eV	Norm $^{\dagger}$
Si He $\alpha$	1.8480 $\pm 0.0006$	20.7 $\pm 1.1$	175.5 $\pm 2.2$	1.8476 $^{+0.0006}_{-0.0005}$	22.4 $\pm 1.1$	175.4 $\pm 2.2$	1.8481 $^{+0.0006}_{-0.0005}$	20.1 $^{+1.1}_{-1.0}$	175.7 $\pm 2.2$	1.8481 $^{+0.0006}_{-0.0005}$	20.0 $^{+1.1}_{-1.0}$	175.6 $\pm 2.2$
Si Ly $\alpha$	=Si He $\beta$ –0.177	=Si He $\beta$	0.035 $^{+0.05}_{-0.035}$	=Si He $\beta$ –0.177	=Si He $\beta$	0.17 $^{+0.65}_{-0.17}$	=Si He $\beta$ –0.177	=Si He $\beta$	0.0 $\pm 0.0$	=Si He $\beta$ –0.177	=Si He $\beta$	0.0 $\pm 0.0$
Si He $\beta$	2.179 $\pm 0.006$	30 $^{+9}_{-10}$	10.47 $\pm 0.61$	2.1784 $\pm 0.0056$	31.0 $^{+9.1}_{-9.8}$	10.54 $\pm 0.62$	2.179 $^{+0.006}_{-0.005}$	30 $^{+9}_{-10}$	10.57 $\pm 0.61$	2.179 $^{+0.006}_{-0.005}$	29 $^{+9}_{-10}$	10.48 $\pm 0.61$
S He $\alpha$	2.438 $\pm 0.002$	31.3 $^{+3.5}_{-3.7}$	37.3 $\pm 1.1$	2.438 $\pm 0.002$	30.3 $^{+3.5}_{-3.7}$	36.9 $\pm 1.1$	2.438 $\pm 0.002$	32.4 $^{+3.4}_{-3.6}$	37.8 $\pm 1.1$	2.438 $\pm 0.002$	32.4 $^{+3.4}_{-3.6}$	37.7 $\pm 1.1$
S Ly $\alpha$	=S He $\beta$ –0.261	=S He $\beta$	0.0 $\pm 0.0$	=S He $\beta$ –0.261	=S He $\beta$	0.0 $\pm 0.0$	=S He $\beta$ –0.261	=S He $\beta$	0.0 $\pm 0.0$	=S He $\beta$ –0.261	=S He $\beta$	0.0 $\pm 0.0$
S He $\beta$	2.867 $\pm 0.02$	0.006 $\pm 0.571$	1.48 $\pm 0.35$	2.87 $\pm 0.02$	0.0002 $\pm 1$	1.27 $\pm 0.35$	2.86 $\pm 0.02$	0.0002 $\pm 1$	1.69 $\pm 0.35$	2.86 $\pm 0.02$	4.0e–5 $\pm 1$	1.69 $\pm 0.35$
Ar He $\alpha$	3.11 $\pm 0.01$	0.003 $\pm 1$	2.77 $\pm 0.38$	3.11 $\pm 0.01$	0.18 $^{+27}_{-0.18}$	2.65 $\pm 0.38$	3.120 $^{+0.010}_{-0.006}$	0.13 $^{+30}_{-0.13}$	2.90 $\pm 0.38$	3.11 $\pm 0.01$	1.2 $^{+29.0}_{-1.2}$	2.91 $\pm 0.38$
Ar Ly $\alpha$	=Ar He $\alpha$ +0.199	=Ar He $\alpha$	0.0 $\pm 0.0$	=Ar He $\alpha$ +0.199	=Ar He $\alpha$	0.0 $\pm 0.0$	=Ar He $\alpha$ +0.199	=Ar He $\alpha$	0.05 $^{+0.26}_{-0.05}$	=Ar He $\alpha$ +0.199	=Ar He $\alpha$	0.05 $^{+0.26}_{-0.05}$
Ar He $\beta$	=Ar He $\alpha$ +0.561	=Ar He $\alpha$	0.0 $\pm 0.0$	=Ar He $\alpha$ +0.561	=Ar He $\alpha$	0.0 $\pm 0.0$	=Ar He $\alpha$ +0.561	=Ar He $\alpha$	0.0 $\pm 0.0$	=Ar He $\alpha$ +0.561	=Ar He $\alpha$	0.0 $\pm 0.0$
Ca He $\alpha$	3.78 $\pm 0.02$	50 $^{+30}_{-38}$	1.6 $\pm 0.3$	3.78 $\pm 0.02$	54 $^{+31}_{-33}$	1.66 $\pm 0.31$	3.78 $\pm 0.02$	51 $^{+30}_{-35}$	1.6 $\pm 0.3$	3.78 $\pm 0.02$	49 $^{+30}_{-38}$	1.6 $\pm 0.3$
Ca Ly $\alpha$	=Ca He $\alpha$ +0.214	=Ca He $\alpha$	0.0 $\pm 0.0$	=Ca He $\alpha$ +0.214	=Ca He $\alpha$	0.1 $^{+0.2}_{-0.1}$	=Ca He $\alpha$ +0.214	=Ca He $\alpha$	0.0 $\pm 0.0$	=Ca He $\alpha$ +0.214	=Ca He $\alpha$	0.0 $\pm 0.0$
Ca He $\beta$	=Ca He $\alpha$ +0.690	=Ca He $\alpha$	0.2 $\pm 0.1$	=Ca He $\alpha$ +0.690	=Ca He $\alpha$	0.43 $\pm 0.19$	=Ca He $\alpha$ +0.690	=Ca He $\alpha$	0.16 $^{+0.19}_{-0.16}$	=Ca He $\alpha$ +0.214	=Ca He $\alpha$	0.13 $\pm 0.15$
Cr K $\alpha$	5.51 $\pm 0.07$	=Fe K $\alpha$	0.49 $\pm 0.23$	5.49 $\pm 0.06$	=Fe K $\alpha$	0.74 $\pm 0.23$	5.52 $\pm 0.08$	=Fe K $\alpha$	0.36 $\pm 0.22$	5.52 $\pm 0.08$	=Fe K $\alpha$	0.34 $\pm 0.22$
Mn K $\alpha$	5.909 (fixed)	=Fe K $\alpha$	0.218 (fixed)	5.899 (fixed)	=Fe K $\alpha$	0.428 (fixed)	5.915 (fixed)	=Fe K $\alpha$	0.104 (fixed)	5.9 (fixed)	=Fe K $\alpha$	0.0 (fixed)
Fe K $\alpha$	6.42 $^{+0.01}_{-0.02}$	84 $\pm 17$	3.62 $\pm 0.35$	6.42 $^{+0.01}_{-0.02}$	97 $\pm 16$	3.95 $\pm 0.36$	6.42 $^{+0.01}_{-0.02}$	77 $\pm 18$	3.43 $\pm 0.34$	6.42 $^{+0.01}_{-0.02}$	78 $\pm 18$	3.44 $\pm 0.34$
Fe K $\beta$	7.07 $^{+0.08}_{-7.10}$	=Fe K $\alpha$	0.61 $\pm 0.26$	7.06 $^{+0.07}_{-7.10}$	=Fe K $\alpha$	0.81 $\pm 0.26$	7.08 $^{+0.09}_{-7.10}$	=Fe K $\alpha$	0.49 $\pm 0.25$	7.08 $^{+0.08}_{-7.10}$	=Fe K $\alpha$	0.50 $\pm 0.25$
Ni K $\alpha$	7.707 (fixed)	=Fe K $\alpha$	0.362 (fixed)	7.731 (fixed)	=Fe K $\alpha$	0.507 (fixed)	7.692 (fixed)	=Fe K $\alpha$	0.263 (fixed)	7.696 (fixed)	=Fe K $\alpha$	0.281 (fixed)
Flux $^{\S}$	1.014	—	—	1.003	—	—	1.021	—	—	1.020	—	—
$\chi^2_{\nu}$ (d.o.f)	1.05(185)	—	—	1.17 (185)	—	—	1.03 (185)	—	—	1.03 (183)	—	—

$\diamond$  : The uncertainties are in the 90% confidence range.

\* : In unit of  $10^{21} \text{ cm}^{-2}$ .

$\dagger$  : In units of  $10^{-3} \text{ cm}^{-2} \text{ s}^{-1}$ .

$\ddagger$  : In units of  $10^{-6} \text{ cm}^{-2} \text{ s}^{-1}$ .

$\S$  : In units of  $10^{-12} \text{ erg cm}^{-2} \text{ s}^{-1}$  between 1.7–9.0 keV.

Flux of He $\gamma$  fixed to  $0.3 \times \text{He}\beta$ .

Flux of Ly $\beta$  fixed to  $\text{He}\beta/\text{He}\alpha \times \text{Ly}\alpha$ .

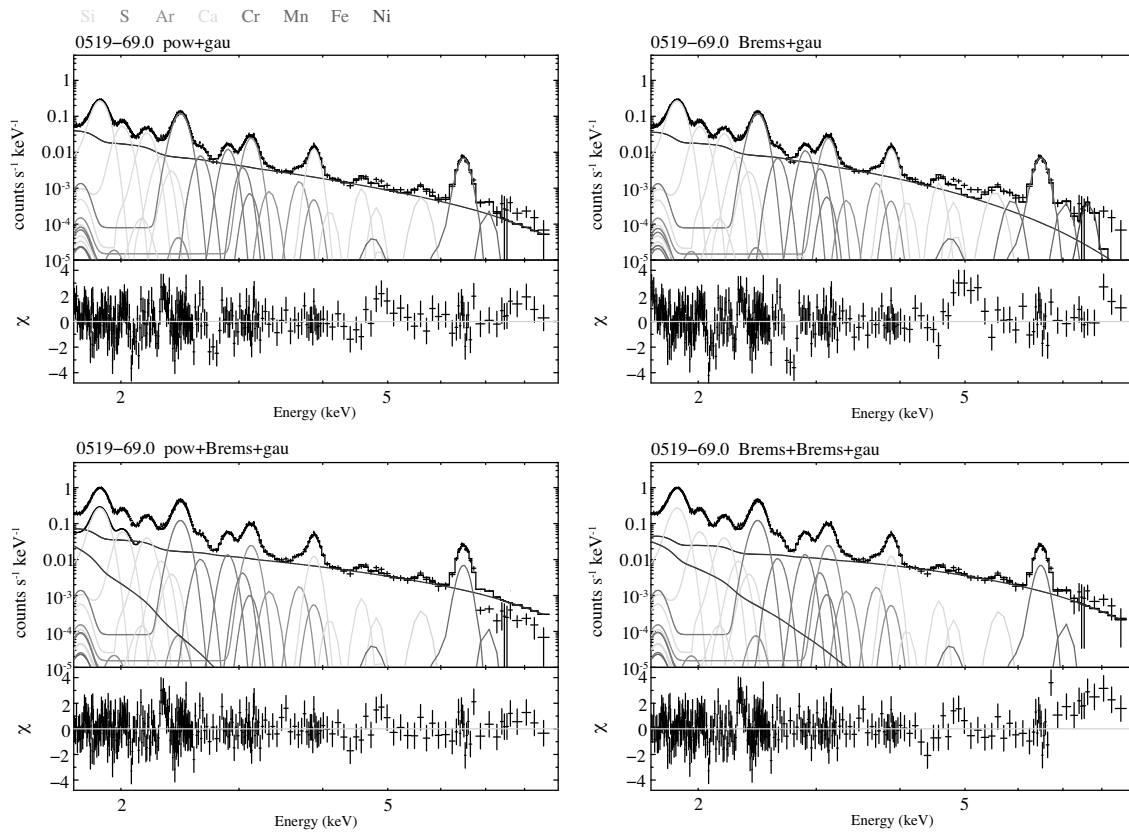


**Figure A.5:** The fitting results of SNR 0519-69.0 for four type models.

Table A.5: The best-fit parameters with multi-gaussians + continuum model in 0519-69.0°.

Model	power-law			Brems.			power-law+Brems.			Brems.+Brems.		
	Centroid keV	Width eV	Norm <sup>‡</sup>	Centroid keV	Width eV	Norm <sup>‡</sup>	Centroid keV	Width eV	Norm <sup>‡</sup>	Centroid keV	Width eV	Norm <sup>‡</sup>
$n_{\text{H}}^{\text{MC}^*}$	0.07 (fixed)			0.17 (fixed)			0.07 (fixed)			0.07 (fixed)		
Continuum <sub>1</sub>	3.59±0.024			1.23±0.014			2.87 <sup>+0.027</sup> <sub>-0.026</sub>			Brems.1: (keV) 3.001 <sup>+0.099</sup> <sub>-0.096</sub>		
Norm <sup>†</sup>	1.13±0.026			0.971±0.022			0.409±0.013			0.184±0.006		
Continuum <sub>2</sub>	—			—			0.153 <sup>+0.0012</sup> <sub>-0.0013</sub>			Brems.2: (keV) 0.232 <sup>+0.002</sup> <sub>-0.002</sub>		
Norm <sup>†</sup>	—			—			5700±33007			201±349		
Line	Centroid keV	Width eV	Norm <sup>‡</sup>	Centroid keV	Width eV	Norm <sup>‡</sup>	Centroid keV	Width eV	Norm <sup>‡</sup>	Centroid keV	Width eV	Norm <sup>‡</sup>
Si Heα	1.8602 <sup>+0.0005</sup> <sub>-0.0006</sub>	6.3 <sup>+1</sup> <sub>-2.5</sub>	258.6±3.3	1.8598 <sup>+0.0005</sup> <sub>-0.0005</sub>	7.97 <sup>+0.62</sup> <sub>-0.73</sub>	260.9±3.3	1.8603 <sup>+0.0006</sup> <sub>-0.0005</sub>	7.45 <sup>+0.72</sup> <sub>-0.94</sub>	259.2±3.2	1.8605 <sup>+0.0006</sup> <sub>-0.0005</sub>	6.44 <sup>+0.96</sup> <sub>-2.70</sub>	260.4±3.3
Si Lyα	=Si Heβ-0.177	=Si Heβ	31.5±1.1	=Si Heβ-0.177	=Si Heβ	31.4±1.1	=Si Heβ-0.177	=Si Heβ	35.4±1.1	=Si Heβ-0.177	=Si Heβ	35.2±1.1
Si Heβ	2.1860 <sup>+0.0048</sup> <sub>-0.0005</sub>	7.3e-4±-1	19.84±0.75	2.188 <sup>+0.001</sup> <sub>-0.004</sub>	3.1e-5±-1	19.2±0.8	2.1880 <sup>+0.0010</sup> <sub>-0.0009</sub>	0.029 <sup>+6</sup> <sub>-0.029</sub>	23.2±0.8	2.188 <sup>+0.001</sup> <sub>-0.002</sub>	0.012±-1	23.43±0.75
S Heα	2.4543 <sup>+0.0012</sup> <sub>-0.0009</sub>	18.1 <sup>+2.5</sup> <sub>-2.8</sub>	101.3±1.7	2.4545 <sup>+0.0011</sup> <sub>-0.0009</sub>	17.0 <sup>+2.6</sup> <sub>-3.0</sub>	101.0±1.7	2.4543 <sup>+0.0012</sup> <sub>-0.0009</sub>	19.5 <sup>+2.3</sup> <sub>-2.5</sub>	103.6±1.7	2.4542 <sup>+0.0012</sup> <sub>-0.0009</sub>	19.8 <sup>+2.3</sup> <sub>-2.5</sub>	104.1±1.7
S Lyα	=S Heβ-0.261	=S Heβ	5.6±0.6	=S Heβ-0.261	=S Heβ	4.9±0.6	=S Heβ-0.261	=S Heβ	7.2±0.6	=S Heβ-0.261	=S Heβ	7.6±0.6
S Heβ	2.893 <sup>+0.001</sup> <sub>-0.006</sub>	0.00-1.00	8.54±0.53	2.893 <sup>+0.003</sup> <sub>-0.005</sub>	8.5e-5±-1	7.89±0.53	2.891 <sup>+0.004</sup> <sub>-0.004</sub>	4.3e-4±-1	9.61±0.53	2.891 <sup>+0.003</sup> <sub>-0.004</sub>	2.5 <sup>+12</sup> <sub>-2.5</sub>	9.81±0.53
Ar Heα	3.131 <sup>+0.003</sup> <sub>-0.003</sub>	21.1 <sup>+6.1</sup> <sub>-7.7</sub>	18.23±0.73	3.131 <sup>+0.003</sup> <sub>-0.003</sub>	18.8 <sup>+6.6</sup> <sub>-9.2</sub>	17.98±0.74	3.131±0.003	24.1 <sup>+5.6</sup> <sub>-6.6</sub>	18.72±0.74	3.131±0.003	24.3 <sup>+5.6</sup> <sub>-6.5</sub>	18.78±0.74
Ar Lyα	=Ar Heα+0.199	=Ar Heα	0.60±0.33	=Ar Heα+0.199	=Ar Heα	0.34±0.33	=Ar Heα+0.199	=Ar Heα	0.99±0.25	=Ar Heα+0.199	=Ar Heα	1.00±0.45
Ar Heβ	=Ar Heα+0.561	=Ar Heα	1.1±0.3	=Ar Heα+0.561	=Ar Heα	1.0±0.3	=Ar Heα+0.561	=Ar Heα	1.3±0.3	=Ar Heα+0.561	=Ar Heα	1.3±0.3
Ca Heα	3.885 <sup>+0.004</sup> <sub>-0.004</sub>	14 <sup>+12</sup> <sub>-14</sub>	8.31±0.46	3.885 <sup>+0.004</sup> <sub>-0.004</sub>	17 <sup>+11</sup> <sub>-17</sub>	8.41±0.47	3.885 <sup>+0.004</sup> <sub>-0.004</sub>	13±13	8.31±0.46	3.885 <sup>+0.004</sup> <sub>-0.004</sub>	12 <sup>+13</sup> <sub>-12</sub>	8.25±0.46
Ca Lyα	=Ca Heα+0.214	=Ca Heα	0.17 <sup>+0.23</sup> <sub>-0.17</sub>	=Ca Heα+0.214	=Ca Heα	0.31±0.23	=Ca Heα+0.214	=Ca Heα	0.15 <sup>+0.23</sup> <sub>-0.15</sub>	=Ca Heα+0.214	=Ca Heα	0.08 <sup>+0.23</sup> <sub>-0.08</sub>
Ca Heβ	=Ca Heα+0.690	=Ca Heα	0.72±0.21	=Ca Heα+0.690	=Ca Heα	1.02±0.21	=Ca Heα+0.690	=Ca Heα	0.60±0.21	=Ca Heα+0.690	=Ca Heα	0.51±0.21
Cr Kα	5.620 <sup>+0.061</sup> <sub>-0.059</sub>	=Fe Kα	0.70±0.24	5.551±0.049	=Fe Kα	1.02±0.24	5.622 <sup>+0.078</sup> <sub>-0.073</sub>	=Fe Kα	0.44±0.23	5.63 <sup>+0.08</sup> <sub>-0.08</sub>	=Fe Kα	0.43±0.24
Mn Kα	6.00 (fixed)	=Fe Kα	0.0 (fixed)	5.884 (fixed)	=Fe Kα	0.63 (fixed)	6.00 (fixed)	=Fe Kα	0.0 (fixed)	6.0 (fixed)	=Fe Kα	0.0 (fixed)
Fe Kα	6.493 <sup>+0.006</sup> <sub>-0.008</sub>	86.3 <sup>+8.2</sup> <sub>-8.1</sub>	9.55±0.48	6.493 <sup>+0.007</sup> <sub>-0.007</sub>	96.3 <sup>+7.9</sup> <sub>-7.7</sub>	10.17±0.49	6.493 <sup>+0.006</sup> <sub>-0.008</sub>	80.6±8.3	9.18±0.48	6.493 <sup>+0.006</sup> <sub>-0.008</sub>	81.7±8.3	9.25±0.48
Fe Kβ	7.06 <sup>+0.13</sup> <sub>-0.13</sub>	=Fe Kα	0.43±0.25	7.061 <sup>+0.088</sup> <sub>-0.088</sub>	=Fe Kα	0.75±0.25	7.06 ±0.30	=Fe Kα	0.21±0.16	7.06 <sup>+0.16</sup> <sub>-0.16</sub>	=Fe Kα	0.29±0.24
Ni Kα	7.60 (fixed)	=Fe Kα	0.0 (fixed)	7.646 (fixed)	=Fe Kα	0.86 (fixed)	7.8 (fixed)	=Fe Kα	1.062 (fixed)	7.6 (fixed)	=Fe Kα	0.0 (fixed)
Flux <sup>§</sup>	2.1172			2.1027			2.1191			2.1209		
$\chi^2_{\nu}(\text{d.o.f})$	1.41 (252)			1.71 (252)			1.22 (250)			1.25 (250)		

◇ : The uncertainties are in the 90% confidence range.

\* : In unit of  $10^{21} \text{ cm}^{-2}$ .

† : In units of  $10^{-3} \text{ cm}^{-2} \text{ s}^{-1}$ .

‡ : In units of  $10^{-6} \text{ cm}^{-2} \text{ s}^{-1}$ .

§ : In units of  $10^{-12} \text{ erg cm}^{-2} \text{ s}^{-1}$  between 1.7–9.0 keV.

Flux of Heγ fixed to  $0.3 \times \text{He}\beta$ .

Flux of Lyβ fixed to  $\text{He}\beta/\text{He}\alpha \times \text{Ly}\alpha$ .

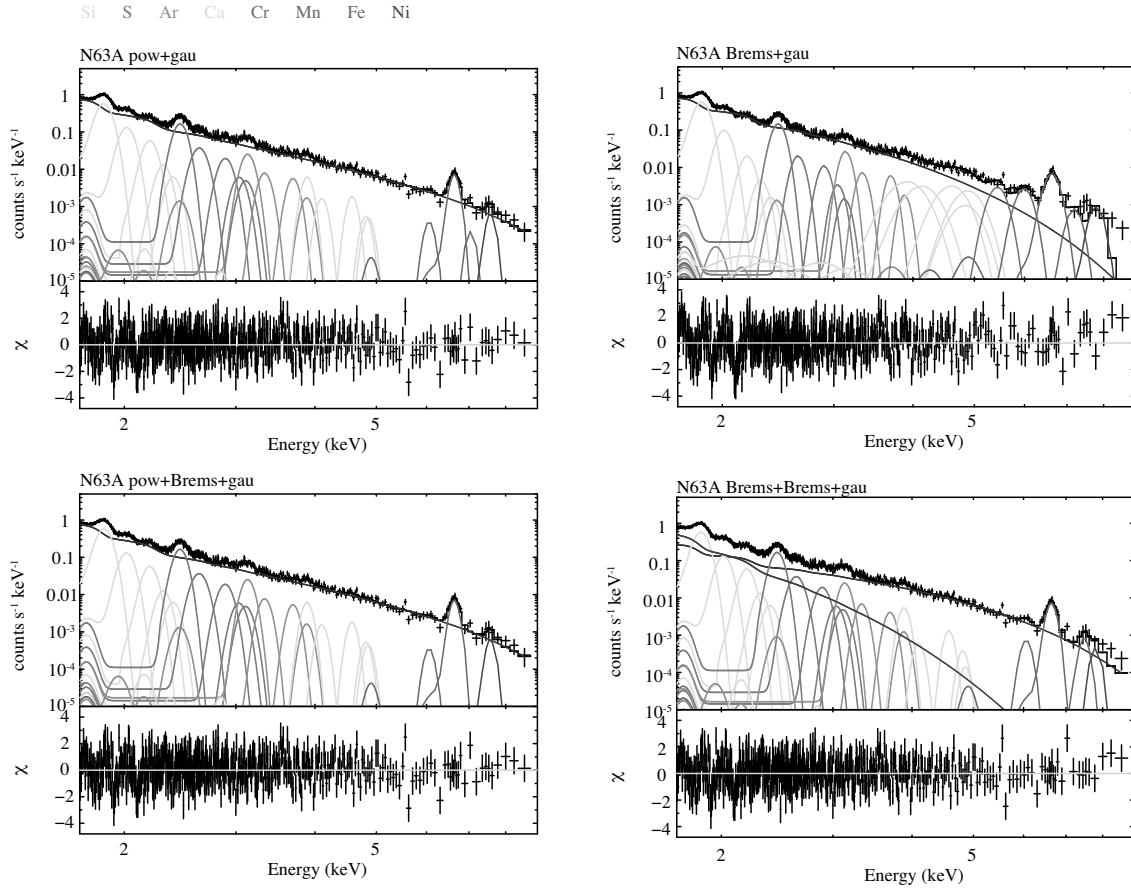


**Figure A.6:** The fitting results of SNR N63A for 4 type models.

Table A.6: The best-fit parameters with multi-gaussians + continuum model in N63A<sup>◇</sup>.

Model	power-law			Brems.			power-law+Brems.			Brems.+Brems.		
	Centroid keV	Width eV	Norm <sup>†</sup>	Centroid keV	Width eV	Norm <sup>†</sup>	Centroid keV	Width eV	Norm <sup>†</sup>	Centroid keV	Width eV	Norm <sup>†</sup>
$N^{\text{H}}C^*$	0.17 (fixed)			0.17 (fixed)			0.17 (fixed)			0.17 (fixed)		
Continuum <sub>1</sub>	1.8571 <sup>+0.0010</sup> <sub>-0.0009</sub>	1.4 <sup>+1.2</sup> <sub>-1.4</sub>	579±14	1.8558 <sup>+0.0002</sup> <sub>-0.002</sub>	0.19 <sup>+2.4</sup> <sub>-0.19</sub>	585±14	1.8574 <sup>+0.0009</sup> <sub>-0.001</sub>	0.88 <sup>+1.4</sup> <sub>-0.88</sub>	572±13	1.8570 <sup>+0.0008</sup> <sub>-0.001</sub>	2.3 <sup>+1.3</sup> <sub>-1.1</sub>	592±14
Norm <sup>†</sup>	4.52±0.01	=Si Heβ	87.0±5.8	=Si Heβ-0.177	=Si Heβ	64.7±5.8	=Si Heβ-0.177	=Si Heβ	86.3±5.8	=Si Heβ-0.177	=Si Heβ	87.3±5.8
Continuum <sub>2</sub>	35.1±0.3	7.8e-5±-1	36.2±3.7	2.191 <sup>+0.002</sup> <sub>-0.008</sub>	0.004±-1	12.7±3.8	2.195 <sup>+0.002</sup> <sub>-0.005</sub>	7.2e-5±-1	35.7±3.7	2.195 <sup>+0.001</sup> <sub>-0.006</sub>	0.13±-1	36.9±3.7
Norm <sup>†</sup>	—	—	140.3±5.5	2.452 <sup>+0.004</sup> <sub>-0.002</sub>	0.003 <sup>+12</sup> <sub>-0.003</sub>	124.0±5.5	2.451±0.003	4.0 <sup>+10</sup> <sub>-3.9</sub>	139.1±5.5	2.451±0.003	5.6 <sup>+9.8</sup> <sub>-5.9</sub>	141.2±5.5
Line	=S Heβ	=S Heβ	33.7±3.7	=S Heβ-0.261	=S Heβ	15.5±3.4	=S Heβ-0.261	=S Heβ	34.0±3.8	=S Heβ-0.261	=S Heβ	34.3±3.7
Si Heα	2.889 <sup>+0.009</sup> <sub>-0.010</sub>	34 <sup>+14</sup> <sub>-17</sub>	17.4±2.3	2.90±0.02	0.0005±-1	8.4±2.3	2.89±0.01	36 <sup>+14</sup> <sub>-15</sub>	17.2±2.3	2.89±0.01	35 <sup>+14</sup> <sub>-16</sub>	17.2±2.3
Si Lyα	3.13±0.01	27 <sup>+21</sup> <sub>-27</sub>	20.8±2.6	3.13±0.01	0.0001±-1	20.1±2.5	3.13±0.01	25 <sup>+21</sup> <sub>-25</sub>	20.6±2.6	3.13±0.01	20 <sup>+22</sup> <sub>-20</sub>	19.8±2.6
S Heβ	=Ar Heα+0.199	=Ar Heα	6.3±1.9	=Ar Heα+0.199	=Ar Heα	5.2±1.9	=Ar Heα+0.199	=Ar Heα	6.2±1.9	=Ar Heα+0.199	=Ar Heα	5.3±1.9
Ar Heα	=Ar Heα+0.561	=Ar Heα	4.4±1.4	=Ar Heα+0.561	=Ar Heα	4.3±1.3	=Ar Heα+0.561	=Ar Heα	4.1±1.4	=Ar Heα+0.561	=Ar Heα	3.1±1.4
Ca Heα	3.89 <sup>+0.02</sup> <sub>-0.03</sub>	0.43±61	4.3 <sup>+1.4</sup> <sub>-1.3</sub>	3.91±0.19	200±56	9.2 <sup>+1.8</sup> <sub>-1.6</sub>	3.89±0.03	0.007±-1	4.4±1.4	3.89±0.03	3.7 <sup>+52</sup> <sub>-3.6</sub>	3.9±1.4
Ca Lyα	=Ca Heα+0.214	=Ca Heα	1.22±0.75	=Ca Heα+0.214	=Ca Heα	6.8±1.3	=Ca Heα+0.214	=Ca Heα	1.06±0.75	=Ca Heα+0.214	=Ca Heα	0.4 <sup>+1.1</sup> <sub>-0.4</sub>
Ca Heβ	=Ca Heα+0.690	=Ca Heα	1.38±0.76	=Ca Heα+0.690	=Ca Heα	6.75±0.76	=Ca Heα+0.690	=Ca Heα	1.35±0.77	=Ca Heα+0.690	=Ca Heα	0.96±0.83
Cr Kα	5.442±-1	=Fe Kα	0.0±0.0	5.44 <sup>+0.05</sup> <sub>-5.4</sub>	=Fe Kα	4.41±0.87	5.500±-1	=Fe Kα	0.0±0.0	5.43±-1	=Fe Kα	0.0±-1
Mn Kα	6.062±0.174	=Fe Kα	0.40±0.41	6.00±0.03	=Fe Kα	4.31±0.52	6.06±0.222	=Fe Kα	0.37±0.41	6.06±0.10	=Fe Kα	0.83±0.47
Fe Kα	6.64±0.02	33 <sup>+28</sup> <sub>-33</sub>	8.0±0.7	6.64±0.02	124 <sup>+15</sup> <sub>-14</sub>	12.1±1.1	6.64±0.01	38 <sup>+27</sup> <sub>-38</sub>	8.12±0.68	6.64±0.01	56 <sup>+23</sup> <sub>-28</sub>	9.01±0.74
Fe Kβ	7.1±0.4	=Fe Kα	0.3 <sup>+0.7</sup> <sub>-0.3</sub>	7.2 <sup>+0.2</sup> <sub>-0.1</sub>	=Fe Kα	1.8±0.8	7.06±-1	=Fe Kα	0.0±0.0	7.52±0.09	=Fe Kα	1.8±1.1
Ni Kα	7.58±0.09	=Fe Kα	1.07±0.60	7.68±0.06	=Fe Kα	2.66±0.67	7.574±0.087	=Fe Kα	1.07±0.60	7.80±0.52	=Fe Kα	0.82±0.91
Flux <sup>§</sup>	8.7561			8.7676			8.7378			8.7714		
$\chi^2_p$ (d.o.f)	1.13 (471)			1.34 (471)			1.14 (469)			1.13 (469)		

◇ : The uncertainties are in the 90% confidence range.

\* : In unit of  $10^{21} \text{ cm}^{-2}$ .

† : In units of  $10^{-3} \text{ cm}^{-2} \text{ s}^{-1}$ .

‡ : In units of  $10^{-6} \text{ cm}^{-2} \text{ s}^{-1}$ .

§ : In units of  $10^{-12} \text{ erg cm}^{-2} \text{ s}^{-1}$  between 1.7–9.0 keV.

Flux of Heγ fixed to  $0.3 \times \text{He}\beta$ .

Flux of Lyβ fixed to  $\text{He}\beta/\text{He}\alpha \times \text{Ly}\alpha$ .

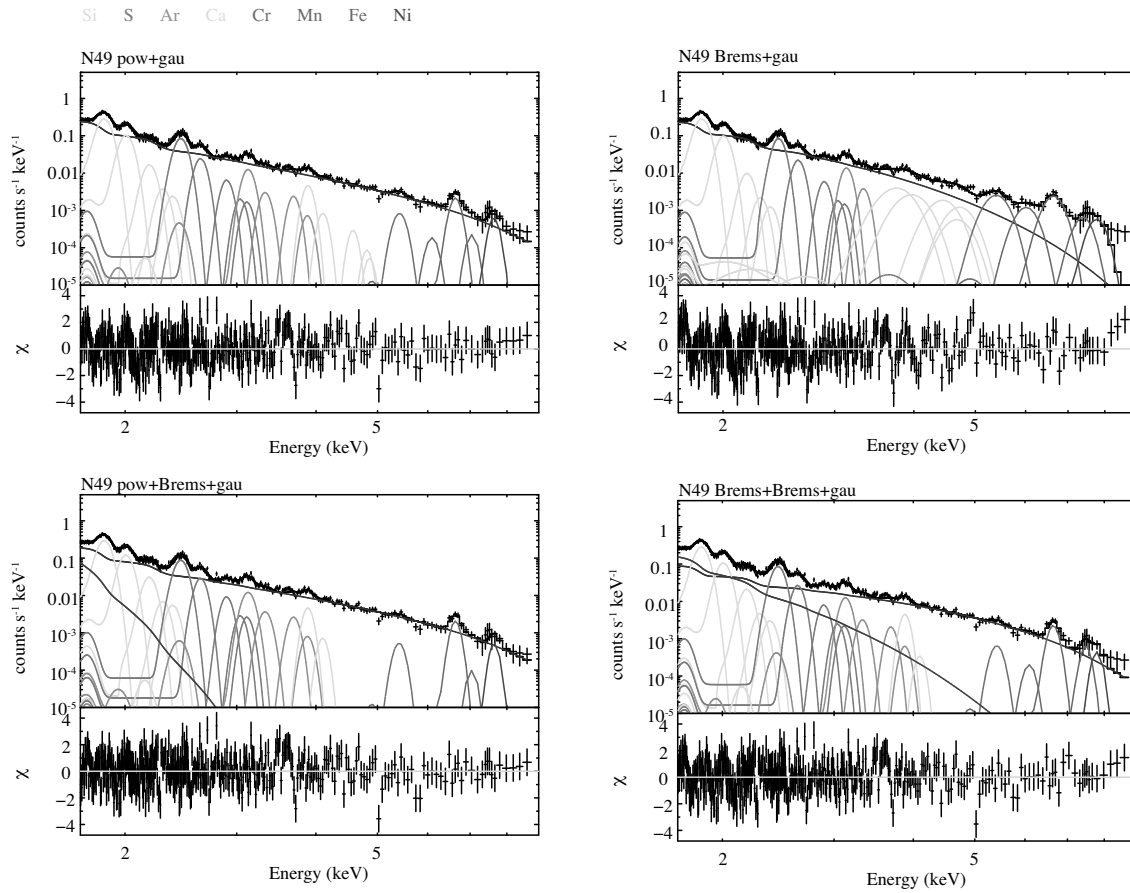


**Figure A.7:** The fitting results of SNR N49 for 4 type models.

Table A.7: The best-fit parameters with multi-gaussians + continuum model in N49°.

Model	power-law			Brems.			power-law+Brems.			Brems.+Brems.			
	Centroid keV	Width eV	Norm <sup>†</sup>	Centroid keV	Width eV	Norm <sup>†</sup>	power-law: $\Gamma$	Centroid keV	Width eV	Norm <sup>†</sup>	Centroid keV	Width eV	Norm <sup>†</sup>
$N_{\text{H}}^{\text{MC}^*}$	0.22 (fixed)			0.22 (fixed)				0.22 (fixed)				0.22 (fixed)	
Continuum <sub>1</sub>	4.04±0.01			0.883±0.004			3.74±0.01						1.84±0.02
Norm <sup>†</sup>	8.86±0.09			9.8±0.1			5.82±0.07						1.59±0.03
Continuum <sub>2</sub>	—			—			0.1340 <sup>+0.0008</sup> <sub>-0.0009</sub>						0.440±0.002
Norm <sup>†</sup>	—			—			75800±346806						37.7±0.9
Line	Centroid keV	Width eV	Norm <sup>†</sup>	Centroid keV	Width eV	Norm <sup>†</sup>	Centroid keV	Width eV	Norm <sup>†</sup>	Centroid keV	Width eV	Norm <sup>†</sup>	
Si He $\alpha$	1.854	0.3 <sup>+1.3</sup> <sub>-0.2</sub>	310.7±6.6	1.8524 <sup>+0.0004</sup> <sub>-0.0006</sub>	0.78 <sup>+0.93</sup> <sub>-0.55</sub>	333.6±7.1	1.8544 <sup>+0.0013</sup> <sub>-0.0005</sub>	0.26 <sup>+0.41</sup> <sub>-0.12</sub>	294±6	1.854±0.022	0.05 <sup>+0.04</sup> <sub>-0.05</sub>	326.9±6.9	
Si Ly $\alpha$	=Si He $\beta$ -0.177	=Si He $\beta$	63.1±2.6	=Si He $\beta$ -0.177	=Si He $\beta$	59.7±2.6	=Si He $\beta$ -0.177	=Si He $\beta$	73.9±2.6	=Si He $\beta$ -0.177	=Si He $\beta$	65.8±2.6	
Si He $\beta$	2.1841 <sup>+0.0009</sup> <sub>-0.0004</sub>	0.018±-1	9.8±1.5	2.1824 <sup>+0.0009</sup> <sub>-0.0030</sub>	0.021±-1	5.8±1.5	2.185 <sup>+0.003</sup> <sub>-0.001</sub>	0.001±-1	18.2±1.5	2.185 <sup>+0.001</sup> <sub>-0.003</sub>	0.024±-1	12.5±1.5	
S He $\alpha$	2.449±0.002	17.4 <sup>+5.5</sup> <sub>-7.1</sub>	71.6±2.5	2.448±0.003	0.003±-1	67.4±2.4	2.450±0.002	22.0 <sup>+4.7</sup> <sub>-5.4</sub>	76.6±2.5	2.449 <sup>+0.003</sup> <sub>-0.002</sub>	19.8 <sup>+5.1</sup> <sub>-6.1</sub>	74.3±2.5	
S Ly $\alpha$	=S He $\beta$ -0.261	=S He $\beta$	17.8±1.6	=S He $\beta$ -0.261	=S He $\beta$	16.1±1.6	=S He $\beta$ -0.261	=S He $\beta$	21.1±1.5	=S He $\beta$ -0.261	=S He $\beta$	19.5±1.6	
S He $\beta$	2.893 <sup>+0.003</sup> <sub>-0.008</sub>	0.04±-1	4.66±0.96	2.891±0.002	0.0004±-1	4.25±0.96	2.893 <sup>+0.004</sup> <sub>-0.007</sub>	2.9 <sup>+1.4</sup> <sub>-1.4</sub>	6.64±0.95	2.893 <sup>+0.004</sup> <sub>-0.006</sub>	2.87±51.2	5.77±0.96	
Ar He $\alpha$	3.13±0.01	22 <sup>+20</sup> <sub>-22</sub>	9.5±1.2	3.134 <sup>+0.009</sup> <sub>-0.010</sub>	19±19	10.3±1.1	3.129±0.011	35 <sup>+19</sup> <sub>-22</sub>	10.0±1.2	3.13±0.01	24 <sup>+19</sup> <sub>-24</sub>	9.6±1.2	
Ar Ly $\alpha$	=Ar He $\alpha$ +0.199	=Ar He $\alpha$	2.25±0.87	=Ar He $\alpha$ +0.199	=Ar He $\alpha$	2.78±0.86	=Ar He $\alpha$ +0.199	=Ar He $\alpha$	2.9±0.9	=Ar He $\alpha$ +0.199	=Ar He $\alpha$	2.39±0.87	
Ar He $\beta$	=Ar He $\alpha$ +0.561	=Ar He $\alpha$	1.72±0.65	=Ar He $\alpha$ +0.561	=Ar He $\alpha$	0.0±0.0	=Ar He $\alpha$ +0.561	=Ar He $\alpha$	2.05±0.66	=Ar He $\alpha$ +0.561	=Ar He $\alpha$	1.51±0.65	
Ca He $\alpha$	3.89±0.02	20 <sup>+32</sup> <sub>-20</sub>	3.3±0.7	3.75±0.03	200±45	9.0 <sup>+1.2</sup> <sub>-1.1</sub>	3.89±0.02	13 <sup>+36</sup> <sub>-13</sub>	3.16±0.69	3.88±0.02	11 <sup>+36</sup> <sub>-11</sub>	3.05±0.69	
Ca Ly $\alpha$	=Ca He $\alpha$ +0.214	=Ca He $\alpha$	0.59±0.56	=Ca He $\alpha$ +0.214	=Ca He $\alpha$	5.80±0.91	=Ca He $\alpha$ +0.214	=Ca He $\alpha$	0.49 <sup>+0.55</sup> <sub>-0.49</sub>	=Ca He $\alpha$ +0.214	=Ca He $\alpha$	0.24 <sup>+0.55</sup> <sub>-0.24</sub>	
Ca He $\beta$	=Ca He $\alpha$ +0.690	=Ca He $\alpha$	0.22±0.41	=Ca He $\alpha$ +0.690	=Ca He $\alpha$	3.95±0.45	=Ca He $\alpha$ +0.690	=Ca He $\alpha$	0.0±0.0	=Ca He $\alpha$ +0.690	=Ca He $\alpha$	0.0±0.0	
Cr K $\alpha$	5.42 <sup>+0.08</sup> <sub>-5.4</sub>	=Fe K $\alpha$	0.96±0.49	5.40 <sup>+0.02</sup> <sub>-5.4</sub>	=Fe K $\alpha$	5.37±0.65	5.4 <sup>+0.1</sup> <sub>-5.4</sub>	=Fe K $\alpha$	0.54±0.46	5.42 <sup>+0.12</sup> <sub>-5.4</sub>	=Fe K $\alpha$	0.75±0.55	
Mn K $\alpha$	6.10±0.45	=Fe K $\alpha$	0.22±0.30	6.02±0.06	=Fe K $\alpha$	2.73±0.43	6.00±0.00	=Fe K $\alpha$	0.0±0.0	6.10±0.31	=Fe K $\alpha$	0.45±0.44	
Fe K $\alpha$	6.64±0.03	83 <sup>+32</sup> <sub>-30</sub>	3.03±0.54	6.66±0.03	196.598	6.13±0.67	6.64±0.03	66 <sup>+37</sup> <sub>-44</sub>	2.61±0.51	6.66±0.04	84 <sup>+36</sup> <sub>-35</sub>	3.19±0.54	
Fe K $\beta$	7.05 <sup>+0.52</sup> <sub>-7.00</sub>	=Fe K $\alpha$	0.38±0.44	7.40±0.11	=Fe K $\alpha$	2.10±0.86	7.05±0.66	=Fe K $\alpha$	0.15 <sup>+0.41</sup> <sub>-0.15</sub>	7.49 <sup>+0.1</sup> <sub>-0.11</sub>	=Fe K $\alpha$	1.18±0.82	
Ni K $\alpha$	7.63±0.06	=Fe K $\alpha$	1.36±0.47	7.80±0.40	=Fe K $\alpha$	2.23±1.66	7.65±0.03	=Fe K $\alpha$	0.96±0.43	7.79±0.39	=Fe K $\alpha$	1.13±1.12	
Flux <sup>§</sup>	3.8199			3.8724								3.8552	
$\chi^2_{\nu}$ (d.o.f)	1.39 (356)			1.59 (356)								1.36 (354)	

◊ : The uncertainties are in the 90% confidence range.

\* : In unit of  $10^{21} \text{ cm}^{-2}$ .

† : In units of  $10^{-3} \text{ cm}^{-2} \text{ s}^{-1}$ .

‡ : In units of  $10^{-6} \text{ cm}^{-2} \text{ s}^{-1}$ .

§ : In units of  $10^{-12} \text{ erg cm}^{-2} \text{ s}^{-1}$  between 1.7–9.0 keV.

Flux of He $\gamma$  fixed to  $0.3 \times \text{He}\beta$ .

Flux of Ly $\beta$  fixed to He $\beta$ /He $\alpha \times \text{Ly}\alpha$ .

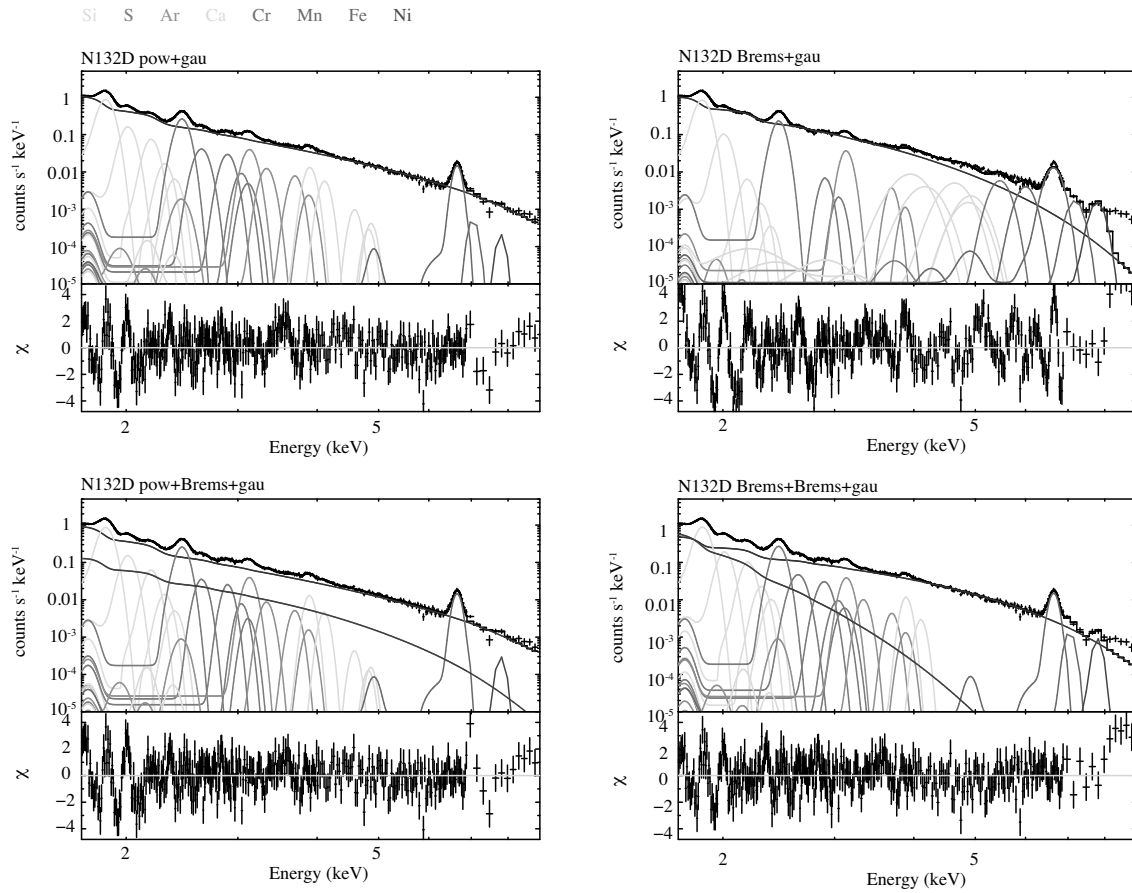


**Figure A.8:** The fitting results of SNR N132D for 4 type models.

Table A.8: The best-fit parameters with multi-gaussians + continuum model in N132D $^{\diamond}$ .

Model	power-law			Brems.			power-law+Brems.			Brems.+Brems.		
$N_{\text{H}}^{\text{MC}^*}$	0.13 (fixed)			0.36 (fixed)			0.13 (fixed)			0.13 (fixed)		
Continuum $_1$	4.12 $\pm$ 0.12			0.935 $\pm$ 0.007			power-law: $\Gamma$	4.080 $\pm$ 0.005		Brems.1: (keV)	1.550 $\pm$ 0.005	
Norm $^{\ddagger}$	39.8 $\pm$ 0.2			41.0 $\pm$ 0.7			Brems.: (keV)	33.9 $\pm$ 0.2		Brems.2: (keV)	9.99 $\pm$ 0.06	
Continuum $_2$	—			—				1.07 $\pm$ 0.01		0.3400 $\pm$ 0.0008		
Norm $^{\ddagger}$	—			—				4.1 $\pm$ 0.1		410 $\pm$ 5		
Line	Centroid	Width	Norm $^{\ddagger}$	Centroid	Width	Norm $^{\ddagger}$	Centroid	Width	Norm $^{\ddagger}$	Centroid	Width	Norm $^{\ddagger}$
	keV	eV		keV	eV		keV	eV		keV	eV	
Si He $\alpha$	1.8480 $\pm$ 0.0006	20.7 $\pm$ 1.1	175.5 $\pm$ 2.2	1.8476 $^{+0.0006}_{-0.0005}$	22.1 $\pm$ 1.1	175.4 $\pm$ 2.2	1.8481 $^{+0.0006}_{-0.0005}$	20.1 $^{+1.1}_{-1.0}$	175.7 $\pm$ 2.2	1.8481 $^{+0.0006}_{-0.0005}$	20.0 $^{+1.1}_{-1.0}$	175.6 $\pm$ 2.2
Si Ly $\alpha$	=Si He $\beta$ -0.177	=Si He $\beta$	0.035 $^{+0.65}_{-0.035}$	=Si He $\beta$ -0.177	=Si He $\beta$	0.17 $^{+0.65}_{-0.17}$	=Si He $\beta$ -0.177	=Si He $\beta$	96.0 $\pm$ 4.1	=Si He $\beta$ -0.177	=Si He $\beta$	12.1 $\pm$ 5.1
Si He $\beta$	2.179 $\pm$ 0.006	30 $^{+9}_{-10}$	10.47 $\pm$ 0.61	2.1784 $\pm$ 0.0056	31.0 $^{+9.1}_{-9.8}$	10.54 $\pm$ 0.62	2.179 $^{+0.006}_{-0.005}$	30 $^{+9}_{-10}$	10.57 $\pm$ 0.61	2.179 $^{+0.006}_{-0.005}$	29 $^{+9}_{-10}$	10.48 $\pm$ 0.61
S He $\alpha$	2.438 $\pm$ 0.002	31.3 $^{+3.5}_{-3.7}$	226.2 $\pm$ 3.3	2.438 $\pm$ 0.002	30.3 $^{+3.5}_{-3.7}$	36.9 $\pm$ 1.1	2.438 $\pm$ 0.002	32.4 $^{+3.4}_{-3.6}$	37.8 $\pm$ 1.1	2.438 $\pm$ 0.002	32.4 $^{+3.4}_{-3.6}$	37.7 $\pm$ 1.1
S Ly $\alpha$	=S He $\beta$ -0.261	=S He $\beta$	36.2 $\pm$ 2.4	=S He $\beta$ -0.261	=S He $\beta$	0.0 $\pm$ 0.0	=S He $\beta$ -0.261	=S He $\beta$	26.2 $\pm$ 2.8	=S He $\beta$ -0.261	=S He $\beta$	44.6 $\pm$ 3.7
S He $\beta$	2.867 $\pm$ 0.007	32.4 $\pm$ 5.8	25.4 $\pm$ 1.5	2.87 $\pm$ 0.02	0.029 $\pm$ 1	1.27 $\pm$ 0.35	2.86 $\pm$ 0.02	3.2 $\pm$ 41.6	1.69 $\pm$ 0.35	2.86 $\pm$ 0.02	41.2 $\pm$ 5.2	1.69 $\pm$ 0.35
Ar He $\alpha$	3.11 $\pm$ 0.01	37.6 $\pm$ 6.0	2.77 $\pm$ 0.38	3.11 $\pm$ 0.01	0.18 $^{+27}_{-0.18}$	2.65 $\pm$ 0.38	3.120 $^{+0.010}_{-0.006}$	0.13 $^{+30}_{-0.13}$	2.90 $\pm$ 0.38	3.11 $\pm$ 0.01	1.2 $^{+29.0}_{-1.2}$	2.91 $\pm$ 0.38
Ar Ly $\alpha$	=Ar He $\alpha$ +0.199	=Ar He $\alpha$	10.5 $\pm$ 1.1	=Ar He $\alpha$ +0.199	=Ar He $\alpha$	0.0 $\pm$ 0.0	=Ar He $\alpha$ +0.199	=Ar He $\alpha$	0.05 $^{+0.26}_{-0.05}$	=Ar He $\alpha$ +0.199	=Ar He $\alpha$	0.05 $^{+0.26}_{-0.05}$
Ar He $\beta$	=Ar He $\alpha$ +0.561	=Ar He $\alpha$	6.35 $\pm$ 0.92	=Ar He $\alpha$ +0.561	=Ar He $\alpha$	2.63 $\pm$ 1.14	=Ar He $\alpha$ +0.561	=Ar He $\alpha$	3.85 $\pm$ 0.96	=Ar He $\alpha$ +0.561	=Ar He $\alpha$	3.25 $\pm$ 1.07
Ca He $\alpha$	3.78 $\pm$ 0.02	50 $^{+30}_{-38}$	1.6 $\pm$ 0.3	3.78 $\pm$ 0.02	54 $^{+31}_{-33}$	1.66 $\pm$ 0.31	3.78 $\pm$ 0.02	51 $^{+30}_{-35}$	1.6 $\pm$ 0.3	3.78 $\pm$ 0.02	49 $^{+30}_{-38}$	1.6 $\pm$ 0.3
Ca Ly $\alpha$	=Ca He $\alpha$ +0.214	=Ca He $\alpha$	4.38 $\pm$ 0.67	=Ca He $\alpha$ +0.214	=Ca He $\alpha$	0.1 $^{+0.2}_{-0.1}$	=Ca He $\alpha$ +0.214	=Ca He $\alpha$	3.22 $\pm$ 0.69	=Ca He $\alpha$ +0.214	=Ca He $\alpha$	2.00 $\pm$ 0.68
Ca He $\beta$	=Ca He $\alpha$ +0.690	=Ca He $\alpha$	0.8 $\pm$ 0.4	=Ca He $\alpha$ +0.690	=Ca He $\alpha$	0.43 $\pm$ 0.19	=Ca He $\alpha$ +0.690	=Ca He $\alpha$	0.16 $^{+0.19}_{-0.16}$	=Ca He $\alpha$ +0.214	=Ca He $\alpha$	0.0 $\pm$ 0.0
Cr K $\alpha$	5.40 $\pm$ 1	=Fe K $\alpha$	0.0 $\pm$ 0.0	5.49 $\pm$ 0.06	=Fe K $\alpha$	0.74 $\pm$ 0.23	5.52 $\pm$ 0.08	=Fe K $\alpha$	0.36 $\pm$ 0.22	5.52 $\pm$ 0.08	=Fe K $\alpha$	0.34 $\pm$ 0.22
Mn K $\alpha$	6.00 $\pm$ 0.0	=Fe K $\alpha$	0.0 $\pm$ 0.0	6.01 $\pm$ 0.02	=Fe K $\alpha$	7.11 $\pm$ 0.44	6.10 $\pm$ 1	=Fe K $\alpha$	0.0 $\pm$ 0.0	6.00 $\pm$ 1	=Fe K $\alpha$	0.0 $\pm$ 0.0
Fe K $\alpha$	6.42 $^{+0.01}_{-0.02}$	84 $\pm$ 17	3.62 $\pm$ 0.35	6.42 $^{+0.01}_{-0.02}$	97 $\pm$ 16	3.95 $\pm$ 0.36	6.42 $^{+0.01}_{-0.02}$	77 $\pm$ 18	3.43 $\pm$ 0.34	6.42 $^{+0.01}_{-0.02}$	78 $\pm$ 18	3.44 $\pm$ 0.34
Fe K $\beta$	7.07 $^{+0.08}_{-7.10}$	=Fe K $\alpha$	0.61 $\pm$ 0.26	7.06 $^{+0.07}_{-7.10}$	=Fe K $\alpha$	0.81 $\pm$ 0.26	7.08 $^{+0.09}_{-7.10}$	=Fe K $\alpha$	0.49 $\pm$ 0.25	7.08 $^{+0.08}_{-7.10}$	=Fe K $\alpha$	0.50 $\pm$ 0.25
Ni K $\alpha$	7.80 $\pm$ 0.31	=Fe K $\alpha$	0.37 $\pm$ 0.35	7.80 $\pm$ 0.05	=Fe K $\alpha$	4.59 $\pm$ 0.44	7.80 $\pm$ 0.48	=Fe K $\alpha$	0.26 $\pm$ 0.50	7.80 $\pm$ 0.062	=Fe K $\alpha$	1.95 $\pm$ 0.37
Flux $^{\S}$	1.3864			1.3792			1.3877			1.3813		
$\chi^2_{\nu}$ (d.o.f)	1.82 (325)			3.72 (325)			1.81 (323)			1.70 (323)		

$\diamond$  : The uncertainties are in the 90% confidence range.

\* : In unit of  $10^{21} \text{ cm}^{-2}$ .

$\dagger$  : In units of  $10^{-3} \text{ cm}^{-2} \text{ s}^{-1}$ .

$\ddagger$  : In units of  $10^{-6} \text{ cm}^{-2} \text{ s}^{-1}$ .

$\S$  : In units of  $10^{-12} \text{ erg cm}^{-2} \text{ s}^{-1}$  between 1.7–9.0 keV.

Flux of He $\gamma$  fixed to  $0.3 \times \text{He}\beta$ .

Flux of Ly $\beta$  fixed to  $\text{He}\beta/\text{He}\alpha \times \text{Ly}\alpha$ .



# REFERENCES

- Anders, E., & Grevesse, N. 1989, *Geochim. Cosmochim. Acta*, 53, 197
- Arnaud, K. A. 1996, in *Astronomical Society of the Pacific Conference Series*, Vol. 101, *Astronomical Data Analysis Software and Systems V*
- Badenes, C., Hughes, J. P., Bravo, E., & Langer, N. 2007, *ApJ*, 662, 472
- Badenes, C., Maoz, D., & Draine, B. T. 2010, *MNRAS*, 407, 1301
- Bamba, A., Yamazaki, R., Ueno, M., & Koyama, K. 2003, *ApJ*, 589, 827
- Barret, D., den Herder, J.-W., & Piro, L. 2015, in *Exploring the Hot and Energetic Universe: The first scientific conference dedicated to the Athena X-ray observatory*, 4
- Black, J. K., Baker, R. G., Deines-Jones, P., Hill, J. E., & Jahoda, K. 2007, *Nuclear Instruments and Methods in Physics Research A*, 581, 755
- Borkowski, K. J., Hendrick, S. P., & Reynolds, S. P. 2006, *ApJ*, 652, 1259
- Borkowski, K. J., Hendrick, S. P., & Reynolds, S. P. 2007, *ApJ*, 671, L45
- Borkowski, K. J., Rho, J., Reynolds, S. P., & Dyer, K. K. 2001, *ApJ*, 550, 334
- Brickhouse, N. S., Dupree, A. K., Edgar, R. J., *et al.* 2000, *ApJ*, 530, 387
- Chevalier, R. A. 1974, *ApJ*, 188, 501
- Dickey, J. M., & Lockman, F. J. 1990, *ARA&A*, 28, 215
- Dwarkadas, V. V. 2005, *ApJ*, 630, 892
- Filipovic, M. D., Jones, P. A., White, G. L., & Haynes, R. F. 1998, *A&AS*, 130, 441
- French, M. J., Jones, L. L., Morrissey, Q., *et al.* 2001, *Nuclear Instruments and Methods in Physics Research A*, 466, 359

- Green, D. A. 2014, *Bulletin of the Astronomical Society of India*, 42, 47
- Haberl, F., & Pietsch, W. 1999, *A&AS*, 139, 277
- Harkness, R. P., & Wheeler, J. C. 1990, in *Supernovae*, 1–29
- Hendrick, S. P., Borkowski, K. J., & Reynolds, S. P. 2003, *ApJ*, 593, 370
- Hendrick, S. P., Reynolds, S. P., & Borkowski, K. J. 2005, *ApJL*, 622, L117
- Hess, V. F. 1912, *Physikalische Zeitschrift*, 13, 1084
- Hughes, J. P., Ghavamian, P., Rakowski, C. E., & Slane, P. O. 2003, *ApJL*, 582, L95
- Hughes, J. P., Hayashi, I., & Koyama, K. 1998, *ApJ*, 505, 732
- Hughes, J. P., Hayashi, I., Helfand, D., *et al.* 1995, *ApJL*, 444, L81
- Ishisaki, Y., Maeda, Y., Fujimoto, R., *et al.* 2007, *PASJ*, 59, 113
- Iwamoto, K., Brachwitz, F., Nomoto, K., *et al.* 1999, *ApJS*, 125, 439
- Jahoda, K. M., Black, J. K., Hill, J. E., *et al.* 2014, in *Society of Photo-Optical Instrumentation Engineers (SPIE) Conference Series*, Vol. 9144
- Jennings, Z. G., Williams, B. F., Murphy, J. W., *et al.* 2012, *ApJ*, 761, 26
- Jennings, Z. G., Williams, B. F., Murphy, J. W. *et al.* 2014, *ApJ*, 795, 170
- Kelley, R. L., Mitsuda, K., Allen, C. A., *et al.* 2007, *PASJ*, 59, 77
- Klinger, R. J., Dickel, J. R., Fields, B. D., & Milne, D. K. 2002, *AJ*, 124, 2135
- Kobayashi, C., Umeda, H., Nomoto, K., Tominaga, N., & Ohkubo, T. 2006, *ApJ*, 653, 1145
- Kosenko, D., Helder, E. A., & Vink, J. 2010, *A&A*, 519, A11
- Koyama, K., Petre, R., Gotthelf, E. V., *et al.* 1995, *Nature*, 378, 255
- Koyama, K., Tsunemi, H., Dotani, T., *et al.* 2007, *PASJ*, 59, 23
- Lee, J.-J., Park, S., Hughes, J. P., Slane, P. O., & Burrows, D. N. 2011, *ApJL*, 731, L8
- Lewis, K. T., Burrows, D. N., Hughes, J. P., *et al.* 2003, *ApJ*, 582, 770

- Lopez, L. A., Castro, D., Slane, P. O., *et al.* 2014, ApJ, 788, 5
- Lopez, L. A., Ramirez-Ruiz, E., Badenes, C., *et al.* 2009, ApJL, 706, L106
- Lopez, L. A., Ramirez-Ruiz, E., Huppenkothen, D., *et al.* 2011, ApJ, 732, 114
- Maggi, P., Haberl, F., Sturm, R., & Dewey, D. 2012, A&A, 548, L3
- Masai, K. 1984, Ap&SS, 98, 367
- Masai, K. 1994, ApJ, 437, 770
- McKee, C. F. 1974, ApJ, 188, 335
- Mitsuda, K., Bautz, M., Inoue, H., *et al.* 2007, PASJ, 59, 1
- Nomoto, K., Thielemann, F.-K., & Yokoi, K. 1984, ApJ, 286, 644
- Novick, R., Weisskopf, M. C., Berthelsdorf, R., Linke, R., & Wolff, R. S. 1972, ApJL, 174, L1
- Ohnishi, T., Koyama, K., Tsuru, T. G., *et al.* 2010, American Institute of Physics Conference Series, Vol. 1269, 463–465
- Ozawa, M. 2010, Ph.D. Thesis
- Ozawa, M., Koyama, K., Yamaguchi, H., Masai, K., & Tamagawa, T. 2009, ApJL, 706, L71
- Park, S., Hughes, J. P., Burrows, D. N., *et al.* 2003a, ApJL, 598, L95
- Park, S., Hughes, J. P., Slane, P. O., *et al.* 2003b, ApJL, 592, L41
- Park, S., Hughes, J. P., Slane, P. O., *et al.* 2012, ApJ, 748, 117
- Pols, O. 1997, in Astronomical Society of the Pacific Conference Series, Vol. 130, The Third Pacific Rim Conference on Recent Development on Binary Star Research, 153
- Rest, A., Suntzeff, N. B., Olsen, K., *et al.* 2005, Nature, 438, 1132
- Russell, S. C., & Dopita, M. A. 1992, ApJ, 384, 508
- Sato, T., Koyama, K., Takahashi, T., Odaka, H., & Nakashima, S. 2014, PASJ, 66, 124
- Sawada, M., & Koyama, K. 2012, PASJ, 64, arXiv:1202.3125

- Schenck, A., Park, S., Burrows, D. N., *et al.* 2014, *ApJ*, 791, 50
- Sedov, L. I. 1959, *Similarity and Dimensional Methods in Mechanics*
- Serlemitsos, P. J., Soong, Y., Chan, K.-W., *et al.* 2007, *PASJ*, 59, 9
- Slane, P., Gaensler, B. M., Dame, T. M., *et al.* 1999, *ApJ*, 525, 357
- Slane, P., Hughes, J. P., Edgar, R. J., *et al.* 2001, *ApJ*, 548, 814
- Smith, R. C., Kirshner, R. P., Blair, W. P., & Winkler, P. F. 1991, *ApJ*, 375, 652
- Smith, R. C., Raymond, J. C., & Laming, J. M. 1994, *ApJ*, 420, 286
- Takahashi, T., Abe, K., Endo, M., *et al.* 2007, *PASJ*, 59, 35
- Takahashi, T., Mitsuda, K., Kelley, R., *et al.* 2014, *Society of Photo-Optical Instrumentation Engineers (SPIE) Conference Series*, Vol. 9144, 25
- Takeuchi, Y., Tamagawa, T., Asami, F., *et al.* 2012, *Journal of Instrumentation*, 7, C3042
- Takeuchi, Y., Kitaguchi, T., Hayato, A., *et al.* 2014a, *Society of Photo-Optical Instrumentation Engineers (SPIE) Conference Series*, Vol. 9144, 4
- Takeuchi, Y., Tamagawa, T., Kitaguchi, T., *et al.* 2014b, *Journal of Instrumentation*, 9, C01002
- Takeuchi, Y., Yamaguchi, H., & Tamagawa, T. 2016, *PASJpublish*, arXiv:1511.08992
- Tamagawa, T., Tsunoda, N., Hayato, A., *et al.* 2006, *Nuclear Instruments and Methods in Physics Research A*, 560, 418
- Tamagawa, T., Hayato, A., Asami, F., *et al.* 2009, *Nuclear Instruments and Methods in Physics Research A*, 608, 390
- Tanaka, Y., Inoue, H., & Holt, S. S. 1994, *PASJ*, 46, L37
- Thielemann, F.-K., Nomoto, K., & Hashimoto, M.-A. 1996, *ApJ*, 460, 408
- Trudolyubov, S., & Priedhorsky, W. 2005, in *X-Ray and Radio Connections*, 4
- Tucker, W. H., & Gould, R. J. 1966, *ApJ*, 144, 244
- Uchida, H., Koyama, K., & Yamaguchi, H. 2015, *ApJ*, 808, 77

Uchida, H., Koyama, K., Yamaguchi, H., *et al.* 2012, PASJ, 64, arXiv:1208.0113

Uchiyama, Y., Aharonian, F. A., Tanaka, T., *et al.* 2007, Nature, 449, 576

van der Heyden, K. J., Bleeker, J. A. M., & Kaastra, J. S. 2004, A&A, 421, 1031

Vink, J. 2012, A&A Rev., 20, 49

Warren, J. S., & Hughes, J. P. 2004, ApJ, 608, 261

Warren, J. S., Hughes, J. P., & Slane, P. O. 2003, ApJ, 583, 260

Weisskopf, M. C., Cohen, G. G., Kestenbaum, H. L., *et al.* 1976, ApJL, 208, L125

Weisskopf, M. C., Silver, E. H., Kestenbaum, H. L., *et al.* 1978, ApJL, 220, L117

Westerlund, B. E. 1990, A&A Rev., 2, 29

Williams, R. M., Chu, Y.-H., Dickel, J. R., *et al.* 2005, ApJ, 628, 704

Woosley, S. E., & Eastman, R. G. 1997, NATO Advanced Science Institutes (ASI) Series C, Vol. 486, 821

Yamaguchi, H., Ozawa, M., Koyama, K., *et al.* 2009, ApJL, 705, L6

Yamaguchi, H., Koyama, K., & Uchida, H. 2011, PASJ, 63, 837

Yamaguchi, H., Badenes, C., Petre, R., *et al.* 2014a, ApJL, 785, L27

Yamaguchi, H., Eriksen, K. A., Badenes, C., *et al.* 2014b, ApJ, 780, 136

Yamauchi, S., Nobukawa, M., Koyama, K., & Yonemori, M. 2013, PASJ, 65

Yokogawa, J., Imanishi, K., Koyama, K., Nishiuchi, M., & Mizuno, N. 2002, PASJ, 54, 53



# Acknowledgements

The present thesis was written as part of the doctor's course of the Department of Physics, Graduate School of Science, Tokyo University of Science. I could not have completed this thesis without the support from my collaborators.

Firstly, I would like to thank Prof. Toru Tamagawa, my supervisor. I am very grateful for his careful guidance, advice, and motivation and his continuous support since I was a fourth year undergraduate student. I have learned many things from him while I was a student.

I am especially grateful to Dr. Hiroya Yamaguchi of NASA/GSFC for giving me the chance to carry out this study and for his considerable assistance, despite his heavy workload. I have learned a lot from him about the science of supernovae, and it was a pleasure to study with him. I cannot thank him enough for his help.

I would like to thank all the members of Tamagawa High Energy Astrophysics Laboratory at RIKEN for their valuable advice from differing viewpoints and their extensive support.

I also express my thanks to Dr. Hideaki Otsu, Dr. Ken'ichiro Yoneda, and Dr. Yasuo Wakabayashi at RIKEN for always caring for me and their support.

This work was financially supported by the Japan Society for the Promotion of Science through a Research Fellowship for Young Scientists.

Finally, I would like to thank my family and friends, who have encouraged me when I was feeling down or feeling like giving up. I will never forget their kindness.